Plasmon Induced Carrier Polarization in Semiconductor Nanocrystals

by

Penghui Yin

A thesis
presented to the University of Waterloo
in fulfillment of the
thesis requirement for the degree of
Doctor of Philosophy
in
Chemistry (Nanotechnology)

Waterloo, Ontario, Canada, 2020

Examining Committee Membership

The following served on the Examining Committee for this thesis. The decision of the Examining Committee is by majority vote.

External Examiner	NAME: Kevin Kittilstved
	Title: Associate Professor
Supervisor(s)	NAME: Pavle V. Radovanovic
	Title: Professor
Internal Member	NAME: Germán Sciaini
	Title: Associate Professor
Internal Member	NAME: Eric Prouzet
	Title: Associate Professor
Internal-external Member	NAME: Zoran Miskovic
	Title: Professor
Other Member(s)	NAME: Daniel Thomas
	Title: Associate Professor

AUTHOR'S DECLARATION

I hereby declare that I am the sole author of this thesis. This is a true copy of the thesis, including any required final revisions, as accepted by my examiners.

I understand that my thesis may be made electronically available to the public.

Abstract

Currently used technologies are reaching the natural performance limit, invigorating the development of different quantum technologies. Spintronics and valleytronics are emerging quantum electronic technologies that rely on using electron spin and multiple extrema of the band structure (valleys), respectively, as additional degrees of freedom. There are also collective properties of electrons in semiconductor nanostructures that potentially could be exploited in multifunctional quantum devices. Specifically, plasmonic semiconductor nanocrystals (NCs) offer an opportunity for interface-free coupling between a plasmon and an exciton. However, plasmon–exciton coupling in single-phase semiconductor NCs remains challenging because confined plasmon oscillations are generally not resonant with excitonic transitions. In this thesis, using magnetic circular dichroism (MCD) spectroscopy, I examined the electron polarization in plasmonic semiconductor NCs, and the effect of electron localization, plasmon oscillator strength and damping, as well as NC morphology on carrier polarization. The results effectively open up the field of *plasmontronics*, which involves the phenomena that arise from intrinsic plasmon–exciton and plasmon–spin interactions. Furthermore, the dynamic control of carrier polarization allows us to harness the magnetoplasmonic mode as a new degree of freedom in practical photonic, optoelectronic and quantum-information processing devices.

First, we demonstrated the control of excitonic splitting in In_2O_3 NCs upon excitation with circularly polarized light in an external magnetic field by simultaneous control of the electronic structure of donor defects and the nanocrystal host lattice. Using variable-temperature− variable-field MCD spectroscopy, we show that the NC band splitting has two distinct contributions in plasmonic In_2O_3 NCs. Temperature-independent splitting arises from the cyclotron magnetoplasmonic modes, which impart angular momentum to the conduction band excited states near the Fermi level, and increases with the intensity of the corresponding plasmon resonance. Temperature-dependent splitting is associated with the localized electron spins trapped in defect states. The ratio of the two components can be controlled by the formation of oxygen vacancies or introduction of aliovalent dopants. Using these experimental results in conjunction with the density functional theory modeling, relative contribution of the two mechanisms is discussed in the context of the perturbation theory taking into account energy separation between the NC excited states and the localized defect states.

To implement such opportunities it is essential to develop robust understanding of the parameters that influence magnetoplasmon-induced carrier polarization. I investigated comparatively the plasmonic properties of Mo-doped In_2O_3 (IMO) and W-doped In_2O_3 (IWO) NCs, with a particular

emphasis on the role of plasmonic properties on excitonic splitting. In contrast to tungsten dopants, which are predominantly in 6+ oxidation state, molybdenum coexists as Mo^{5+} and Mo^{6+}, resulting in a lower dopant activation in IMO compared to IWO NCs. By manipulating the plasmonic properties of these two NC systems, such as localized surface plasmon resonance energy, intensity, and damping, we identified two opposing influences determining the excitonic Zeeman splitting induced by magnetoplasmonic modes. Localized surface plasmon resonance oscillator strength, commensurate with free carrier density, increases while electron damping, caused by ionized impurity scattering, decreases the transfer of the angular momentum from the magnetoplasmonic modes to the conduction band electronic states. The results contribute to fundamental understanding of the mechanism of non-resonant plasmon-exciton coupling and magnetoplasmon-induced Zeeman splitting in degenerate semiconductor NCs, allowing for the rational design of multifunctional materials with correlated plasmon and charge degrees of freedom.

The magnetoplasmon-induced carrier polarization was further attested in oxygen-deficient TiO_2 NCs of which the excitonic MCD band has an opposite sign compared to that observed for plasmonic In_2O_3 NCs indicating the plasmon-induced carrier polarization can be controlled by the electronic properties of NC host lattice. In addition, further manipulation of excitonic splitting in colloidal TiO_2 NCs was demonstrated by simple control of their faceting. By changing NC morphology via reaction conditions, I controlled the concentration and location of oxygen vacancies, which can generate localized surface plasmon resonance and foster the reduction of lattice cations leading to the emergence of individual or exchange-coupled Ti(III) centers with high net-spin states. These species can all couple with the nanocrystal lattice under different conditions resulting in distinctly patterned excitonic Zeeman splitting and selective control of conduction band states in an external magnetic field. These results demonstrate that the combination of redox-active vacancy sites and nanocrystal morphology can be used to control quantum states in individual NCs using both localized and collective electronic properties, representing a new approach to complex multifunctionality in reduced dimensions.

The results of this work demonstrate the ability to control carrier polarization in nonmagnetic metal oxide NCs using both individual and collective electronic properties, and allow for their application as an emerging class of multifunctional materials with strongly interacting degrees of freedom.

Acknowledgements

First, I would like to express my sincere gratitude to my supervisor Dr. Pavle V. Radovanovic for his invaluable support throughout the project. His guidance and enthusiasm towards science encouraged me to face many difficulties I encountered and become a better researcher.

I would like to thank my committee members, Dr. Germán Sciaini, Dr. Daniel Thomas and Dr. Eric Prouzet, for their time, insightful advices, and valuable comments on my research during past few years. I would also like to thank external examiner Dr. Kevin Kittilstved and internal external examiner Dr. Zoran Miskovic for reading my thesis and attending the thesis defense.

I would like to acknowledge Dr. Carmen Andrei at the Canadian Center for Electron Microscopy for her assistance in TEM image collection. I thank Dr. Jian Wang for his support at the 10ID beamline at Canadian Light Source and Dr. Zou Finfrock , Dr. Debora Motta Meira at the 20-BM beamline and Dr. Richard Rosenberg at the 4-ID beamline at Advanced Photon Source for their assistance. I acknowledge Waterloo Institute for Nanotechnology for Graduate Research Fellowships and Canadian Light Source for Graduate Student Travel Awards (CLS@APS).

I would also like to thank my previous and present fellow group members for their assistance and encouragement. I had the pleasure of working with previous group members Vahid, Hanbing, Yi, Yunyan, Natalie and Manu and current group members Paul, Wenhuan, Chenwei, Shuoyuan, Nathaniel, I-hsuan, and Archisman. In particular, I would like to thank Manu for helping me with the density functional theory calculations for several projects. I also acknowledge Natalie for spending time on magnetic circular dichroism measurements with me and helping me analyze the X-ray absorption data. I would like to thank Yi and Hanbing for helping me with sample synthesis.

I thank my friend Dapeng and Yang from Dr. Xiaosong Wang's group for their help on the dynamic light scattering and the low-magnification TEM measurements. Yixuan and Parisa from Dr. Holger Kleinke's lab helped me with the XRD measurements. I also thank Paola and Sahar from Giga to Nanoelectronics Center for helping me with the Raman measurements.

Last but not least, I am grateful to my parents and my fiancée for their understanding and support. Their love gives me the energy to reach my goals.

Dedication

I would like to dedicate this thesis to my parents Changlin Yin and Dongqin Wang, and my fiancée Xin Zheng for their tremendous love and support.

Table of Contents

List of Figures

List of Tables

List of Abbreviations

APS	Advanced photon source
bcc	Body-center cubic
DFT	Density functional theory
DMS	Diluted magnetic semiconductor
DMSOs	Diluted magnetic semiconductor oxides
DLS	Dynamic light scattering
EDX	Energy dispersive X-ray spectroscopy
EPR	Electron paramagnetic resonance
FTIR	Fourier-transform infrared spectroscopy
GGA	Generalized gradient approximation
GMR	Giant magnetoresistance
IMO	Molybdenum-doped In_2O_3
ITO	Tin-doped In_2O_3
IWO	Tungsten-doped In_2O_3
LCP	Left circularly polarized
LO	Longitudinal Optical
LSPR	Localized surface plasmon resonance
MCD	Magnetic circular dichroism
MIR	Mid infrared
MP	Monkhorst-Pack
NCs	Nanocrystals
NIR	Near infrared
NPs	Nanoparticles
PBE	Perdew-Burke-Ernzerhof
PPMS	Physical property measurement system

QDs	Quantum dots
RCP	Right circularly polarized
TEM	Transmission electron microscopy
THz	Tetrahertz
TO	Transverse optical
UV-Vis-NIR	Ultraviolet-visible-near infrared
XAS	X-ray absorption spectroscopy
XANES	X-ray absorption near edge structure
XPS	X-ray photoemission spectroscopy

Chapter 1
Introduction

1.1 Localized Surface Plasmon Resonance in Semiconductor Nanocrystals

A thousand years ago, colloidal gold nanoparticles (NPs) have been used to make colorful glasses, which is one of the first exploitations of nanomaterials in history, although, at the time, people did not have a clear understanding about the mechanism of this phenomenon. With the recent development in nanoscience and nanotechnologies, the origin of this coloration has been unveiled, catalyzing the development of the new research field of plasmonics. At the heart of plasmonics is localized surface plasmon resonance (LSPR) which is defined as a collective oscillation of conduction electrons at the surface of NPs when stimulated with incident light with resonant photon frequency.[1] Two striking properties of LSPR are the large absorbance at the resonant plasmon frequency and the significant enhancement of electric field near the particle surface.[2] These unique features render plasmonic metal NPs particularly interesting for different technologies, which include photovoltaics,[3] chemical and biomolecular sensors,[4] and photothermal cancer therapy.[5]

The LSPR is not exclusively limited in metal NPs, it could also be exhibited in conducting metal oxide nanocrystals (NCs) and semiconductor NCs with a large free carrier concentration.[6] Recent years have seen a surge of the interest in plasmonic semiconductor nanostructures, as an alternative to their noble metal counterparts.[7] Generally, LSPR of semiconductor NCs is expected to have similar size and shape tunability as metal nanostructures.[8] In addition, semiconductor and metal oxide NCs offer an opportunity to adjust the type and concentration of charge carriers by aliovalent doping (substitutional or interstitial),[9-10] or controlling the stoichiometry (cation or anion deficiency),[8,11] as shown in Figure 1.1. As a result, degenerately doped semiconductor and metal oxide NCs exhibit resonant plasmon oscillations in the near-to-mid-infrared spectral range (Figure 1.2). Furthermore, the ability to control carrier activation, trapping, and scattering *via* NC composition and/or surface chemistry allows for fine tuning of the energy, band width, and quality factor of the LSPR.[12-15]

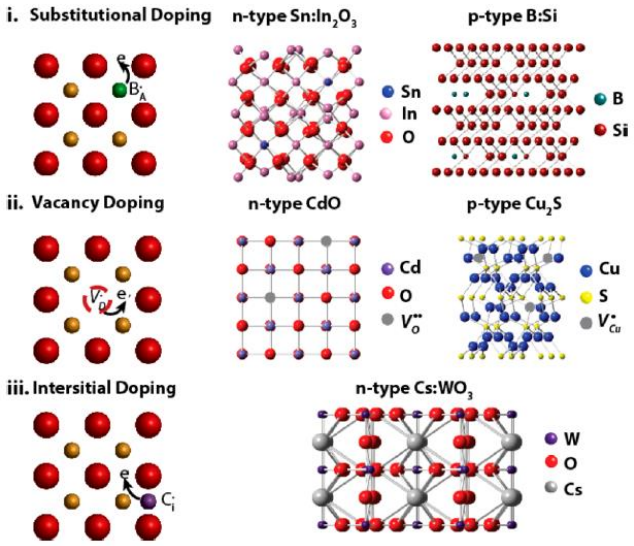

Figure 1.1 Schemes of common doping mechanisms including (i) aliovalent substitutional impurities, (ii) vacancies, and (iii) interstitial impurities (left), and corresponding examples of n- and p-type-doped semiconductor systems (right). Orange and red spheres in the schemes on the left represent host lattice cations and anions, respectively.[7*]

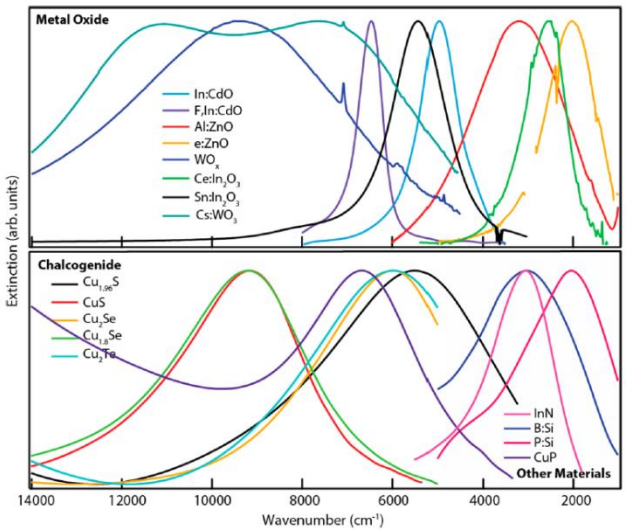

Figure 1.2 LSPR extinction spectra of representative n-type metal oxide NCs (top panel) and p-type copper chalcogenides NCs (bottom panel). The extinction spectra of representative plasmonic metal nitride, metal phosphide, as well as aliovalent doped Si NCs are also included in the bottom panel.[7*]

---

[*]Reprinted with permission from (Agrawal, A.; Cho, S. H.; Zandi, O.; Ghosh, S.; Johns, R. W.; Milliron, D. J., Chem. Rev. **2018**, *118*, 3121-3207). Copyright (2018) American Chemical Society.

1.1.1 n-Type Plasmonic Semiconductor NCs

Plasmonic metal oxides[9,11,16-20] (In_2O_3, ZnO, CdO, SnO_2, TiO_2, MoO_3 and WO_3) are generally intrinsic n-type semiconductors with the free electrons generated by oxygen vacancies and interstitial cations.[21-23] These metal oxides, as bulk materials, normally possess a small amount of free electrons which is not capable of forming the LSPR in near infrared (NIR) to mid infrared (MIR) region. For many metal oxides, the concentration of the oxygen vacancies can be adjusted through the oxygen partial pressure (synthetic atmosphere) or exposure of the high-energy facets of NCs.[24-25] It has been demonstrated that when a larger concentration of oxygen vacancies is favored by the reaction equilibrium, In_2O_3, TiO_2, MoO_3 and WO_3 NCs could have sufficient free electrons to generate LSPR.[11,20,26-27] It is worth mentioning that, some metal oxides, such as VO_2 and ReO_3, are intrinsically metallic and could possess the LSPR in the NIR and even visible light region.[28-29]

Aliovalent doping is a commonly used protocol to tune the electric properties of a semiconductor material in industry. With Sn-doped In_2O_3 (ITO) being one of the most widely used transparent conducting oxides (TCOs), the optical study of its nanocrystalline form opens the doors for investigation of prototype plasmonic semiconductors NCs.[9] Subsequently, different dopants were introduced into In_2O_3, including, Ti, Sb, Ce and Mo, to tune to plasmon frequency from NIR to MIR.[12,30-31] Many other types of metal oxides substitutionally doped with high-valence-cations have been extensively studied in the search of plasmonic semiconductor nanomaterials, including ZnO doped with Al, Ga, and In;[16] CdO doped with Dy, In, and Sn;[17,32-33] TiO_2 doped with Nb;[19] SnO_2 doped with Sb,[18] etc. In these degenerately doped semiconductor NCs, the dopants substitute the lattice cations and cause the shift of the Fermi level depending on the energetic alignment of the dopant orbitals with the conduction band of metal oxides. It is generally observed that, starting from pure metal oxide NCs, with increased dopant concentration, the free electron concentration increases and results in the blue shift of LSPR energy accompanied by increased absorption intensity (see section 1.2.2). However, eventually, adding more dopants stops blue-shift of the LSPR frequency and even leads to the red-shift of the LSPR. In the case of ITO, with high Sn dopant concentration, a portion of Sn^{4+} ions will be compensated by interstitial oxygen atoms and form ($2Sn_{In}\cdot - O_i''$) defect complexes resulting in the saturation effect in which additional Sn dopants no longer increases free electron concentrations.[34] In other cases, such as Sb-doped In_2O_3 and Dy-doped CdO, the red shift of the plasmon frequency has been attributed to the electrons scattering effect by lattice defects associated with a large concentration of dopants.[12,32] The free electrons in metal oxides can also be introduced by interstitial doping. For

example, WO_3, with a relatively open crystal lattice, allows for interstitial doping of ions (Cs, K, Li, Rb, etc.), resulting in accumulation of delocalized free electrons in the conduction band.[10,35]

In addition to metal oxides, several metal nitrides with high free electron concentration were also demonstrated to possess LSPR properties. TiN exhibits metallic properties with exceptionally high carrier concentration. Recently, TiN NCs have been synthesized using a non-thermal plasma route, and its LSPR band maxima tuned from 800 to 1000 nm.[36] InN NCs with a small band gap exhibits LSPR in MIR range.[37] One of the interesting phenomena in colloidal InN NCs is that its LSPR frequency remains nearly unchanged while the LSPR intensity is reduced by the oxidative titration.[38] This is in contrast with the behavior of LSPR in many metal oxides in which the plasmon intensity and energy changes in synchrony with each other. The invariance of LSPR energy is attributed to the strong conduction-band non-parabolicity at small wavevectors which leads to the strong dependence of the effective mass on carrier wavevectors (see section 1.2.3). Mercury chalcogenides (HgX: HgS, HgSe, and HgTe) have also drawn broad attention as they offers a large optical tunability from NIR to tetrahertz (THz) range. Shen *et al.* observed broad LSPR absorption centered around 1000 cm^{-1} for HgS quantum dots (QDs) with large sizes (ca. 15 nm).[39] Goubet *et al.* developed the method to synthesize colloidal HgTe NCs with size range from 5 nm to 200 nm.[40] For the large HgTe NCs which is well beyond the quantum confinement regime, the absorption feature in the THz range was assigned, at least partly, to the LSPR. The exciton Bohr radius for mercury chalcogenides is much larger than that of the metal oxides, which raises the possibility of the contribution from the intraband transition due to quantum confinement when discussing the absorption features in the IR range (see section 1.2.3). Phosphorus (P) doped Si NCs was synthesized by Rowe *et al.* using a non-thermal plasma method.[41] P-doped Si NCs with doping concentration ranging from 0 to 4% exhibits the LSPR peak tunability from 600 cm^{-1} to 2000 cm^{-1}. However, the propensity of forming the oxide layer at the surface of Si NCs leads to the degradation of LSPR intensity as appreciable amount of free electrons were trapped at defect states near Si/SiO_2 interface.

1.1.2 p-Type Plasmonic Semiconductor NCs

Contrary to metal oxides which have the propensity of forming anion vacancies, copper chalcogenides (Cu_2X: Cu_2S, Cu_2Se, Cu_2Te) tend to have copper vacancies which is thermodynamically more favorable compared with its stoichiometric form under ambient environment owing to the low chemical potential of Cu^0.[42-43] The formation of cation vacancies leads to the p-type conductivity in copper chalcogenides with hole concentration depending on the copper deficiency.[44] Substoichiometric $Cu_{2-x}X$ NCs exhibit

diverse crystal structures with different extent of copper deficiency.[43,45-46] It has been demonstrated that $Cu_{2-x}S$ NCs could exist in eight different phases with different concentration of copper vacancies.[46] Stoichiometric Cu_2S possesses a chalcocite phase with Cu atoms occupies the interstitial sites of an asymmetrically hexagonal closed packed S sublattice, which eventually evolved into cubic closed pack sublattice with increased Cu vacancies.

LSPR in $Cu_{2-x}X$ NCs is originated from the collective oscillation of free holes in the valence band in contrast to the oscillation of free electrons in n-type semiconductor NCs. As synthesized $Cu_{2-x}X$ NCs have the free hole concentration on the order of 10^{21} cm^{-3} which leads to the LSPR in the NIR region.[43] Luther *et al.* synthesized pseudospherical $Cu_{2-x}S$ QDs with various sizes ranging from 2.4 nm to 5.9 nm and observed the quantum confinement of the band gap absorption together with size-dependent LSPR absorption in the NIR region.[8] The diminished LSPR intensity in small $Cu_{2-x}S$ QDs has been attributed to the surface scattering of the free carriers. Kriegel *et al.* observed the NIR LSPR absorption for the whole class of $Cu_{2-x}X$ (X=S, Se, Te) NCs.[47] They also demonstrated that the $Cu_{1.97}S$ and $Cu_{1.8}Se$ are the thermodynamically stable forms over their stoichiometric counterparts. In addition, the stoichiometry of $Cu_{2-x}X$ NCs can be readily tuned by oxidative or reductive post-synthesis treatment which leads to the change of free hole concentration and thus its LSPR properties. Luther *et al.* demonstrated, upon exposing to air (oxygen), non-plasmonic stoichiometric Cu_2S nanorod will lose Cu atoms and generate LSPR with its energy and intensity controlled by time of oxygen exposure.[8] Inversely, using Cu(I) complex, Xie *et al.* converted strongly plasmonic $Cu_{1.1}S$ NCs to Cu_2S NCs in which LSPR is significantly diminished.[48] Dorfs *et al.* performed similar studies on $Cu_{2-x}Se$ NCs in which LSPR can be tuned reversibly by adding Ce(IV) complex (oxidation) or Cu(I) complex (reduction).[49]

In analogy to aliovalent doping in metal oxides, alloying with different cations and/or anions have been attempted to further tune the LSPR properties of $Cu_{2-x}X$ NCs. Several groups have explored the synthesis of $Cu_{2-x}S_ySe_{1-y}$ NCs and observed the blue shift of LSPR peak with increasing Se content.[50-52] Dilena *et al.* proposed that the effect is caused by the increase of Cu vacancies accompanied by the increased Se content.[51] Wang *et al.* attributed the effect to the decreased effective mass of the free holes when incorporating more Se into NCs given that the effective mass of holes in $Cu_{2-x}Se$ is 0.2−0.25 compared with 0.8 for $Cu_{2-x}S$.[52] Guo *et al.* synthesized $Cu_{2-x}S_yTe_{1-y}$ NCs and demonstrated the LSPR peak can be shifted to a higher energy by incorporating Te.[53] Niezgoda *et al.* reported the synthesis of $Cu_xIn_yS_2$ QDs ($0.88 \leq x \leq 1.01$, $0.95 \leq y \leq 0.91$) which exhibit the size-dependent LSPR properties.[54]

Wang *et al.* systematically studied the effects of In incorporation on size, morphology, crystal structure, and optical properties of Cu_xIn_yS NCs.[55] With increasing In content, LSPR peak of Cu_xIn_yS NCs shifts to lower energies with significant broadening, and is almost completely quenched when In content in NCs reaches 0.6 (y=0.6). They attributed the tuning of LSPR to the change of Cu deficiencies induced by In incorporation.

1.1.3 Contributing factors of LSPR in Semiconductor NCs

In_2O_3 NCs have been used as model system to study the contributing factor of LSPR in semiconductor NCs such as crystal structure,[15] NC size,[56] dopant distribution,[57] surface depletion,[58] strain effect,[30] and ensemble broadening[59] (Figure 1.3). Wang *et al.* synthesized and isolated the ITO NCs in body-center cubic (*bcc*) structure (around 10 nm) and metastable corundum phase (less than 5 nm) by size-selective precipitation.[15] The strong LSPR absorption in the NIR region was only observed for the ITO NCs with cubic crystal structure. The lack of LSPR in small NCs with corundum phase was attributed to the large band gap energy and the large separation between the Sn^{4+} donor state and the conduction band bottom which leads to significantly higher dopant activation energy, and thus no appreciable free electrons in the corundum phase ITO NCs. Crockett *et al.* synthesized the ITO NCs with almost identical dopant concentration and distribution but various sizes ranging from 5 nm to 21 nm.[56] The LSPR peaks of ITO NC samples exhibit a blue shift and decrease in linewidth as the NC size increases, indicating a large carrier concentration and less LSPR damping for large ITO NCs. The observed trend was attributed to the decreased surface area-to-volume ratio of larger NCs, which results in the reduced Sn dopant ions that are in inactive trap states at the surface, and less scattering of electrons by Sn dopant atoms near the surface. Using different precursors and ligands, two series of ITO NCs with different Sn dopant distributions (surface segregated *vs* uniformly distributed) were achieved by Lounis *et al.*[57] They observed different dopant activation energy and LSPR line shape for the two series of samples, which were attributed to the interstitial oxygen atoms and the Sn orbital hybridization near the surface vicinity. Zandi *et al.* observed the effect of depletion layer, caused by native surface defect, on the electrochemical modulation of LSPR and the near-field enhancement of ITO NCs.[58] The depletion layer, which is determined by NC sizes and Sn dopant concentration, reduces the near-field effect and the sensitivity of LSPR to surrounding environment. Runnerstrom *et al.* synthesized Ce-doped In_2O_3 NCs and observed significantly reduced LSPR band width in comparison to that of ITO NCs exhibiting similar LSPR energies.[30] It is proposed that the relatively similar sizes between Ce^{4+} and In^{3+} ions minimize the lattice strain and lead to high electron mobility and thus the narrow LSPR band width.

Using synchrotron infrared nanospectroscopy, Johns *et al.* investigated the LSPR band shape of individual ITO NC and observed significant particle-to-particle variability in LSPR energy as well as band width.[59] The ensemble measurement shows much broader LSPR band width which is associated with the size, shape, dopant (concentration and distribution) heterogeneity.

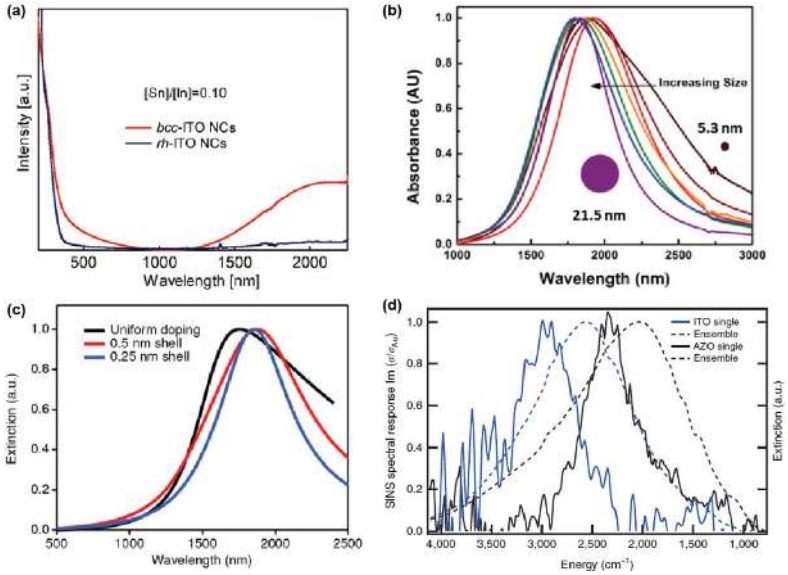

Figure 1.3 Absorption spectra of ITO NCs influenced by different parameters. (a) Absorption spectra of *bcc*-ITO (red line) and *rh*-ITO (blue line) NCs with the same doping concentrations.[15†] (b) absorption spectra of ITO NCs with identical doping concentrations and different sizes ranging from 5.3 to 21.5 nm, the black arrow indicates increasing NC sizes.[56‡] (c) absorption spectra of ITO NCs with uniformly distributed Sn dopants (black line) and surface segregated Sn dopants located in 0.25 nm shell (blue line) and 0.5 nm shell (red line).[57‡‡] (d) absorption spectra of single ITO (solid blue line) and AZO, solid black line) NC and their ensemble counterpart (dashed blue and black line for ITO and AZO, respectively).[59]

---

†Reprinted with permission from (Wang, T.; Radovanovic, P. V., J. Phys. Chem. C **2010,** *115*, 406-413). Copyright (2010) American Chemical Society.

‡Adapted with permission from (Crockett, B. M.; Jansons, A. W.; Koskela, K. M.; Sharps, M. C.; Johnson, D. W.; Hutchison, J. E., Chem. Mater. **2019**, *31*, 3370-3380). Copyright (2010) American Chemical Society.

‡‡Reprinted with permission from (Lounis, S. D.; Runnerstrom, E. L.; Bergerud, A.; Nordlund, D.; Milliron, D. J., J. Am. Chem. Soc. **2014**, *136*, 7110-7116). Copyright (2014) American Chemical Society.

1.1.4 Dynamic Modulation of LSPR in Semiconductor NCs

The aforementioned reversible tuning of LSPR in $Cu_{2-x}Se$ NCs by chemical redox reactions is one of the typical examples of dynamic modulation of LSPR in semiconductor NCs. Post-synthetic tuning of LSPR by oxidation/reduction were also attempted using plasmonic metal oxide NCs. Kim *et al.* synthesized hexagonal Cs-doped WO_3 nanoplatelets and observed the quenching and red shift of its LSPR upon air exposure due to the oxidation of NCs (Figure 1.4a).[60] The oxidized NCs could be reduced by the addition of hydrazine and the LSPR peak will restore the original peak position. The similar studies were conducted by Hu *et al.* in which they demonstrated, upon annealing in O_2 and N_2, LSPR of ITO NCs red-shifts upon oxidation in O_2 and blue-shifts to its original position upon reduction in N_2.[61] It is worth noting that the well-controlled reduction of LSPR by oxidants have been employed to quantitatively calculate the free carriers in plasmonic semiconductor NCs. There are two oxidants commonly used in the oxidative titration experiments. One is $[FeCp^*_2]^+$, which is effective for removing the photo-doped electrons on NCs.[62] However, it is relatively weak and has negligible effect on the electrons generated by aliovalent or vacancy doping. Stronger oxidants such as Ce^{4+}, $[NO]^+$, or $[N(C_6H_4Br\text{-}4)_3]^{\bullet+}$ can be used to remove more stable free electrons.[62] $NOBF_4$ was used to as oxidants to titrate the free electrons in InN NCs.[38]

Photochemical charging has also been employed to dynamically tune the LSPR of semiconductor NCs. The additional free electrons in NC conduction band are generated by illumination with UV light (above band gap energy) and stabilized in anaerobic conditions with the presence of a hole scavenger. Schimpf *et al.* systematically investigated the IR absorption spectra of photochemically charged ZnO NCs with different sizes varying from 1.5 nm to 6 nm.[63] They performed the magnetic circular dichroism (MCD) measurements on the IR feature of the small NCs and observed the similar behavior as reported for LSPR absorption of Au NPs. Thus the IR absorption was assigned to LSPR instead of the intra-conduction-band single-electron transitions which was originally interpreted for the photo-charged NCs.[64] By using different hole quenchers, they demonstrated that photochemically induced free electrons can be further increased.[65] Schimpf *et al.* manipulated the LSPR of colloidal In_2O_3 and ITO NCs by photochemical charging and demonstrated that the presence of Sn dopants has negligible effect on the photochemically added free electrons (Figure 1.4 b).[62] They proposed that the maximum photodoping level is mainly determined by the thermodynamic factors relating to the hole quencher and the chemical potential of photochemically generated carriers.

One of the common approaches to tune the carrier concentration and thus the optical properties of semiconductor NCs is through the electrochemical charging/discharging in the battery-type cell with electrolyte. The electrochemically injected electrons are stabilized by electrolyte cations via intercalation (Li^+ or H^+) or capacitive effect.[66-67] Electrochemical modulation of LSPR in TCO NCs have received broad attention in the development of electrochromic smart windows.[68-69] Garcia *et al.* demonstrated the dynamic and reversible tuning of the LSPR in ITO NCs thin film in which the free electron concentration can be changed by a factor of three.[70] In order to achieve efficient charging/discharging upon applied voltages, the surface ligand on the ITO NCs has to been removed to form a conducting network. The similar studies also were performed on p-type Cu_2Se NCs. Llorente *et al.* achieved reversible tuning of LSPR in $Cu_{2-x}Se$ NCs by capacitive charging/discharging, indicating the free hole concentration in the valence band can also be effectively tuned electrochemically.[71] In contrast, under the same experiment condition, LSPR of CuS NCs can merely be tuned to a small extent which was attributed to the metallic electronic structure of CuS. As mentioned above, Zandi *et al.* systematically investigated electrochemical modulation of the ITO NCs with different sizes and Sn doping concentrations.[58] They observed the significant shift of LSPR frequency for small ITO NCs with low doping concentrations during the electrochemical charging/discharging (Figure 1.4 c). In contrast, the LSPR frequency of large ITO NCs with high doping concentration exhibit much smaller shift. Using optical modelling, they correlated the experimental results to the different extent of surface depletion associated with different ITO NCs, which dictates the charge accumulation and distribution across the NCs and thus determine the LSPR properties of ITO NCs.

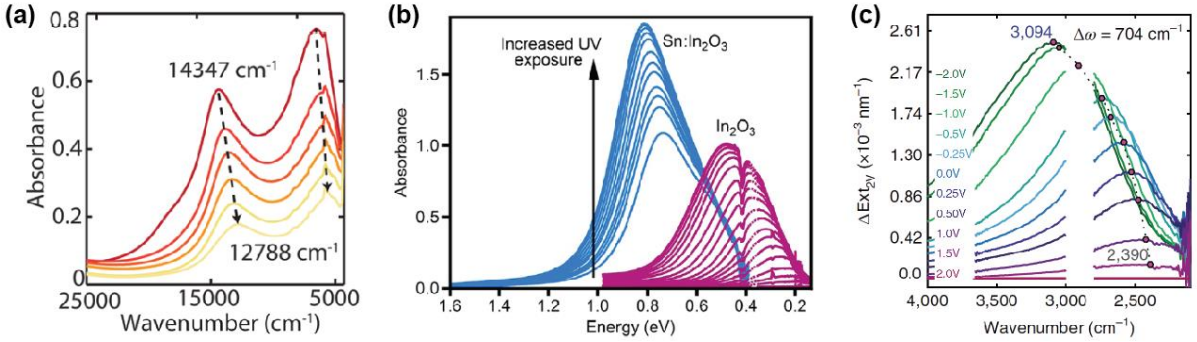

Figure 1.4 Examples of dynamic tuning of LSPR spectra using different methods. (a) Absorption of dynamic optical absorption spectra of h-Cs:WO_3 platelets undergoing oxidation by exposure to air for up to 24 h. The arrows indicate increasing time of exposure.[60§] (b) absorption spectra before and following various extents of photodoping of In_2O_3 (right, ~0.4 eV) and 9.0% Sn-doped In_2O_3 (left, ~0.8 eV) NCs. The arrows show the direction of increasing photodoping.[62§§] (c) *In-situ* FTIR spectroelectrochemistry spectra of 7.4 nm-1%ITO NC thin film collected at various applied potentials relative to that at 2V. The color code for different potentials are indicated on the left side of the panel. The blank region corresponds to the absorption saturation associated with the electrolyte.[58§§§]

1.2 Physical Model of LSPR in Semiconductor NCs

The theoretical framework of LSPR in semiconductor NCs is developed on the basis of light-matter interaction involving semiconductor NCs uniformly dispersed in a matrix with dielectric constant ε_m. Considering the light as a propagating transverse electromagnetic wave, the optical properties of non-magnetic NCs (absorption and scattering) are determined by electric field inside and outside the NCs which can be calculated through solving Maxwell's equations. For simplicity, we will focus on the case in which the semiconductor NCs have a spherical shape and isotropic dielectric constant ε_D, and thus the Mie theory can be applied to solve Maxwell's equations. For the NCs with other geometries, Maxwell's equations usually need to be solved numerically by computational methods.

1.2.1 Mie Theory

Mie theory was proposed by Gustav Mie at the beginning of 20th century in order to describe the interaction between an electromagnetic plane wave and a sphere characterized by its diameter and its complex refractive index.[72] It was first developed to study the scattering effect of spherical Au NPs,

and later extended to simulate the optical properties of semiconductor NCs. Using Mie theory, the absorption and scattering cross sections can be solved as equation (1.1) and (1.2).

$$C_{ext}(\omega) = 4\pi R^3 k\sqrt{\varepsilon_m}\,\mathrm{Im}\left\{\frac{\varepsilon_D(\omega)-\varepsilon_m}{\varepsilon_D(\omega)+2\varepsilon_m}\right\} \qquad \textbf{(Equation 1.1)}$$

$$C_{sca}(\omega) = 4\pi R^6 k\sqrt{\varepsilon_m}\,\mathrm{Im}\left|\frac{\varepsilon_D(\omega)-\varepsilon_m}{\varepsilon_D(\omega)+2\varepsilon_m}\right|^2 \qquad \textbf{(Equation 1.2)}$$

Here, $k = \omega / c$ is the wavevector of the light, R is the radius of NCs. Based on equation (1.1) and (1.2), the optical properties are dictated by the dielectric function of NCs. When the dielectric function is complex ($\varepsilon_D(\omega) = \varepsilon_1(\omega) + i\varepsilon_2(\omega)$) with a negative real part ($\varepsilon_1(\omega) < 0$), the maximum extinction is reached when $\varepsilon_1(\omega) = -2\varepsilon_m$ based on eq. (1). This condition indicates the absorption is maximized at a resonant incident light frequency which is the physical basis of LSPR. The dielectric function with a negative real part is often exhibited by the materials with a large concentration of free carriers such as metals or heavily doped semiconductors.

1.2.2 Free Carrier Contribution to the Dielectric Function

The dielectric function of degenerately doped semiconductors can be constructed from Drude-Lorentz model in which free carriers were treated as damped harmonically oscillating particles around the lattice atoms in the external electric field ($\mathbf{E}$) of an electromagnetic wave. In this classical theory, the electric displacement field ($\mathbf{D}$) is defined as:[73]

$$\mathbf{D} = \varepsilon_{opt}\varepsilon_0\mathbf{E} - \frac{Ne^2\mathbf{E}}{m^*(\omega^2 + i\gamma\omega)} \qquad \textbf{(Equation 1.3)}$$

where ε_{opt} is the dielectric constant measured in the transparent region of the spectrum of an undoped semiconductor ($\varepsilon_{opt} \approx n^2$, where n is the refractive index), ε_0 is the permittivity of the free space, ω is the frequency of light, m^* is the effective electron mass, e is the electron charge, N is the free electron concentration, and γ is the damping constant. The dielectric function $\varepsilon_D(\omega)$ is related to $\mathbf{D}$ through the following equation:

$$\varepsilon_D(\omega) = \varepsilon_{opt}\left(1 - \frac{{\omega_p}^2}{\omega^2 + i\gamma\omega}\right) \qquad \textbf{(Equation 1.4)}$$

where ω_p is plasma frequency. In some literature, ε_{opt} is noted by the high frequency dielectric constant ε_∞. By equation (1.4), the plasma frequency has a square root dependence on the free electron concentration:

$$\omega_p = \left(\frac{Ne^2}{\varepsilon_{opt}\varepsilon_0 m^*}\right)^{1/2} \qquad \textbf{(Equation 1.5)}$$

The absorption coefficient (α) has a linear relationship with the free electron concentration:

$$\alpha = \frac{\varepsilon_{opt}{\omega_p}^2}{nc\omega^2\tau} = \frac{Ne^2}{m^*\varepsilon_0 nc\tau\omega^2} \qquad \textbf{(Equation 1.6)}$$

where c is the speed of light and τ is the damping time. The Drude-Lorentz model has been successfully applied to predict the conductivity of semiconductor materials and the optical properties of plasmonic semiconductor NCs. Based on the Drude-Lorentz model, degenerately doped semiconductor NCs, with the carrier concentration ranging from 10^{19} cm^{-3} to 10^{22} cm^{-3}, the LSPR absorption should occur in the NIR and MIR region, perhaps even at far IR region as shown in Figure 1.5.

In addition to free electron concentration, another important parameter in Drude-Lorentz model is the damping constant (γ) which quantifies the optical loss of the LSPR and dictates the broadening of absorption spectrum. The damping of carrier oscillations can arise from different scattering processes in semiconductors and can be described as:[74-75]

$$\gamma = \sum \gamma_i = \gamma_{e-e} + \gamma_{e-ph} + \gamma_{e-ion} + \gamma_s + \gamma_{ib} + \ldots \qquad \textbf{(Equation 1.7)}$$

Where γ_{e-e} represents the electron-electron scattering; γ_{e-ph}, the electron-phonon scattering; γ_{e-ion}, the electron-ionized impurity scattering; γ_s, the surface scattering; γ_{ib}, the interband scattering.

[¶]Reprinted by permission from Macmillan Publishers Ltd: [Nat. Mater.] (Luther, J. M.; Jain, P. K.; Ewers, T.; Alivisatos, A. P. 2011, 10, 361-366), Copyright (2011).

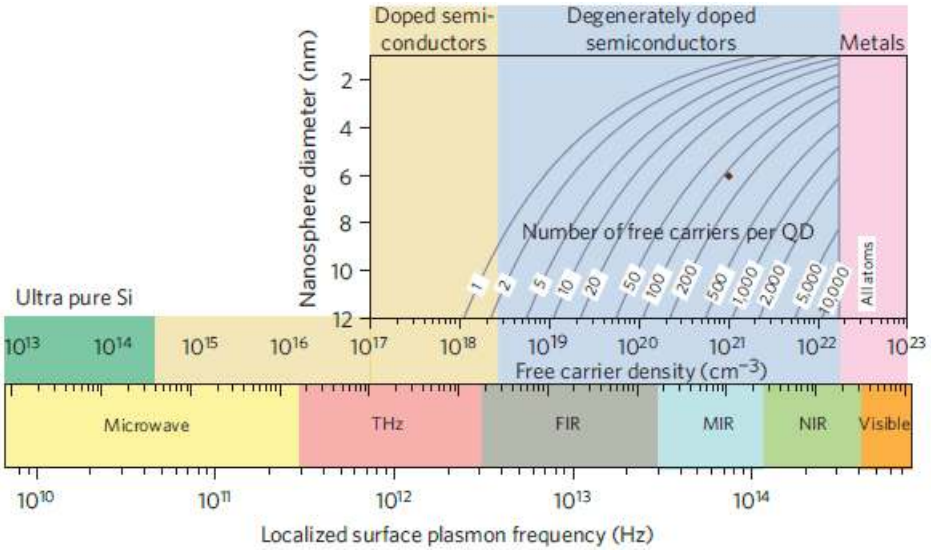

Figure 1.5 Calculated localized surface plasmon resonance (LSPR) frequency dependence on free carrier density based on Drude model (bottom panel); and calculated number of dopant atoms required for nanoparticle sizes ranging from 2 nm to 12nm to achieve free carrier density between 10^{17} and 10^{23} cm^{-3} (top panel).[8¶]

1.2.3 Limitations of Drude-Lorentz Model

Although Drude-Lorentz model has been proved to be valid for many plasmonic semiconductor NCs, there are several exceptions in which the experimental results do not agree with the Drude-Lorentz model. One of the discrepancies comes from the band structure dispersion. As indicated in Equation 1.5, the Drude-Lorentz model assumes the effective mass of electron does not change with the carrier concentration which is plausible for material with a parabolic conduction band. However, for the material with non-parabolic conduction band, the effective mass [$m^*(k_l)$] depends strongly on the value of the wavevector (k_l) associated with each electron:[38]

$$m^*(k_l)m_0 = \frac{\hbar^2 k_l}{dE_{CB}/dk} = \frac{\hbar k_l}{v_g} \qquad \textbf{(Equation 1.8)}$$

Where m_0 is the electron rest mass, $\hbar$ is Planck's constant, E_{CB} is the specific energy state for a given wavevector, and v_g is the electron group velocity. In the linear dispersion regime, v_g is constant and thus the effective mass of the electron linearly depends on k_l . With increasing free carrier concentration, the free carrier occupies the energy state with high wavevector will have large effective

mass. As a result, the plasmon frequency dependence on the free electron concentration will become less pronounced which has been demonstrated in InN NCs for which the LSPR frequency almost remains unchanged when the carrier concentration is tuned by the redox titration.[38] Similar behavior of LSPR was also observed in oxygen-deficient TiO_2 NCs.[76]

The other discrepancy is related to the quantum confinement associated with small sized NCs. As mentioned above, Schimpf *et al.* observed a blue shift of LSPR in ZnO NCs with decreasing sizes in the quantum confinement regime.[63] In contrast, based on Drude-Lorentz model, the LSPR frequency should red shift as the NCs size decreases due to the higher damping associated with surface scattering. In order to model LSPR in quantum confined ZnO NCs, quantum confinement was introduced, in addition to incident electric field, to the restoring force acting on electrons, resulting in a set of available transition frequencies, ω_{if} ,where i and f are designations for the initial and final quantum states, contributing to the total dielectric function. The modified dielectric function was defined as:

$$\varepsilon(\omega) = \varepsilon_{IB}(\omega) - {\omega_p}^2 \sum_{i,f} \frac{s_{if}}{\omega^2 - {\omega_{if}}^2 + i\gamma\omega} \qquad \textbf{(Equation 1.9)}$$

Where ε_{IB} is contributions from interband transitions, ω_p is bulk plasma frequency, s_{if} is the oscillator strength, γ is the size-dependent scattering frequency. Using this modified dielectric function, the calculated optical properties agree well with experimental data. Jain developed the "plasmon-in-a-box" model to study the evolution of optical transitions in quantum confined NCs with increasing number of free electrons.[77] At low density regime (several electrons per NC), intraband transition is dominant. Adding more electrons leads to the coexistence of individual intraband excitation and the LSPR transitions. With even higher electron concentration, the individual electrons can overcome the confinement and participate fully in LSPR excitation. The conclusion was later experimentally demonstrated using HgS QDs by Shen *et al.*[39]

1.3 Magnetic Circular Dichroism of LSPR

The active control of optical and electronic properties of semiconductor materials by external magnetic field is attractive for many potential computing and data storage technologies.[78] Plasmonic semiconductors with diverse optical and electronic properties are very intriguing candidates for the magneto-optical investigations. The magnetoplasmonic effect was first demonstrated in noble metal/ferromagnetic metal heterostructures through the optical Kerr effect.[79-80] Pineider *et al.* extended

the magneto-optical measurement to MCD spectroscopy and observed the magnetoplasmonic modes on colloidal Au NPs.[81] Schimpf *et al.* performed the MCD measurement on photocharged ZnO NCs and used the MCD spectra as the signature to assign the IR absorption to LSPR.[63] Later, they reported large MCD signals of ITO NCs demonstrating the generality of magneto-optical response of LSPR.[62]

When excited by circularly polarized light, cyclotron LSPR modes are generated, with the rotation direction determined by the light polarization. In the absence of an external magnetic field, the two cyclotron plasmonic modes, corresponding to excitation by left and right circularly polarized light, are degenerate. However, in an external magnetic field applied parallel to the light propagation direction, the degeneration is lifted resulting from the total force ($\mathbf{F}$) acting on the electrons that collectively oscillate in cyclotron motion:

$$\mathbf{F} = -e\mathbf{E} - e(\mathbf{v} \times \mathbf{B}) \qquad \textbf{(Equation 1.10)}$$

where e and $\mathbf{v}$ are the charge and velocity of the electron, respectively, and $\mathbf{E}$ and $\mathbf{B}$ are external electric and magnetic field, respectively.

The difference between the absorption of left and right circularly polarized light by these magnetoplasmonic modes results in derivative-shaped MCD signal (Figure 1.6). The shift in frequency of the magnetoplasmonic modes ($\Delta\omega$) for a given magnetic field strength (B) relative to zero-field LSPR frequency (ω_0) is given as:

$$\Delta\omega = \left|\omega_B - \omega_0\right| = g(\omega_0)B \qquad \textbf{(Equation 1.11)}$$

where ω_B is the frequency of the magnetoplasmonic mode (ω_B^-, ω_B^+) and $g(\omega_0) = -e/2m$ is the proportionality constant. It follows from the equation (11) that the universal behaviors of LSPR MCD signal are linearly dependent on the magnetic field and independent on temperature.

Using MCD spectroscopy, Hartstein *et al.* accurately predicted the intrinsic NC electronic structure parameters, such as the type of free carriers and their effective mass.[82]

[‡]Reprinted with permission from (Yin, P.; Hegde, M.; Garnet, N. S.; Tan, Y.; Radovanovic, P. V., Nano Lett. **2019**, 19, 6695-6702). Copyright (2019) American Chemical Society.

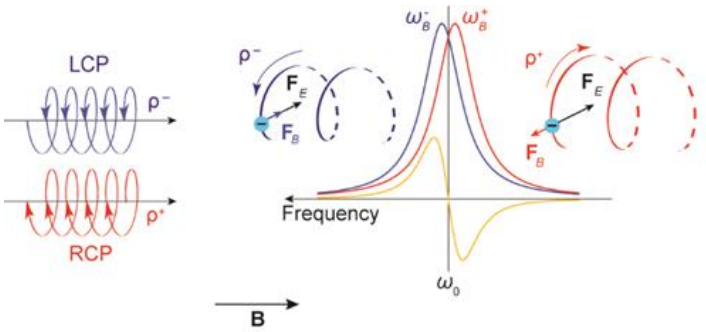

Figure 1.6 Schematic representation of the origin of LSPR MCD of plasmonic NCs. The derivative-shaped MCD intensity (yellow line) is a result of the difference between the absorption of left circularly polarized light (LCP, blue line) and right circularly polarized light (RCP, red line) having ρ^- and ρ^+ helicity, respectively, for magnetic field (**B**) oriented parallel to the light propagation direction. In an external magnetic field the two degenerate LSPR modes having frequency ω_0 split, giving rise to modes with resonance frequencies.[76]

1.4 Interaction between Plasmon and Quasiparticles

From the quantum mechanical point of view, a plasmon is quantization of plasma oscillation of free electron gas density and can be viewed as a quasiparticle.[83] Thus, within the energetic proximity, a plasmon can interact with other quasiparticles which offers exciting opportunities for new scientific discoveries and technological applications.

1.4.1 Plasmon-Phonon Interaction

The plasmon-phonon coupling has received broad attention in 1960s as it saw the surge of research interest in III-V semiconductors.[84-87] The heavily doped III-V semiconductors could possess free electron density on the order of 10^{18} cm^{-3} which is capable of generating the plasmon resonance in the THz regime.[87] The optical phonons also locate in the same regime. The interaction between plasmon and phonon mediates the carrier lattice energy exchanges and thus plays a very important role in the transport properties of III-V semiconductors.[88] Resonant Raman spectroscopy studies of heavily doped III-V semiconductors,[85,88] such as GaAs and InN, thin film suggest that the electrostatic coupling of polarized longitudinal optical (LO) phonons with the surrounding charge carriers (plasmons) result in the formation of the so-called L^+ and L^- coupled phonon-plasmon modes. The plasmon-phonon coupling is maximized when the LO phonons resonate with the plasmons. At high doping levels, the

frequency of both L^+ and L^- modes depend on the free carrier concentration (Figure 1.7). With increasing carrier concentration, the L^+ mode eventually converges to the plasmon mode, while the L^- mode approaches to the transverse optical (TO) phonons. Recently, Faust *et al.* performed the resonant Raman spectroscopy studies of Cu doped InAs NCs and observed similar results.[89] The phenomena were also reported in metal oxides, such as CdO,[90] ZnO,[91] and CeO_2,[92] in which the plasmon mode can couple with multiple LO phonon modes and even the surface phonon modes. With the recent discovery on the chiral phonon and its associated angular momentum,[93-94] the plasmon-phonon coupling could have more profound impact in the next generation electronic devices.

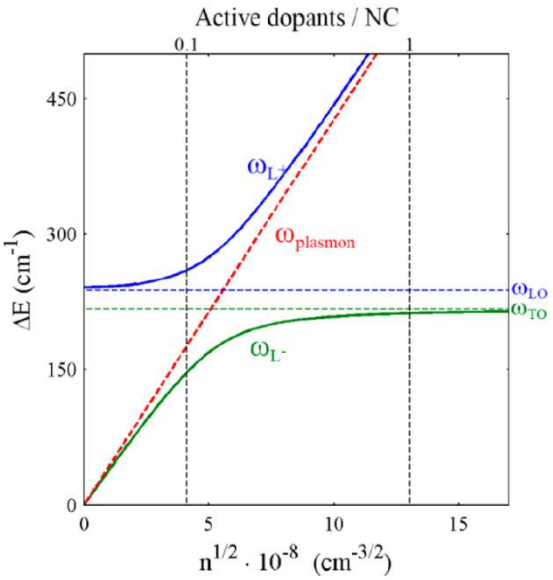

Figure 1.7 Calculated Raman shift of the coupled phonon−plasmon L^+ (blue solid line) and L^- (green solid line) modes versus the square root of the free electron concentrations for InAs NCs. The LO and TO phonon frequencies are indicated by horizontal blue and green dashed lines, respectively. The dashed red line represents the dependence of free plasmon energy on the square root of carrier concentration. The carrier concentrations equivalent to 0.1 and 1 electrons per NC are indicated by the vertical black lines.[89]**

Reprinted with permission from (Faust, A.; Amit, Y.; Banin, U., J. Phys. Chem. Lett. **2017, *8*, 2519-2525). Copyright (2017) American Chemical Society.

1.4.2 Plasmon-Exciton Interaction

Plasmon-exciton interaction has attracted broad attention after the demonstration of enhanced photon absorption/emission of dye molecules by adjacent metal NPs.[95] For extensively studied organic molecules and semiconductor materials, the excitonic transitions often lie in the visible spectrum regime which requires the LSPR in the same energy range for the resonant plasmon-exciton coupling. Thus, the plasmon-exciton interaction is primarily investigated using heterostructures with metal NPs or thin films as plasmonic components.[96-98] The interaction can be classified as a weak or strong coupling depending on the perturbation between exciton wavefunction and the plasmonic electromagnetic modes.[97]

In the weak coupling regime, the plasmon-exciton coupling was described as the interaction between the strong electromagnetic field of LSPR and the exciton dipole which could potentially lead to the enhanced absorption cross-section,[99] increased radiative rate,[100-101] as well as energy transfer between exciton and plasmon.[102] Within the close proximity, the enhanced electromagnetic field in the surface vicinity of metallic nanostructures can be absorbed by the adjacent semiconductor materials or organic molecules, and thus effectively increase the absorption cross section of dye molecules or semiconductors.[103] This phenomenon has been utilized to improve the performance of photodetector and photovoltaics.[3,104] Wang *et al.* studied the angle- and polarization-dependent photoluminescence decay dynamics of CdSe NCs dispersed in the Au disk array and observed that the emission decay of CdSe NCs was accelerated under the resonant conditions.[100] They attributed the radiative rate enhancement to the locally enhanced radiation fields in the vicinity of the Au nanodisks. With the spectral overlap between emission of photo emitter (dye molecules or QDs) and the plasmon absorption of metallic NPs, the nonradiative energy transfer from the exciton to the surface plasmon could lead to the reduction of emission intensity and significant shortening of the emission lifetime.[105-107] The exciton-plasmon energy transfer is strongly affected by the distance between photo emitters and the plasmonic nanostructure.[102]

In the strong coupling regime, the strong perturbation between wave functions will lead to the formation of mixed plasmon-exciton states similar to the aforementioned plasmon-phonon coupling.[97] The excitation energy is shared and oscillates between the plasmonic and excitonic systems. Gómez *et al.* demonstrated the strong coupling between a surface plasmon propagating on a planar silver thin film and the lowest excited state of CdSe NCs.[108] Using the attenuated total reflection measurement, they directly observed two plasmon-exciton mixed states which have a Rabi splitting of ~112 meV at room temperature. Liu *et al.* performed the angle-resolved reflectance microscopy spectra on the

monolayer MoS_2 integrated on the silver nanodisk arrays and observed strong exciton-plasmon coupling with the coupling strength up to 58 meV at 77 K.[109] Recently, Lee *et al.* demonstrated dynamic tuning of exciton-plasmon coupling strength between the strong and weak coupling limits in monolayer MoS_2 with plasmonic nanodisk array assembled in a field-effect transistor. [110]

In addition, using Au/CdSe core-shell nanostructures, Zhang *et al.* demonstrated the plasmon-exciton coupling leads to enhanced optical Stark effect which exhibits polarization dependence and enables the spin manipulation of CdSe NCs.[111] Zhou *et al.* recently probed spin-forbidden dark exciton state in monolayer WSe_2 integrated on single-crystal silver film by using the surface plasmon-assisted near-field spectroscopy based on the near field coupling to the surface plasmon polariton.[112] These examples indicate that the plasmon-exciton coupling in conjunction with other degrees of freedom could open avenues for new optoelectronics that can be used for controlling quantum states in different quantum technologies.

1.5 Multifunctional Materials with Correlating Degrees of Freedom

Semiconductor technology is the main driving force for many scientific and technological breakthrough in 20th century. However, with the advancement of semiconductor industry, Moore's law is approaching its limit and the size of transistors approaching to its physical limitations. A fundamentally new technology is urgently needed in order to keep improving the processing power of semiconductor chips. One of the viable options is utilizing multiple degrees of freedom to process and transfer information,[113] in contrast to relying on charge alone, which is exploited in conventional semiconductor devices. Recently, spintronic and valleytronics emerged as two of the promising candidates for next generation electronic devices.[114-115]

1.5.1 Spintronics

Spintronics studies the active control and manipulation of electron spin electronic property in addition to the charge property in semiconductor devices, which could lead to drastic improvement of the device performance in terms of processing speeds and lower electrical power consumption.[114,116-118] The discovery of giant magnetoresistance (GMR) effect in 1988 brought broad attention to the field of spintronics.[119] GMR was first observed in thin film structures with conductive ferromagnetic layers separated by the nonmagnetic interlayer of which the electrical resistance was low when magnetic moments of the ferromagnetic layers were aligned in parallel, and at maximum when the magnetic moments were antiparallel.[120] Based on the GMR effect, spin valve and magnetic tunnel junction were

developed and incorporated into the electronic devices such as magnetic field sensors, read heads for hard discs, galvanic insulators, and magnetoresistive random-access memory (MRAM).[117] MRAM uses the magnetic hysteresis (coupling between two ferromagnetic layer) to store the data and magnetoresistance to read the data.[121] Compare to traditional electrically erasable programmable read-only memory, the MRAM possesses much fast writing speed, better data retention, as well as much lower power consumption. In addition, other prototype spintronic devices have been designed including the spin polarized light-emitting diode[122] and spin field effect transistor.[123] One of the essential components toward realization of these spintronic devices is finding the suitable semiconductor materials with long range magnetic ordering which catalyzed the research field of diluted magnetic semiconductors.

1.5.2 Diluted Magnetic Semiconductors

Diluted magnetic semiconductors (DMS) refers to the non-magnetic semiconductors doped with a small percentage of magnetic ions, normally transition-metal elements, which induces magnetic ordering, preferable ferromagnetism, in the semiconductor.[124-125] At the early stages, DMSs have been extensively studied using II-VI (CdSe and HgTe),[125] III-V (GaAs and GaN)[126-128] semiconductors as host lattices and Mn as magnetic dopants. In these systems, the magnetic ordering of the host lattice is attributed to the exchange interaction between the s or p electrons of the host lattice and the d-electrons from the magnetic impurities.[125] For the practical use, DMS with Curie temperature (T_C) above room temperature was the focus of the research field. The observed room-temperature ferromagnetism in Co-doped TiO_2 thin films stimulated the wide search of transition metal doped TCO as the candidates for high-T_C DMSs.[129] Wide-bandgap metal oxides, including ZnO, TiO_2, SnO_2, and In_2O_3, have been used as a host lattice for the investigations of diluted magnetic semiconductor oxides (DMSOs).[124,130-134] In DMSOs, the concentration of the magnetic cations is usually very low and well below the limit required for the conventional exchange interaction which traditionally is used to explain magnetic ordering in oxides. Coey *et al.* discussed the ferromagnetic exchange coupling in DMSOs by using a new model of indirect exchange via shallow donors (Figure 1.8).[135] In this model, the shallow donor electrons originated from oxygen vacancies form magnetic polarons which can mediate the magnetic ordering. At low concentration of donors, their hydrogenic orbitals overlap to form the impurity band with localized electrons. As donor concentration increases above the critical concentration, the impurity band states become delocalized. The donor impurity band will become spin-split due to the overlap of

the magnetic polarons. Interaction between the electronic states of the localized 3d impurity band and delocalized donor states lead to an extended hybridized state which result in the high T_C.

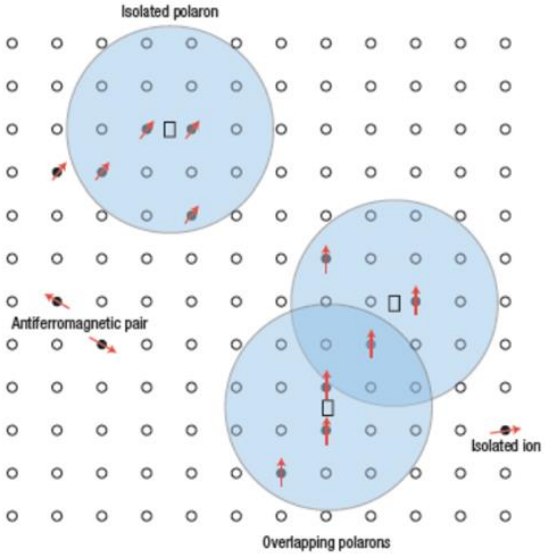

Figure 1.8 Representation of magnetic polarons. A donor electron in its hydrogenic orbit couples with its spin antiparallel to impurities with a 3d shell that is half-full or more than half-full. The figure is drawn for x (concentration of magnetic cations) = 0.1, γ (ratio of hydrogenic radius to Bohr radius) = 12. Cation sites are represented by small circles. Oxygen is not shown; the unoccupied oxygen sites are represented by squares.[135‡‡]

1.5.3 Valleytronics

Valleytronics is an emerging electronic technology which exploits valley degree of freedom in conjunction with electron spin and/or charger for information processing.[136] The valleys, with respect to electronic band structure of semiconductors, are the energy-degenerate conduction band minima which possess different crystal momenta depending on the orientation of crystal axes.[137] The electrons, holes or excitons present in different valleys will be associated with different discrete values of the crystal momentum and thus possess an additional degree of freedom. Many periodic solids have energy-degenerate valleys.[138-140] The active control of valley degree of freedom requires selective populating of certain valley and strong coupling between valley index and the external electric or magnetic field.[136]

---

‡‡Reprinted by permission from Macmillan Publishers Ltd: [Nat. Mater.] (Coey, J. M.; Venkatesan, M.; Fitzgerald, C. B. 2005, 4, 173-179), Copyright (2005).

Thus, the choice of valleytronic materials is significantly limited. The emerging two-dimensional materials such as graphene and monolayer transition metal dichalcogenides (MoS_2, $MoSe_2$, and WSe_2) stimulated the research field of valleytronics.[136] Two dimensional materials normally possess valleys at the inequivalent K and K′ points in the first Brillouin zone due to the broken spatial inversion symmetry (Figure 1.9).[141] In addition, the valleys also exhibit strong valley-selective interactions with applied electric and magnetic fields that arise from the nonequivalent Berry curvature and orbital magnetic moment at K and K′ points.[142-144] The finite orbital magnetic moment possessed by carriers at nonequivalent valleys will result in optical circular dichroism, and thus these carriers can be selectively excited through photons with opposite helicity.[145-147] Currently, the research field of valleytronics is still at its early stage and focus on the valleytronic material growth and characterization. The practical use of valleytronic material in the integrated electronic devices remains a formidable challenge.

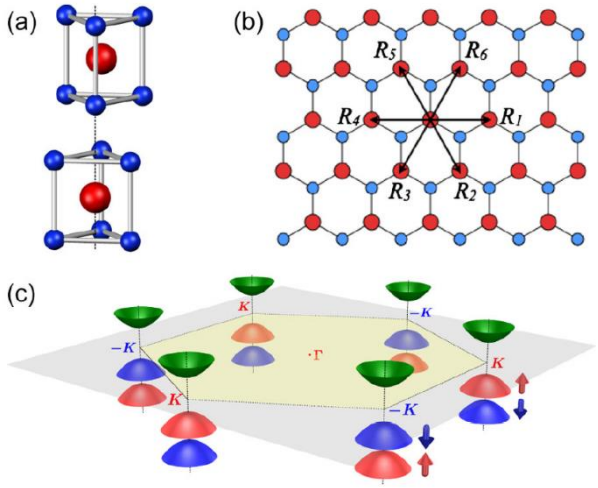

Figure 1.9 (a) The unit cell of bulk MoS_2 with hexagonal symmetry (2H-MoS_2). It contains two unit cells of MoS_2 monolayers, which lacks an inversion center. (b) Top view of the MoS_2 monolayer. (c) Schematic drawing of the band structure at the band edges located at the K points showing parabolic lowest conduction band and spin-orbit split valence band.[141]※

※ Reprinted with permission from: Xiao, D.; Liu, G. B.; Feng, W.; Xu, X.; Yao, W., Phys. Rev. Lett., 108, 196802, 2012. Copyright (2012) by the American Physical Society.

1.6 Motivation and Scope of the Thesis

In addition to electron spin and valleys, there are also collective properties of electrons in semiconductor nanostructures that potentially could be exploited in multifunctional quantum devices. Specifically, plasmonic semiconductor NCs offer an opportunity for interface-free coupling between a plasmon and an exciton. However, non-resonant nature of LSPR and exciton in semiconductor NCs has been a major obstacle toward realizing this opportunity. The possibility of intrinsic (non-resonant) coupling between plasmon and exciton in reduced dimensions is much less explored. After introducing the experimental and theoretical methodologies in Chapter 2, in first part of the thesis, using MCD spectroscopy, we demonstrate a robust electron polarization in degenerately doped In_2O_3 NCs, enabled by non-resonant coupling of cyclotron magnetoplasmonic modes with the exciton at the Fermi level. We performed detailed structural and optical characterizations on In_2O_3 NCs synthesized under different conditions and with varying Sn^{4+} doping concentration, including transmission electron microscopy (TEM), X-ray diffraction (XRD), Raman spectroscopy, UV-vis-NIR absorption spectroscopy and Fourier transform infrared (FTIR) spectroscopy. Furthermore, we used variable-field and variable-temperature MCD spectroscopy to explore the excitonic splitting in In_2O_3 NCs. We show that band splitting has a temperature-independent and a temperature-dependent component, whose ratio that can be controlled by the formation of oxygen vacancies or aliovalent doping of In_2O_3 NCs. Temperature-independent component is associated with splitting of the conduction band states near the Fermi level, caused by the angular momentum of the magnetoplasmonic modes with the opposite helicity. The magnitude of this conduction-band-state splitting is correlated with the LSPR intensity and is predominantly determined by the number of free carriers. However, electron localization on point defect sites results in temperature-dependent spin-induced splitting of the NC band states as the fundamentally different carrier-polarization mechanism**.**

In Chapter 4, we report the synthesis and the direct comparison of the plasmonic properties of Mo and W-doped In_2O_3 (IMO and IWO, respectively) NCs. Molybdenum and tungsten belong to the same group of the periodic table of elements, have almost identical ionic radii for a given oxidation state, and tend to form the same oxidation states, leading to a similar impact on the NC host lattice. However, they have a different dopant activation in In_2O_3 NC allowing for tuning of LSPR energy, intensity, and coherence as demonstrated by a combination of structural and spectroscopic methods, including XRD, TEM, electron dispersive spectroscopy (EDX), X-ray photoelectron spectroscopy (XPS), as well as X-ray absorption spectroscopy (XAS). Comparison of the excitonic MCD spectra of IMO and IWO NCs

having different doping concentrations demonstrates that the excitonic splitting of the NC host lattice increases with increasing LSPR intensity (oscillator strength) and decreasing spectral broadening (dephasing). The results of this work provide additional evidence that excitonic splitting is caused by the magnetoplasmonic modes and give a guideline for the design and optimization of this new class of multifunctional materials.

In Chapter 5, we use MCD spectroscopy to demonstrate unique excitonic splitting patterns in oxygen-deficient TiO_2 NCs enabled by simultaneous control of their faceting and the degree of electron delocalization. The excitonic MCD signal arising from plasmon−exciton coupling has the opposite sign for TiO_2 NCs relative to aliovalently doped In_2O_3 NCs, suggesting the dependence of the plasmon-I induced carrier polarization on the NC electronic structure. Furthermore, controlled reduction of Ti(IV) by oxygen vacancies leads to the formation of Ti(III) sites, which can undergo exchange-coupling processes with the host lattice or neighboring Ti(III) sites. The formation of these Ti(III)-based species by different degree of spatial delocalization of vacancy originated electrons can be controlled by NC morphology together with the LSPR associated with fully delocalized electrons.

In the last chapter (Chapter 6), I summarize our results and provide outlook on the future research directions and prospect of this work. To demonstrate the role of phonon in non-resonant plasmon-exciton coupling, nonstoichiometric InN NCs could be one of the intriguing systems for investigations of the possible plasmon-phonon coupling and its impact on the magnetoplasmon-induced excitonic splitting. In addition, electrochemical tuning of magnetoplasmonic properties and the subsequent carrier polarization will also be important for both comprehensive understanding of the plasmon-exciton interaction in semiconductors and the practical use of plasmonic semiconductor NCs in the optoelectronic devices.

Chapter 2
Experimental Section

2.1 Materials

Indium(III) acetylacetonate ($In(acac)_3$, 98%), tin(IV) chloride pentahydrate ($SnCl_4 \cdot 5H_2O$, 98%) and tungsten hexacarbonyl ($W(CO)_6$) were purchased from Strem Chemicals. Bis(acetylacetonato)dioxomolybdenum(VI) ($MoO_2(acac)_2$), Titanium(IV) fluoride (TiF_4), titanium(IV) chloride ($TiCl_4$, 99.9%), Oleylamine (70 %), and oleic acid (90 %), 1-octadecence (ODE, 90%) 1-octadecanol (ODOL, 95%), Toluene (99.9%) and hexane (98.5%) were purchased from Sigma-Aldrich. All chemicals are used as received without further purification.

2.2 Synthesis and sample preparation

2.2.1 Synthesis of In_2O_3 and Sn^{4+}-Doped In_2O_3 (ITO) NCs

Colloidal In_2O_3 and ITO NCs were synthesized using previously reported procedure.[15,148-149] $In(acac)_3$ (2.2 mmol; 0.9 g) and oleylamine (27 mmol; 7.2 g) were mixed together. The reaction mixture was heated to 250 °C within 1 h and then allowed to react for 1 h in argon or air with continuous stirring. Different atmosphere was used to control the concentrations of oxygen vacancies in synthesized In_2O_3 NCs. The mixture was then slowly cooled to room temperature. After centrifugation at 3000 rpm for 10 min, the precipitate was collected and washed with ethanol three times. The washed precipitate was mixed with 1.5 mL oleic acid and stirred at 90 °C for 30 min. The nanocrystal samples were subsequently precipitated again and washed with ethanol three times. The final product was dispersed in a non-polar solvent, such as hexane or toluene, for further characterization. For the synthesis of Sn^{4+}-doped In_2O_3 NCs, the same experimental procedure was applied in argon atmosphere, but with the addition of varying amount of $SnCl_4 \cdot 5H_2O$ as a doping precursor.

2.2.2 Synthesis of Mo-Doped and W-Doped In_2O_3 NCs

Synthesis of Mo- and W-doped In_2O_3 NCs followed a procedure similar to that described for the ITO NCs. For Mo-doped In_2O_3 (IMO) NCs, all the experimental conditions were kept identical except using $MoO_2(acac)_2$ as dopant precursor. The W-doped In_2O_3 (IWO) NCs were synthesized by using $W(CO)_6$ as dopant precursor with the reaction temperature of 300 °C, while keeping other experimental conditions the same.

2.2.3 Synthesis of TiO_2 NCs

The TiO_2 NCs were synthesized using a modified procedure based on the seeded growth method developed by Gordon *et al*.[27] In a typical synthesis, precursor solution was prepared by dissolving 2 mmol titanium halide (TiF_4 (F), $TiCl_4$ (Cl), or their 1:1 mixture (M)) together with 10 mmol OLAC in 6.8 mL ODE in a glove box. The synthesis was conducted under argon atmosphere using a Schlenk line. In a separate 100 mL three-neck round bottom flask, 30 mmol coordinating ligand (OLAM or ODOL) was mixed with 0.48 mL OLAC and 10.2 mL ODE. The mixture was degassed by heating to 120 °C within 20 minutes and keeping it at that temperature for 1 hour. After degassing, the mixture was cooled to 60 °C before injecting 1.5 mL titanium halide precursor solution. The mixture was then quickly heated to 290 °C and held for 10 min for the crystal seeds to nucleate. The remaining 8.5 mL titanium halide solution was injected into the flask at the rate of about 0.3 mL/min at 290 °C. After that, the mixture was allowed to cool down to room temperature naturally. The product was collected by centrifugation at 3000 rpm for 5 min and redispersed in a small amount of toluene. To purify the product, NCs were precipitated by adding ethanol to the suspension. The washing was repeated three times and the NCs were finally dispersed in hexane, toluene, or chloroform for further characterizations. For notation of different samples, we adopted the designation previously used for these samples, which specifies the precursor and coordinating ligand using the following abbreviations: F-OLAM, M-OLAM, and Cl-ODOL.

2.3 Measurement and Data Analysis

2.3.1 Powder X-ray Diffraction

Powder X-ray diffraction (XRD) is a common characterization method for crystal structure of materials. In addition to the lattice parameter, the crystallite size can also be estimated through the Debye-Scherrer equation:

$$T = \frac{C\lambda}{B\cos\theta} \qquad \textbf{(Equation 2.1)}$$

where T is the crystallite thickness, C is the dimensionless shape factor with the value close to 1, λ is the wavelength of the X-rays (1.54 Å), θ is the diffraction angle in radians, and B is the full-width at half-maximum (FWHM).

The measurements were performed with an INEL XRD diffractometer in Dr. Holger Kleinke's group in Department of Chemistry at the University of Waterloo. The diffractometer is equipped with a position-sensitive detector, utilizing monochromatic Cu-Kα radiation (λ = 1.5406 Å).

2.3.2 Dynamic Light Scattering

The TiO_2 NC sizes were analyzed by dynamic light scattering (DLS). DLS measurements were performed at 25 °C by utilizing a Zetasizer Nano-S90 system (Malvern Instruments) with a laser wavelength of 633 nm positioned at the fixed angle of 90 degrees.

2.3.3 Raman Spectroscopy

Raman spectroscopy was performed at room temperature with a Renishaw 1000 spectrometer using He-Ne laser with the excitation wavelength of 632.8 nm. The radiation source employed was 10% of the total output power (40mW). Prior to the measurement, the spectrometer was calibrated using a silicon foil.

2.3.4 Transmission Electron Microscopy

Transmission electron microscopy (TEM) specimens were prepared by depositing diluted colloidal suspensions of NCs onto copper grids with lacey Formvar/carbon support films purchased from Ted Pella, Inc. TEM imaging and energy dispersive X-ray spectroscopy (EDX) elemental analysis were performed with a JEOL-2010F microscope operating at 200 kV.

2.3.5 UV-Vis-NIR absorption Spectroscopy

Optical absorption spectra were recorded using a Varian Cary 5000 UV-Vis-NIR spectrophotometer in the range of 200 nm to 3300 nm. The measurements were carried out on thin films prepared by drop-casting the NC suspensions onto quartz substrates.

2.3.6 FTIR Spectroscopy

Fourier transform infrared (FTIR) spectra were recorded using a FTIR Bruker Tensor 37 spectrometer. Powder samples were mixed with KBr in approximately 1:50 weight ratio and pressed into pellets for the FTIR measurement.

2.3.7 X-ray Photoemission Spectroscopy

X-ray photoelectron spectroscopy measurements were performed using a Thermo-VG Scientific ESCALab 250 microprobe equipped with a monochromatic Al Kα radiation source (1486.6 eV). Powder samples for XPS measurements were prepared in the same way as for XRD measurements.

The XPS spectra were calibrated against the C 1s peak (284.8 eV) of adventitious carbon. Voigt functions and Shirley backgrounds were used for the peak deconvolution.

2.3.8 X-ray Absorption Spectroscopy

X-ray absorption spectroscopy (XAS) data were collected at Sector 20BM of the Advanced Photon Source (APS).[150]

2.3.8.1 Measurement of Mo K-edge XAS Measurement

The spectra of all IMO NC samples were recorded in the fluorescence detection mode, while the standards (MoO_2 and MoO_3) were recorded in the transmission mode. For measurements at the Mo K-edge, a Rh coated harmonic rejection mirror was set at ~2.5 mrad which implies a high energy cutoff of ~26.8 keV. The Si (111) monochromator was detuned 15% CCW at 20.3 keV. Ultrahigh purity (UHP 5.0) argon was used as the ionization gas in all ion chambers (I_0, I_t, and I_{ref}), and Mo metal foil was used for energy calibration. The samples were made into pellets by mixing ~60-120 mg of sample with ~160-220 mg of boron nitride powder, and subsequently encapsulated in a thin layer of Kapton tape. Fluorescence signal was detected in a standard geometry with the samples oriented 45° relative to the incident X-ray beam, using a 13-element liquid-nitrogen-cooled germanium detector which was positioned 90° to the incident X-ray beam propagation direction.

2.3.8.2 Measurement of W L-edge XAS measurement

The spectra of all IWO NC samples were also recorded in the fluorescence detection mode, and the standards (WO_2 and WO_3) were recorded in the transmission mode. For W L-edge spectra, a Rh coated harmonic rejection mirror was set at 4 mrad. The Si (111) monochromator was detuned 15% at 10.2 keV. A mixture of 50% N2 gas with 50% He gas was used as the ionization gas in the ion chambers. Gallium metal foil was used for energy calibration. Samples weighing ca. 2mg were prepared by pressing the powder into Teflon washer which was then sealed with Kapton tape. Fluorescence signal was collected as described above.

2.3.8.3 Measurement of Ti K-edge XAS measurement

Titanium K-edge XAS spectra were collected in transmission mode using a gaseous ionization detector filled with nitrogen. A titanium foil was used to internally calibrate the energy of the Ti K-edge (6966 eV).

2.3.9 Magnetic Circular Dichroism

2.3.9.1 MCD Experimental Set up

MCD spectroscopy measures the difference in absorption of left and right circularly polarized light. The experimental set up are shown in Figure 2.1.

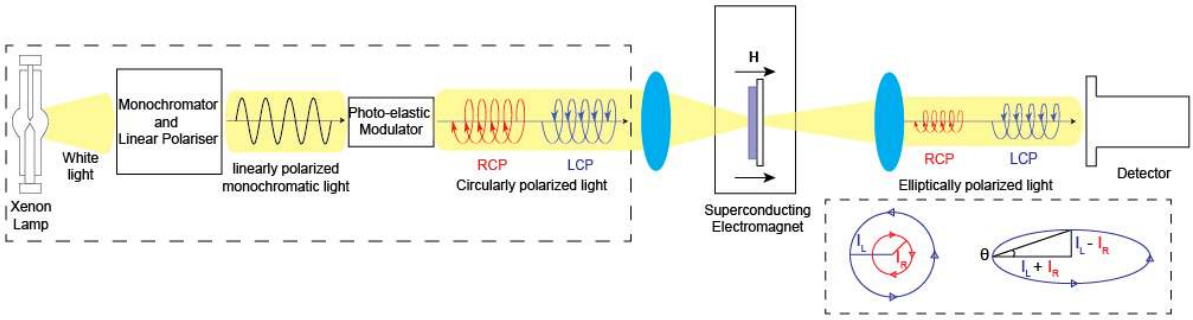

Figure 2.1 MCD experimental set up. A light from a broad-band emitting source is passed through a monochromator and polarizer to generate a monochromatic linearly polarized beam. A portion of this beam is passed through a photoelastic modulator creating left circularly polarized (LCP) and right circularly polarized (RCP) light. A sample is mounted in a superconducting magneto-optical cryostat with the lines of the magnetic field oriented parallel to the light propagation direction. Upon passing through the sample LCP and RCP light are absorbed to a different degree. Different intensities of left and right circularly polarized light (I_L and I_R, respectively) are combined to form an elliptically polarized beam. The ellipticity, θ, is defined as the angle between the long and short axes of the ellipse, and is converted to a differential absorption using eq. (2.3) in section 2.3.9.3.

2.3.9.2 Correlation between Excitonic Splitting and MCD Terms

MCD intensity for a transition from the ground state $|A\rangle$ to an excited state $|J\rangle$ is defined as[151]:

$$\frac{\Delta A}{E} = \left(\frac{2N_0\pi^3\alpha^2 Cl \log e}{250hcn} \right) \mu_B B \left[A_1 \left(-\frac{\partial f(E)}{\partial E} \right) + \left(B_0 + \frac{C_0}{kT} \right) f(E) \right] \quad \textbf{(Equation 2.2)}$$

where ΔA is the differential absorption between left and right circular polarized light, $E = \hbar\nu$, α is the electric permeability, C is the concentration, l is the path length, n is the index of refraction, μ_B is the Bohr magneton, and B is the applied magnetic field. A_1, B_0, and C_0 are known as the MCD $\mathcal{A}$, $\mathcal{B}$, and $\mathcal{C}$ term, respectively, $f(E)$ is the absorption spectrum band shape, and $\partial f(E)/\partial E$ is its first derivative. Under external magnetic field along the light propagation direction (z), the ground and/or excited states are split due to a Zeeman perturbation with a magnitude $-\mu_z B = \mu_B\left(g_L\hat{L}_z + g_S\hat{S}_z\right)B$, where $\hat{L}_z$ and $\hat{S}_z$ are the orbital and spin angular momentum operators, respectively, and $g_L = 1$ and $g_S = 2.002$ are the corresponding gyromagnetic ratios. The overall electron angular momentum responsible for electron polarization is $J = L + S$, with the MCD selection rule $\Delta M_J = \pm 1$ (+1 for left circularly polarized light and -1 for right circularly polarized light).

One of the most reliable ways to experimentally differentiate between different terms is the temperature-dependence of the MCD intensity. $\mathcal{A}$ term MCD occurs in the system which has degenerate excited states. Under magnetic field, the excited states are split due to the Zeeman effect. Since the Zeeman splitting is usually only a few wavenumbers, the two oppositely signed absorption bands will sum to a derivative shape MCD signal, as shown in Figure 2.2a. On the contrary, $\mathcal{C}$ term MCD requires degenerate ground states which undergo Zeeman splitting in the external magnetic field. At low temperatures, kT is comparable to or smaller than the magnitude of the Zeeman splitting in the presence of a strong magnetic field, causing the Boltzmann population of the lower ground state sublevel to be larger than that of the higher-energy sublevel. Hence, two oppositely signed absorption bands will have different intensities, resulting in mostly absorption band shape as shown in Figure 2.2b. $\mathcal{C}$ term MCD is generally associated with the Zeeman splitting due to ground state paramagnetism, and therefore follows temperature dependence characteristic for the Curie law (Figure 2.2c). $\mathcal{C}$ term intensity is generally observed for MCD spectra of diluted magnetic semiconductors.[133,152]

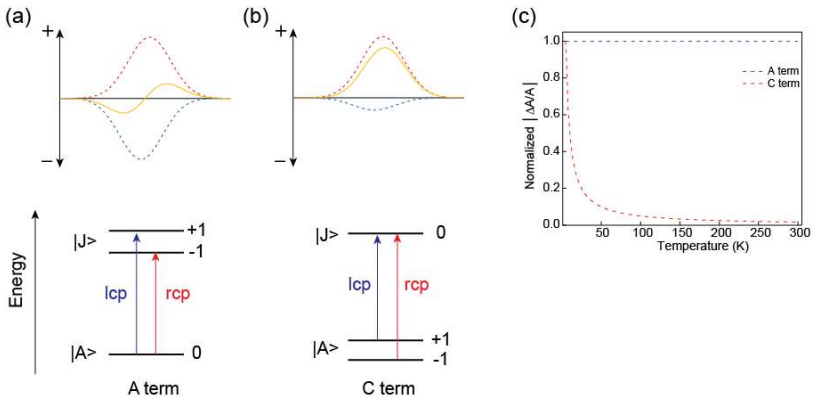

Figure 2.2 Schematic representation of magnetic circular dichroism (MCD) terms. MCD signal (top) and Zeeman splitting (bottom) for $\mathcal{A}$-term (a) and $\mathcal{C}$-term (b) MCD. (c) Comparison of the temperature-dependent $\mathcal{A}$-term and $\mathcal{C}$-term MCD intensity.

2.3.9.3 MCD Measurement and Spectra Analysis

MCD spectroscopic measurements were carried out in Faraday configuration using a Jasco J-815 spectropolarimeter for generating circularly polarized light and signal detection (Figure 2.1). Samples were housed in an Oxford SM 4000 magneto-optical cryostat which allows for variable temperature (1.5 to 300 K) and variable field (0 to 7 T) operation. The NCs were deposited on strain-free quartz substrates by drop-casting the colloidal suspensions in toluene. The MCD intensity (the difference in absorption of left and right circularly polarized light) was expressed as ellipticity (θ, millidegree) of the transmitted light.

The circular polarization of light was defined according to the "optics" convention (i.e., referenced to the detector or looking toward the source). The corresponding MCD spectra were represented as outlined elsewhere.[151,153] MCD intensity is defined as $\Delta A = A_L - A_R$, where A_L and A_R are the absorption of left (ρ^-) and right (ρ^+) circularly polarized light, and represented as a degree of ellipticity (Figure 2.1). The MCD intensities were converted to ΔA/A from ellipticity (θ) using the relationship:

$$\frac{\Delta A}{A} = \frac{\theta}{32982 \times A} \qquad \textbf{(Equation 2.3)}$$

where θ is in millidegree, and A is the band gap absorbance determined from the absorption spectrum simultaneously collected by the CD detector.

Magnetic field dependence of the exciton MCD intensity was obtained from the high-resolution MCD spectra collected at different fields from 1 to 7 T, after the baseline subtraction using the spectrum

collected at 0 T. The corrected field-dependent intensities at the MCD band maximum were fitted to a linear function in B to compare with the field dependence of the MCD intensity for LSPR (Figure 2b, black line). In addition, to clearly distinguish it from the Curie behavior, the magnetic field dependence of the intensity of MCD spectra at band edge energy was also fitted with the spin-only Brillouin function:

$$M_S = \frac{1}{2} N g_S \mu_B \left[(2S+1) \coth\left((2S+1) \frac{g_S \mu_B B}{2 k_B T} \right) - \coth\left(\frac{g_S \mu_B B}{2 k_B T} \right) \right] \quad \textbf{(Equation 2.4)}$$

where S is the spin quantum number, g_S is the corresponding Landé g-factor, B is the external magnetic field, μ_B is the Bohr magneton, k_B is the Boltzmann constant, and T is the temperature. For the fitting, N was treated as the fitting parameter.

For the temperature-dependent MCD intensity measurements, the spectra collected in the absence of magnetic field were used as baselines for correcting the MCD spectra measured at different temperatures from 5 to 300K. The fitting of temperature-dependent MCD intensities for IMO NCs involves the deconvolution of $\mathcal{A}$ term and $\mathcal{C}$ terms from the overall MCD intensity (see the following section for more detailed discussion about $\mathcal{A}$ and $\mathcal{C}$ terms). The $\mathcal{C}$ term MCD intensity vanishes almost completely at high temperatures, and the MCD intensity measured at room temperature was taken as the $\mathcal{A}$ term contribution only. The maximum exciton MCD intensity at 300 K was subtracted from the maximum intensities measured at all other temperatures to obtain the temperature dependence of the $\mathcal{C}$ term which was fitted with the Curie-type relationship:

$$\chi = \frac{C}{T - T_C} \qquad \textbf{(Equation 2.5)}$$

where χ is magnetic susceptibility, T_C is the Curie temperature, T is temperature ranging from 5 to 300 K, and C is the material-specific Curie constant. Adding A term intensity (300 K) to the fitting curve for $\mathcal{C}$ term intensity reproduces very well the temperature dependence of the overall MCD intensity.

For deconvolution of the MCD peaks of M-OLAM sample, a Voigt function was used to fit the 7 T MCD spectrum collected at 300 K to obtain the peak profile for the excitonic transition. The peak position and band width obtained from this fitting were kept unchanged for fitting the spectra at

different magnetic field strengths and temperatures. The second Voigt function was added to achieve the best fitting of the negative band in the range from 2.26 to 4.5 eV. Practically unchanged peak position and band width of the second Voigt function indicated that peak devolution was reasonable. The different profile of the deconvoluted peaks can be attributed to different characteristics of the excitonic and charge transfer transitions.

2.3.10 Magnetization Measurement

Magnetization measurements were performed using a Physical Property Measurement System (PPMS, Quantum Design Model 6000). For the measurement of free-standing NCs, the colloidal samples were precipitated with ethanol, dried, and loaded into the sample capsules. The measurements were made at 2 K with magnetic field ranging from 0 to 9 T.

2.3.11 Electron Paramagnetic Resonance Measurement

Electron paramagnetic resonance (EPR) spectra were collected for powder samples using a Bruker X-band EMXmicro spectrometer equipped with EMX standard resonator and ESR900 continuous flow cryostat (Oxford Instruments) for temperature control. The EPR spectra were obtained at 80 K with the incident microwave frequency of 9.39 GHz, power of 0.63 mW, and modulation amplitude of 4 Gauss by averaging 4 scans.

For the analysis of EPR spectrum of M-OLAM sample, a Lorentzian function (red dashed line in Figure 5.14a) was used to simulate the broad background associated with mutually interacting Ti^{3+} ions, and subtracted from the spectrum to obtain the EPR signal associated with isolated Ti^{3+} ions (blue dashed line in Figure 5.14a).

2.3.12 Density Functional Theory (DFT) Calculations

2.3.12.1 DFT Calculations of Stoichiometric and Oxygen-Deficient In_2O_3 and ITO

The DFT electronic structure calculations were performed within the plane wave self-consistent field approximation using Quantum Espresso code.[31] The generalized gradient approximation (GGA) contained in the Perdew-Burke-Ernzerhof (PBE) exchange correlation functional was used in the calculations. Norm-conserving pseudopotentials were used, with the energy cut-off value of 80 Ry and semicore In 4d states included in the valence electrons. As a first step of the calculation, geometric optimization of the 80 atom In_2O_3 supercell was performed in such a way that the total energy of the system is less than 10^{-4} Ryd and total force on each atom less than 10^{-3} Ryd/a.u. For geometric

optimization Brillouin zone sampling was done using 2×2×2 Monkhorst-Pack (MP) grid. For simulation of the ITO band structure, a Sn dopant was placed in an In b-site (doping concentration ~3.125 %). The electronic structures of In_2O_3 and ITO containing oxygen vacancies were performed by removing one of the O atoms from the supercell to create a defective cell. For both pure and doped In_2O_3, equilibrium lattice parameter obtained from the geometric optimization procedure was used for self-consistent field (SCF) calculations. For SCF calculations, a MP grid of 4×4×4 was used.

2.3.12.2 DFT Calculations of IMO and IWO

The DFT calculations were performed for an In_2O_3 supercell consisting of 80 atoms with the functional forms mentioned above. In order to overcome a problem with band gap underestimation within the PBE-GGA approximation, Hubbard correction parameter (U) was used. Hubbard corrections of U=7.0 eV for In 4d electrons and U=5.9 eV for O 2p electrons were used, respectively. As the first step of calculation, In_2O_3 supercell was fully relaxed using 2×2×2 MP k-point mesh. Fully optimized cell was used for further calculations. Mo- and W-doped In2O3 were simulated by replacing one of the In atoms residing in the b-site. Self-consistent field (SCF) calculations were performed using 4×4×4 k-point mesh. A denser grid of 6×6×6 k-point grid was used for non-self-consistent filed calculations.

2.3.12.3 DFT Calculations of Stoichiometric and Oxygen-Deficient Anatase TiO_2

The electronic structure of oxygen vacancies in anatase TiO_2 was simulated using the plane-wave density functional theory within GGA+U (Hubbard U correction) approximation as developed in Quantum-ESPRESSO package.[154] The anatase TiO_2 supercell of 108 atoms (3×3×1) was constructed for the calculations. Norm-conserving pseudopotential along with U-corrected PBE exchange-correlation functional with plane-wave cutoff energy of 80 Ry was used in calculations.[155] The Hubbard U correction of 3.2 eV on Ti 3d electrons and 2.0 eV on O 2p electrons were used to overcome strong Ti 3d and O 2p coupling.[156] The 108 atoms supercell was relaxed in such a way that total force on each atom is less than 10^{-3} Ry/a.u. and total energy of the system less than 10^{-4} Ry. The O vacancy was created by removing one of the oxygen atoms from the supercell. For geometrical optimization total energy was calculated using 1×1×1 MP k-point mesh (from Γ point). The equilibrium lattice parameters obtained from the geometrical optimization procedure were used for further calculations. For self-consistent and non-self-consistent calculations, a denser MP grid of 2×2×2 was used.

Chapter 3
Plasmon-Induced Carrier Polarization in Sn doped In_2O_3 Nanocrystals

In this part of my thesis I demonstrate a robust electron polarization in degenerately doped In_2O_3 NCs. This chapter presentsdetailed structural, optical, and magneto-optical characterizations of In_2O_3 NCs synthesized under different conditions and with varying Sn^{4+} doping concentrations, including XRD, TEM, absorption spectroscopy (UV-vis-NIR and FTIR) and MCD spectroscopy investigations. The results show that band splitting of In_2O_3 NCs has a temperature-independent and a temperature-dependent component, whose ratio that can be controlled by the formation of oxygen vacancies or aliovalent doping of In_2O_3 NCs. This chapter is adapted from the following publications:

Yin, P.; Tan, Y.; Fang, H.; Hegde, M.; Radovanovic, P.V. "Plasmon-Induced Carrier Polarization in Semiconductor Nanocrystals" *Nat. Nanotechnol.* **2018**, *13*, 463-467. Copyright © 2018, Macmillan Publishers Limited.

Yin, P.; Hegde, M.; Tan, Y.; Chen, S.; Garnet, N.; Radovanovic, P. V. "Controlling the Mechanism of Excitonic Splitting in In_2O_3 Nanocrystals by Carrier Delocalization" Copyright © 2018, American Chemical Society.

3.1 Structural Information of In_2O_3 and ITO NCs

The synthesis of colloidal In_2O_3 NCs was performed by non-injection method in an inert atmosphere (argon gas) and under oxidizing conditions (in air) to control the oxygen deficiency in the NC lattice (see Experimental Section 2.2.1 for details). For the synthesis of indium tin oxide (ITO) NCs, varying amounts of $SnCl_4$ (1-15 mol%) were added to the reaction mixture, and the reaction was allowed to proceed under the flow of argon. As shown in Figure 3.1, the In_2O_3 NCs synthesized in air have a smaller average size and larger size distribution than those synthesized in argon, implying that the oxidizing environment tends to inhibit the NC growth. This process might be associated with the adsorption of byproducts obtained by partial oxidation of oleylamine as a coordinating solvent. On the other hand, the growth of NCs in the presence of Sn^{4+} as an impurity ion, does not significantly influence the NC growth, at least for moderate doping concentrations relevant for this work. All NC samples, undoped and doped, obtained under described conditions exhibit cubic crystal structure characteristic for bixbyite-type In_2O_3 (Figure 3.2a). A notable increase in the broadening of the XRD

peaks for air-synthesized In_2O_3 NCs is consistent with their smaller average size relative to other samples. The compositions of ITO NCs, determined by X-ray photoelectron spectroscopy (XPS), are very similar to those we reported previously for the same starting precursor concentrations, and I use their nominal composition throughout this Chapter. Figure 3.2b shows Raman spectra of different In_2O_3 and ITO NC samples from this study. The spectra for In_2O_3 NCs show four phonon peaks characteristic for bcc-In_2O_3 (307, 366, 497, and 630 cm^{-1}).[148,157] These peaks are somewhat sharper and better defined for NCs synthesized in argon, indicating larger surface area to volume ratio and NC size distribution of air-synthesized NCs. Upon doping with Sn^{4+} ions the peaks broaden and decrease in intensity, completely disappearing for doping concentrations above ca. 10 %. This phenomenon has been associated with the local crystal lattice distortion due to the incorporation of Sn^{4+} dopants into In_2O_3 NCs.[15] Similar findings were made by FTIR spectroscopic measurements (Figure 3.3).

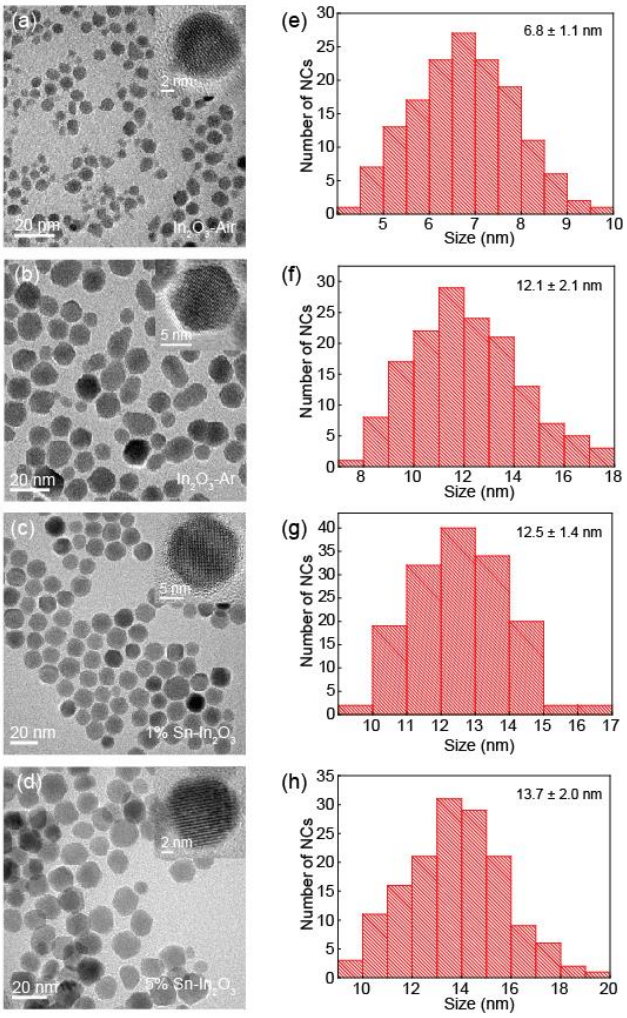

Figure 3.1 (a-d) TEM images of In_2O_3 NCs synthesized in air (a) and argon (b) and ITO NCs having 1 % (c) and 5 % (d) Sn^{4+} doping concentration. (e-h) Corresponding NC size distribution histograms. The average NC sizes are shown as insets.

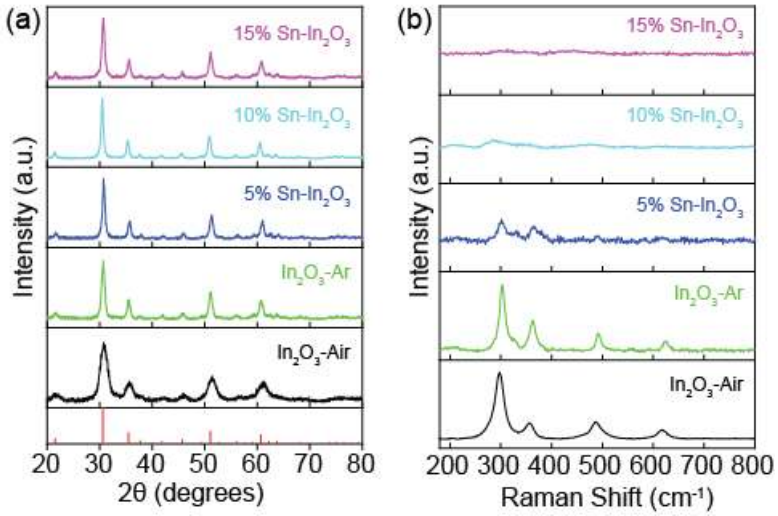

Figure 3.2 (a) XRD patterns and (b) Raman spectra of In_2O_3 NCs synthesized in air (black trace) and argon (green trace) and ITO NCs having different compositions, as indicated in the graph. Vertical lines in Panel (a) indicate the bulk XRD pattern of cubic bixbyite-type In_2O_3.

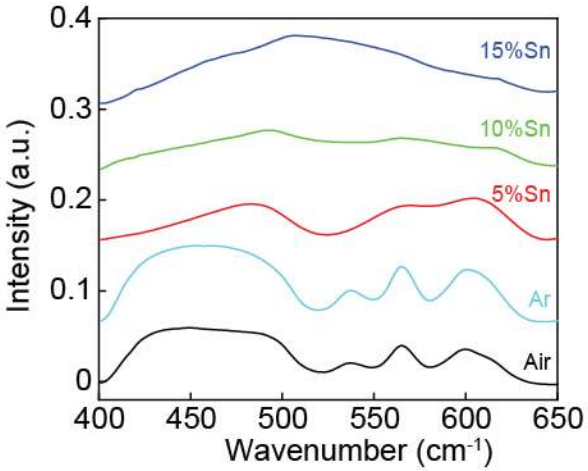

Figure 3.3 Fourier-transform infrared spectra of In_2O_3 NCs synthesized in air (black trace) and argon (light blue trace) and ITO NCs having different Sn^{4+} doping concentrations as indicated in the graph. The observed spectral features correspond to the In−O phonon modes characteristic of cubic In_2O_3.

These peaks broaden and decrease in intensity, similarly to Raman spectra, indicating increased local lattice distortion with increasing doping concentration.

3.2 Optical Properties of In_2O_3 and ITO NCs

The absorption spectra of NCs in Figure 3.2 are shown in Figure 3.4. In the NIR range all ITO NCs exhibit a broad LSPR band that shifts to higher energy with increasing doping concentration (Figure 3.4a). As summarized in Table 3.1, the carrier density in these NCs can be calculated from the plasma frequency, estimated as the LSPR band maximum, using Drude-Lorentz model (Eq. 1.5).

Table 3.1 Free carrier concentrations for four representative samples calculated from LSPR peak energy using Drude-Lorentz model.

Sample	Peak Energy (eV)	Carrier Density (cm^{-3})
In_2O_3-Ar	0.136	1.61×10^{19}
5% Sn-In_2O_3	0.322	9.05×10^{19}
10% Sn-In_2O_3	0.454	1.80×10^{20}
15% Sn-In_2O_3	0.648	3.66×10^{20}

All LSPR spectra of ITO NCs are broad and asymmetric, suggesting homogeneous distribution of Sn^{4+} ions throughout the NCs.[57] Surprisingly, the undoped In_2O_3 NCs synthesized in argon also show a small but clearly observable LSPR band in the MIR, centered at 0.136 eV (light blue trace in Figure 3.4a and Appendix A). The carrier density in these NCs, determined using eq. 1.5, is 1.6×10^{19} cm^{-3}, which corresponds to about 15 extra electrons per NC with an average size of ca. 12 nm. Unlike dopant-originated conduction band electrons in case of ITO NCs,[158] the most likely source of these extra electrons is oxygen vacancies, which are readily formed in bulk and on surface of transparent metal oxides.[21,159-160] However, to our knowledge, LSPR in non-stoichiometric In_2O_3 NCs has not been reported. To confirm this hypothesis, we measured the absorption spectrum of In_2O_3 NCs prepared under oxidizing conditions to reduce the probability of oxygen vacancy formation and minimize their concentration (black trace in Figure 3.4a). Besides the sharp vibrational overtones associated with the solvent molecules and/or coordinating ligands,[161] no LSPR can be detected, confirming the absence of multiple free electrons. It has been shown that as few as 3-4 delocalized carriers can undergo collective oscillation and give rise to LSPR in In_2O_3 NCs of similar size,[12] suggesting that any electrons associated

with oxygen vacancies in these NCs are highly localized. An increase in the concentration of free electrons due to NC synthesis in an inert atmosphere and introduction of Sn^{4+} aliovalent dopants is also evident from the blue shift of the apparent band edge absorption in Figure 3.4b (Burstein-Moss shift).

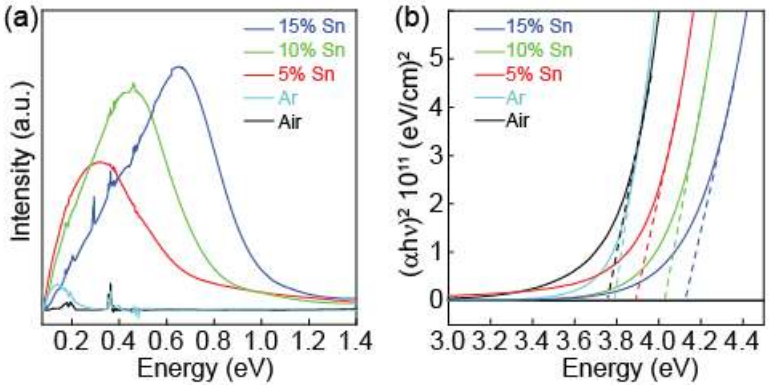

Figure 3.4 (a) LSPR absorption spectra of In_2O_3 NCs synthesized in air (black trace) and argon (light blue trace) and ITO NCs having different doping concentrations, as indicated in the graph. (b) Tauc plots of NCs in (a) used to determine optical band gaps.

3.3 Carrier polarization in ITO NCs

We used MCD spectroscopy in Faraday configuration to examine the excitonic properties of ITO NCs (see Experimental section 2.3.9). Figure 3.5a (blue trace) shows 300 K absorption spectrum of ITO NCs containing 10 mol% Sn^{4+} in the visible range. MCD spectrum of In_2O_3 NCs synthesized under similar conditions and collected at 300 K and 7 T (red trace) shows no measurable intensity. However, variable-field MCD spectra of ITO NCs (black and dashed traces) are dominated by negative bands that coincide with the nanocrystal band edge absorption. The intensity of the MCD band maximum at ca. 4.34 eV is plotted as a function of magnetic field in Figure 3.5b (black squares). The band gap MCD intensity is linearly dependent on the magnetic field, as evident from the best linear fit to the experimental data (blue line), identically to the MCD intensity of LSPR. The Brillouin function fit to the same data for the spin state S =1/2 and the electron spin Landé g-factor g_S =2.002 (red dashed line) shows significant deviation from the experimental data confirming that the observed field dependence is not associated with the Curie-type paramagnetism. Another unusual signature behavior of the cyclotron magnetoplasmonic modes is the temperature independence of their MCD intensity − it has been found that the LSPR MCD intensity remains temperature independent at least up to 30 K.[62-63]

Figure 3.5c shows 7 T MCD spectra of ITO NCs in the optical band gap region collected at various temperatures from 5 to 300 K. All spectra are essentially identical attesting to the temperature independence of the excitonic MCD intensity. The field and temperature behaviors of MCD signal are specific to cyclotron motion of free electrons. Individual free or weakly bound carriers in an external magnetic field give rise to spin-split Landau levels, owing to their cyclotron oscillations. However, the absorption and MCD spectra involving quantized Landau levels are generally observed at low temperatures and high magnetic fields and, in contrast to our observations, have a specific oscillatory pattern (see Appendix B). The results of Figure 3.5 imply that exciton MCD spectra of ITO NCs are associated with the cyclotron magnetoplasmonic oscillations as a collective electronic property, and involve electronic band state splitting rather than intraband sublevels. This is a surprising result because plasmon and exciton are non-resonant, and LSPR is not directly excited in these measurements. Furthermore, unlike classically treated plasmon oscillations, the excitonic absorption involves transition between discrete quantum levels, suggesting the magnetoplasmonic-mode-induced splitting of the nanocrystal band states.

Variable-temperature MCD measurements are very helpful in addressing the nature of band splitting in semiconductor NCs. Specifically, the temperature independence of MCD intensity, characteristic for the $\mathcal{A}$ term, is associated with the lack of ground state splitting (see Experimental section 2.3.9).[153] Zeeman perturbation, represented as $\mu_B(\hat{L}+2\hat{S})\mathbf{B}$, where $\hat{\boldsymbol{L}}$ and $\hat{S}$ are the orbital and spin angular momentum operators, respectively, leads to splitting of the lowest unoccupied conduction band states. In the absence of any source of paramagnetism, the total angular momentum is due to the orbital angular momentum (i.e., $J = L = 1$), with the Zeeman energy of the split states given by $E_{Zeeman} = \mu_B M_J B$, where $M_J = \pm 1$. Taken together, the field and temperature dependent measurements suggest that the cyclotron magnetoplasmonic modes impart significant orbital angular momentum to the nanocrystal excited state, leading to the formation of oppositely polarized electronic states around the Fermi level (Figure 3.5d). Importantly, the appearance of MCD signal with a singular sign (in this case negative) indicates complete polarization of the carriers by the magnetoplasmonic modes.

In analogy to emerging electronic technologies that rely on different degrees of freedom for achieving the polarization of charge carriers, including spintronics (electron spin) and valleytronics (discrete values of crystal momentum), we refer to harnessing the cyclotron plasmonic modes for information processing, transmittal, and storage as *plasmontronics*. The mechanism of this plasmon-induced carrier polarization in degenerate semiconductor NCs is an intriguing and challenging problem. We

hypothesize that optical phonons play a particularly important role in this mechanism, because they couple with both excitons and plasmons in semiconductors. Exciton-phonon coupling is governed by specific matrix elements of the coupling operator.[162] On the other hand, free electrons associated with LSPR can also couple with optical phonons in metal oxide NCs,[92] which is the basis of a well-known polaron effect. Importantly for this work, the phonons can transfer an angular momentum allowing for both the generation of the magnetoplasmonic modes and splitting of the semiconductor band states in the external magnetic field.[163]

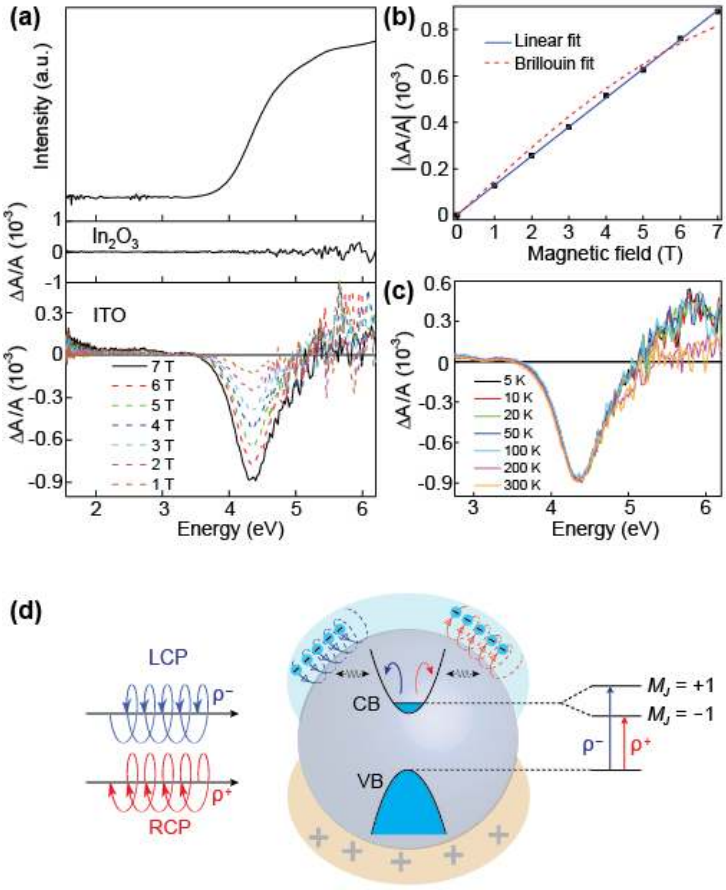

Figure 3.5 (a) Absorption (solid blue line) and MCD (solid black and colored dashed lines) spectra of ITO NCs (containing 10 % Sn^{4+}) collected at 300 K. MCD spectra were recorded at different external magnetic field strengths, as indicated in the graph. 300 K MCD spectrum of In_2O_3 NCs (collected at 7 T) is shown for comparison (solid red line); (b) Magnetic field dependence of MCD intensity at 4.34 eV for ITO NCs in a as function of the magnetic field strength. The linear and Brillouin fits to the

experimental data are shown with blue and dashed red line, respectively; (c) 7 T MCD spectra of NCs in a collected at different temperatures (5-300 K); (d) Schematic representation of the splitting of the conduction band states, induced by angular momentum of the cyclotron magnetoplasmonic modes. Upon excitation with LCP and RCP light in a magnetic field cyclotron magnetoplasmonic modes with helicity ρ- (curved dashed blue line) and ρ+ (curved dashed red line), respectively, are formed. These modes couple with the exciton and transfer angular momentum (blue and red curved arrows) to the conduction band excited states, causing their splitting ($M_J = \pm 1$) and difference in absorption of LCP (vertical blue arrow) and RCP(vertical red arrow) light.

3.4 Effect of Localized Electrons

Figure 3.6a (top panel) shows 5 K MCD spectra of In_2O_3 NCs synthesized in oxygen-rich conditions, for different magnetic fields. Surprisingly, a strong derivative-shaped signal coinciding with the band gap absorption transition is observed, indicating robust excitonic splitting in these NCs. The integrated MCD intensity is plotted with respect to the magnetic field in Figure 3.6 (top panel). The MCD intensity clearly begins to saturate at high magnetic fields, which is characteristic for a paramagnetic behavior. Assuming that this splitting is due to localized unpaired electrons associated with point defects, that could be oxygen vacancies and other internal or surface defects, we fitted the data in Figure 3.6b (top) with the Brillouin function (Eq. 2.4) for the spin state S=1/2 and Lande g-factor g_S =2.002,[164] using the carrier concentration (N) as the only fitting parameter (red line). An excellent fit to the experimental data points suggests that native defects containing localized unpaired electrons can spin-split the NC band states in analogy to transition metal dopants in diluted magnetic semiconductors.[165] The MCD spectra of In_2O_3 NCs synthesized under inert atmosphere show qualitatively similar trend with increasing magnetic field (middle panel in Figure 3.6a), although fitting to the MCD intensities (Figure 3.6b, middle panel) shows deviation from S=1/2 Brillouin function dependence (red line) toward linear behavior (blue line). Upon incorporation of the sufficiently high concentration of Sn^{4+}, the MCD intensity becomes completely linearly dependent on the magnetic field (Figure 3.6a, bottom panel). This reversal of the functional form from saturation to linearity suggests a change in the origin of the excitonic splitting, which is well-correlated with the evolution of LSPR from Figure 3.4a. As discussed above, cyclotron magnetoplasmonic modes, induced by the excitation of plasmonic In_2O_3 NCs with circularly polarized light in an external magnetic field, transfer angular momentum to the excitonic states leading to their Zeeman splitting. Broadening of the excitonic MCD spectrum of ITO NCs is

associated with a range of the number of free electrons in NCs due to variation in doping concentrations as well as the NC size distribution.[166-167]

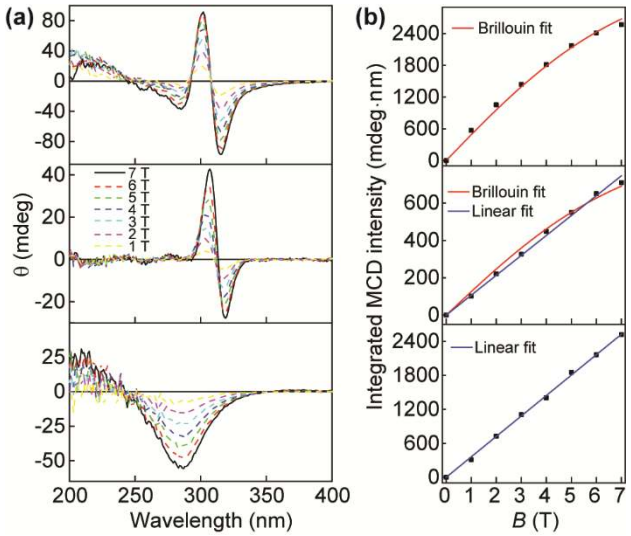

Figure 3.6 (a) MCD spectra of In_2O_3 NCs synthesized in air (top panel), In_2O_3 NCs synthesized in argon atmosphere (middle panel), and 10 % ITO NCs (bottom panel). MCD spectra were recorded at 5 K and different external magnetic field strengths (1-7 T), as indicated in the graph. (b) Magnetic field dependence of integrated MCD intensity for In_2O_3 NCs synthesized in air (top panel), In_2O_3 NCs synthesized in argon (middle panel), and 10 % ITO NCs (bottom panel). The linear and Brillouin fits to the experimental data are shown with blue and red line, respectively.

We also investigated the temperature dependence of the MCD intensity for undoped In_2O_3 and ITO NCs. For In_2O_3 NCs prepared in air, the MCD signal initially drops sharply with temperature (from 5 to 100 K), followed by a more gradual decrease until it completely disappears at room temperature (Figure 3.7a, top panel and Figure 3.7b, black symbols). The MCD intensity is inversely proportional to temperature according to the Curie's law (Figure 3.7b, black line), and indicates the presence of paramagnetic centers in In_2O_3 NCs prepared in oxidizing atmosphere. In spite of the steep decrease in MCD intensity with temperature, a significant signal with negative sign remains at room temperature in argon-synthesized In_2O_3 NCs (Figure 3.7a, middle panel). The reduction of the initial intensity with temperature follows the same dependence as for under oxidizing conditions (light blue symbols and the associated Curie's law fitting in Figure 3.7b). In contrast to undoped In_2O_3 NCs, the MCD spectra of ITO NCs experience much smaller change with temperature. Specifically, the MCD intensity for 5% ITO NCs diminishes by only 4 % from 5 K to 300 K (red symbols in Figure 3.7b), with the decrease

obeying the Curie-type behavior, as described above. For ITO NCs containing higher doping levels (i.e., 10 % or more) MCD spectra remain virtually unchanged up to room temperature (Figure 3.7a bottom panel, and green and blue symbols in Figure 3.7b). MCD intensity decrease with temperature for ITO NCs evidently becomes less pronounced with increasing doping concentration, suggesting decreased contribution of paramagnetism associated with delocalized unpaired electrons. A comparison of the MCD spectra (given as $\Delta A/A$) of undoped In_2O_3 and ITO NCs collected at 300 K are shown in Figure 3.7c. In addition to the blue shift and increased spectral broadening (vide supra), we observed an increase in excitonic MCD intensity with increasing carrier concentration. Together with the results from Figure 3.6, these data and analysis suggest the coexistence of two exciton splitting mechanisms in In_2O_3 NCs; one that dominates in the absence of free electrons and is temperature dependent (related to the presence of localized unpaired electrons), and the other that becomes relevant at higher doping levels and is temperature independent (induced by the cyclotron magnetoplasmonic modes).[31] It should also be noted that this robust temperature-independent excitonic MCD signal cannot be associated with internal asymmetries (e.g., local lattice distortions due to the presence of oxygen vacancy sites). If local symmetry distortions contributed to excitonic Zeeman splitting at room temperature, the excitonic MCD signal would appear in the spectra of air-synthesized NCs (which to some extent also contain localized oxygen vacancies and/or other point defects), and gradually increase in intensity with increasing defect concentration. However, excitonic MCD signal is detected only when LSPR is actually formed in NCs, suggesting the sensitivity of the temperature-independent exciton Zeeman splitting to plasmon oscillations. Furthermore, in argon-synthesized In_2O_3 NCs that contain other dopant impurity traps and lack free electrons,[168-169] there is no evidence of excitonic MCD signal even though the local lattice distortions should be even stronger.

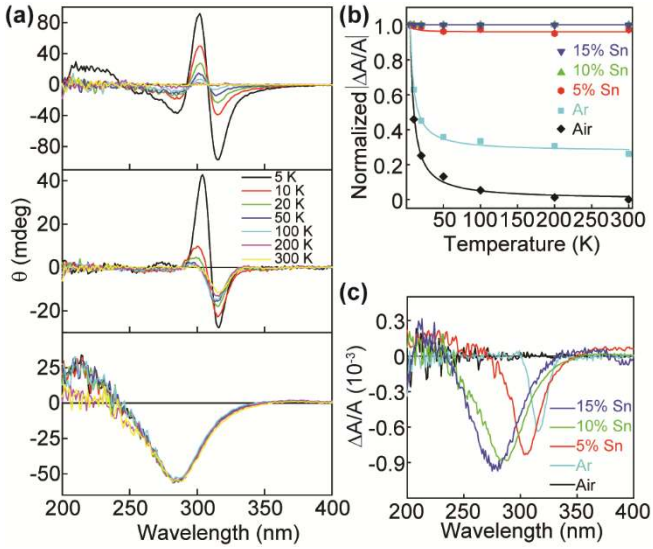

Figure 3.7 (a) 7 T MCD spectra of In_2O_3 NCs synthesized in air (top panel), In_2O_3 NCs synthesized in argon atmosphere (middle panel), and 10 % ITO NCs (bottom panel) collected at different temperatures (5-300 K), as indicated in the graph. (b) Temperature dependence of the normalized integrated MCD intensity for In_2O_3 NCs synthesized in air (black symbols), In_2O_3 NCs synthesized in argon atmosphere (light blue symbols), and ITO NCs having different doping concentration as indicated in the graph. The data are fit to Curie's law (solid lines). (c) MCD spectra (collected at 300 K) of NCs in (b) in the exciton region. The MCD intensity is converted to ΔA/A to enable comparison between different samples.

The results of this work reveal important and unique new properties of plasmonic semiconductor NCs. Unlike diluted magnetic semiconductors, the In_2O_3 and ITO NCs studied in this work contain no magnetic dopants but still exhibit exciton splitting associated with both individual and collective electronic properties. At low concentration of oxygen vacancies, the number of free carriers is too small to generate collective oscillatory behavior,[170] and the NC band splitting is associated with localized spin as an intrinsic electronic property. An increase in the concentration of vacancy defects results in the increased density of free electrons[171] and their resonant cyclotron motion induced by circularly polarized light. In the external magnetic field, the ensuing magnetoplasmonic modes induce conduction band splitting around the Fermi level (vide supra). Given that LSPR has been reported for only a few free electrons in In_2O_3 NCs,[12] the individual electrons that lead to spin-splitting of the band states must be highly localized on native defect sites. Increase in the carrier density by aliovalent doping leads to higher oscillator strength of LSPR and cyclotron plasmon resonance, and consequently to an increase in the contribution of magnetoplasmon-induced band splitting. MCD can therefore serve as a sensitive probe of the carrier delocalization. The observed change in excitonic splitting pattern with increasing

concentration of defects and/or dopants in Figure 3.7b is a signature of the evolution of electron delocalization in this material.

Low-temperature magnetic susceptibility measurements show excellent agreement with the MCD data for In_2O_3 NCs (Figure 3.8a). Importantly, the saturation magnetization for ITO NCs increases with Sn^{4+} doping concentration (Figure 3.8b), suggesting that the density of localized charge carriers also increases with aliovalent doping. Similarly, the saturation magnetization of In_2O_3 NCs synthesized in non-oxidizing atmosphere is higher than that of In_2O_3 NCs synthesized in air (Figure 3.8b). The conclusion that arises from these results is that the density of both localized and delocalized electrons increases with increasing concentration of aliovalent dopants or oxygen vacancies. However, an increase in the overall carrier density leads to enhanced excitonic Zeeman splitting associated with cyclotron magnetoplasmonic modes, while the anomalous spin-induced Zeeman splitting associated with localized charge carriers subsides.

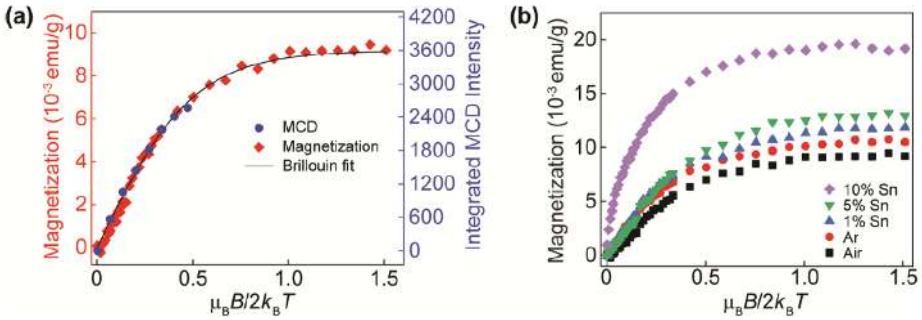

Figure 3.8(a) Comparison between the magnetic susceptibility data and integrated MCD signal intensity for In_2O_3 NCs synthesized in oxidizing conditions as a function of the magnetic field (B). The data were fit to the Brillouin function (Eq. 2.4), and are in excellent agreement. (b) Magnetic susceptibility data for In_2O_3 NCs synthesized in air (black symbols) and argon (red symbols) and ITO NCs having different Sn^{4+} doping concentrations, as indicated in the graph.

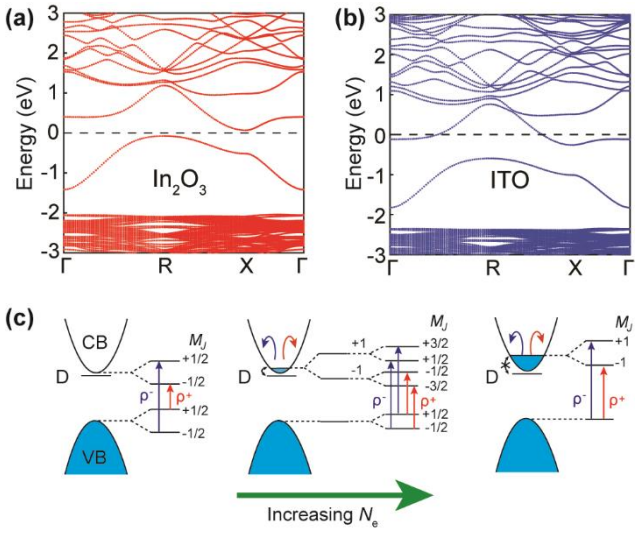

Figure 3.9 (a,b) Calculated band structure diagrams of (a) oxygen-deficient In_2O_3 and (b) 3.125 % Sn^{4+}:In_2O_3 (ITO) NCs. (c) Schematic representation of the band splitting with increasing free electron concentration: splitting induced by localized electron spins in the absence of LSPR (left), splitting induced by the coexistence of localized spins and angular momentum of the magnetoplasmonic modes due to delocalized electrons (middle), and by angular momentum of the cyclotron magnetoplasmonic modes alone at high conduction band occupancy (right) in In_2O_3. The increase of the concentration of free electrons is indicated by the arrow.

To understand this phenomenon, we performed density functional theory (DFT) calculations using generalized gradient approximation (GGA) for In_2O_3 and ITO (See Experimental Section 2.3.12). Comparison of the band structure diagrams for ideal In_2O_3 and ITO lattices demonstrates aliovalent-dopant-induced filling of the conduction band with free electrons (see Appendix C), consistent with the observed Burstein-Moss shift, as well as the previously reported calculations.[158,172] Similar calculations performed by introducing oxygen vacancies (V_O) to mimic the electronic structure of the NCs in this study suggest the formation of new states within the band gap which can act as double donors (Figure 3.9a and b).[173] Unpaired electrons localized in these states (and possibly other sub-band-gap states associated with surface defects) are responsible for the observed paramagnetism with saturation magnetization corresponding to S=1/2. Increasing concentration of oxygen vacancies and/or Sn^{4+} dopants (Figure 3.9b) leads to an increased number of electrons in the conduction band, raising the position of the Fermi level and the energy separation between the NC excited states and the localized defect states. A key feature responsible for indirect exchange interaction between localized defect states and unoccupied conduction band states, and the subsequent spin-induced band splitting of the NC host

lattice, is their mixing. In the simplified description, this mixing can be parametrized by the mixing coefficient (C_{D-E}) according to the perturbation theory:

$$C_{\text{D-E}} = \frac{\left\langle \psi_{\text{D}} \left| \hat{H}_{\text{DE}} \right| \psi_{\text{E}} \right\rangle}{\Delta E_{\text{D-E}}} \qquad \textbf{(Equation 3.1)}$$

where $\left\langle \psi_{\text{D}} \left| \hat{H}_{\text{DE}} \right| \psi_{\text{E}} \right\rangle$ is a wavefunction mixing integral describing the strength of mixing interaction, and ΔE_{D-E} is the energy difference between native or surface defect states and conduction band excited states. In the absence of free electrons, the band splitting is governed only by anomalous Zeeman splitting induced by electron spins in shallow localized defect states (Figure 3.9c, left). For relatively low conduction band occupancy, localized-electron-spin-induced band splitting coexists with magnetoplasmon-induced splitting due to relatively small value of ΔE_{D-E} (Figure 3.9c, middle). The anomalous spin-induced Zeeman splitting can be described similarly to exchange interactions in DMSs,[160] with dominant s-d like interactions between localized donor spins and delocalized electrons.[174] At high concentration of free electrons, large ΔE_{D-E} prevents the exchange interaction between native defect states and conduction band excited states (Figure 3.9c, right). Therefore, with increasing free carrier concentration the probability of anomalous Zeeman splitting of the NC band structure is reduced, while coupling between magnetoplasmonic modes and exciton is enhanced, leading to controlled polarization of charge carriers.

3.5 Conclusion

In this chapter, the field and temperature dependent MCD measurements on degenerately doped In_2O_3 NCs suggest that the cyclotron magnetoplasmonic modes impart significant orbital angular momentum to the nanocrystal excited state, leading to the formation of oppositely polarized electronic states around the Fermi level. The MCD measurements on In_2O_3 NCs synthesized under different atmosphere show that, at low carrier concentration regime, the excitonic splitting can also be induced by the localized unpaired electrons on native defects. The magnetization susceptibility measurements indicate that increase in aliovalent doping concentration also induces the formation of additional lattice defects due to charge compensation, leading to an increase in the number of localized carriers trapped in these sites. This is on contrary to the MCD results of heavily doped In_2O_3 NCs in which the excitonic splitting has negligible contribution from the localized electrons. Combing with DFT calculations, the

observed phenomenon can be explained in the context of perturbation theory. With increasing free carrier concentration, energy difference between native or surface defect states and conduction band excited states enlarges and reduces the probability of anomalous Zeeman splitting of the NC band structure. This work demonstrate the ability to control carrier polarization using both individual and collective electronic properties.

Chapter 4

Effect of Dopant Activation and Plasmon Damping on Carrier Polarization in In_2O_3 Nanocrystals

This chapter presents a study of the synthesis and direct comparison of the plasmonic properties of IMO and IWO NCs. Using a combination of structural and spectroscopic methods, including XRD, TEM, EDX, XPS, as well as XAS, we demonstrated that molybdenum and tungsten donor states in In_2O_3 NCs have different activation energy, allowing for tuning of LSPR energy, intensity, and coherence of NCs without introducing a significant structural difference. Comparison of the excitonic MCD spectra of IMO and IWO NCs having different doping concentrations demonstrates that the excitonic splitting of the NC band structure increases with increasing LSPR intensity and decreasing LSPR damping. This chapter is partly adapted from:

Yin, P.; Tan, Y.; Fang, H.; Hegde, M.; Radovanovic, P.V. "Plasmon-Induced Carrier Polarization in Semiconductor Nanocrystals" *Nat. Nanotechnol.* **2018**, *13*, 463-467. Copyright © 2018, Macmillan Publishers Limited.

Yin, P.; Tan, Y.; Ward, M.J.; Hegde, M.; Radovanovic P. V. "Effect of Dopant Activation and Plasmon Damping on Carrier Polarization in Molybdenum and Tungsten-Doped In_2O_3 Nanocrystals" *J. Phys. Chem. C* **2019**, *123*, 29829-29837. Copyright © 2019, American Chemical Society.

4.1 Structural Characterization of IMO and IWO NCs

The synthesis of colloidal IMO and IWO NCs having different compositions was performed by non-injection method in an inert atmosphere, as described in the Experimental section 2.2.2. An overview TEM image of typical IMO NCs synthesized with Mo/In molar precursor ratio of 0.1 is shown in Figure 4.1a. These NCs have truncated square bipyramidal morphology with an average height (i.e., the longest dimension) of 13.5 ± 2.7 nm (Figure 4.1b). The average doping concentration was determined by EDX elemental analysis to be 9.2%. The summary of the characterization results for IMO NCs synthesized with different Mo^{6+} starting concentration in the reaction mixture is given in Table 4.1. For all NCs there is a tendency of a slight increase in the NC size and the extent of dopant incorporation with increasing dopant precursor concentration. Similar NCs were obtained in the presence of the same amount of tungsten ([W]/[In]=0.1), as the dopant precursor. The size of IWO NCs is somewhat smaller than that of IMO NCs, with an average bipyramid height of 9.1 ± 1.7 nm (Figure 4.1 c and d). The

amount of tungsten incorporated in NCs also appears to be reduced at higher dopant precursor concentration, indicating a lower rate of dopant incorporation. Importantly, Mo(VI) and W(VI) have nearly the same ionic radii in six-coordinate environment (0.59 Å and 0.60 Å for Mo(VI) and W(VI), respectively), suggesting that the difference in dopant size is not the cause for lower incorporation rate of tungsten. Instead, the actual doping concentration is likely associated with the stability of the two metal ions in the corresponding precursors relative to substitutional doping sites in NCs. Both high-resolution TEM images (Figure 4.1a,b insets) and powder XRD patterns (Figure 4.1e) demonstrate that the samples are highly crystalline and have cubic crystal structure characteristic for bixbyite-type In_2O_3. The XRD peak broadening generally decreases with increasing doping concentration for both IMO and IWO NCs (See Appendix D), consistent with an increase in the average NC size. Figure 4.1f compares the Raman spectra of IMO and IWO NCs in Figure 4.1e. The peaks for both NC samples show significant broadening and decrease in intensity relative to those for In_2O_3 NCs, suggesting an increased long range lattice disorder associated with the difference in size between In^{3+} (0.80 Å) and dopant ions, as well as possible presence of accompanying native defects (e.g., oxygen vacancies).

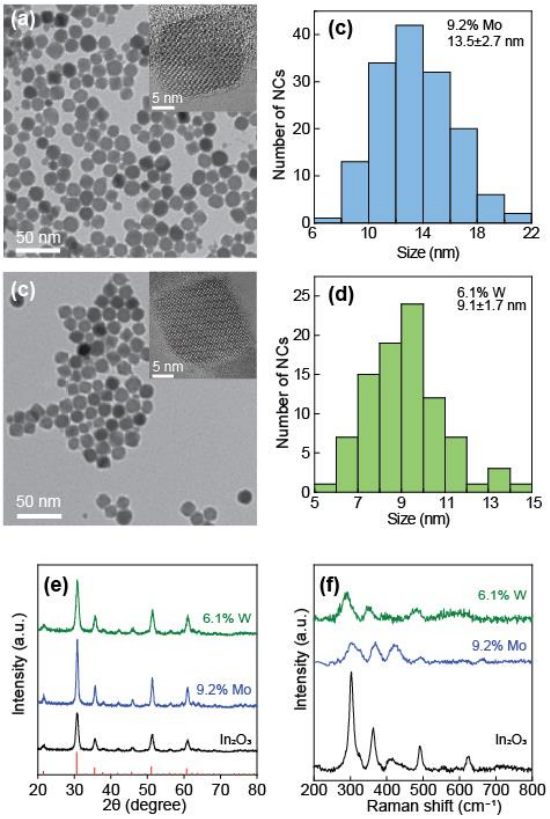

Figure 4.1 (a) TEM image of 9.2% IMO NCs. (b) Size distribution histogram for 9.2% IMO NCs determined from TEM images. (c) TEM image of 6.1% IWO NCs. (d) Size distribution histogram for

6.1% IWO NCs determined from TEM images. (e) XRD patterns of In_2O_3 NCs (black line), 9.2% IMO NCs (blue line), and 6.1% IWO NCs (green line). Red sticks represent XRD pattern of bulk In_2O_3. (f) Raman spectra of NCs in (e), as labeled in the graph. Insets in panel (a) and (b) are typical lattice-resolved TEM images of individual 9.2% IMO and 6.1% IWO NC, respectively.

Table 4.1 Actual doping concentrations and average sizes of IMO and IWO NCs.

Nominal [Mo]/[In] (%)	Actual [Mo]/[In] (%)	Average size (nm)	Nominal [W]/[In] (%)	Actual [W]/[In] (%)	Average size (nm)
1	0.3	10.3	1	0.4	7.5
3	1.4	11.1	3	1.2	9.2
5	4.2	12.7	5	1.5	11.8
10	9.2	13.5	10	6.1	9.1

4.2 Electronic Structure of Mo and W dopants

The electronic structure of Mo and W dopant ions were investigated using XPS and X-ray absorption spectroscopies. Molybdenum 3d XPS spectrum of 4.2% IMO NCs is shown in Figure 4.2a. The observed splitting pattern suggests the presence of molybdenum ions in at least two oxidation states, which were identified by fitting the Shirley-background-corrected spectrum with Voigt functions. An excellent fit was achieved for two spin−orbit doublets corresponding to Mo $3d_{5/2}$ and Mo $3d_{3/2}$ states (Figure 4.2a, red line). The higher energy doublet with Mo $3d_{5/2}$ component at 232.4 eV and Mo $3d_{3/2}$ component at 235.6 eV (blue shaded area) is assigned to Mo^{6+}, based on the values characteristic for MoO_3 (232.5 eV and 235.6 eV for Mo $3d_{5/2}$ and Mo $3d_{3/2}$, respectively).[175-176] The components of the lower-lying doublet at 231.0 eV and 234.1 eV (orange shaded area) are close to the binding energies of Mo $3d_{5/2}$ (231.2 eV) and Mo $3d_{3/2}$ (234.3 eV), respectively, reported for Mo^{5+}.[175-176] On the basis of the integrated intensities of Mo $3d_{5/2}$ peaks we estimate that that ca. 30% of Mo dopant ions is in 5+ and 70% in 6+ oxidation state. This is in contrast with IMO thin films prepared by aerosol-assisted chemical

vapor deposition, in which the main oxidation state of Mo is suggested to be 4+.[177] XPS spectra of IMO NCs having different doping concentrations confirm the presence of Mo^{5+} (Figure 4.2b). One of the reasons for the coexistence of Mo^{5+} with Mo^{6+} is the coordinating solvent (oleylamine). Oleylamine acts as a reducing agent,[178-179] allowing for a reduction of a significant fraction of Mo^{6+} to Mo^{5+} which is then incorporated into the NC host lattice.

The electronic structure of Mo dopants was further investigated by X-ray absorption spectroscopy. Figure 4.2c shows the XANES spectra of IMO NCs having different doping concentrations together with commercial MoO_2 and MoO_3 powders as standards. The most notable differences observed from the XANES spectra are changes in the intensity of the pre-edge feature and a slight shift in energy of the primary absorption edge. The pre-edge intensity arises from dipole-forbidden Mo 1s→4d transitions, which become allowed via Mo 4d-5p orbital mixing. This mixing increases with the reduction of Mo site symmetry.[180] A unit cell of bixbyite-type In_2O_3 consists of 16 formula units, with In^{3+} distributed between two non-equivalent six-coordinated sites. Eight In^{3+} ions reside in a trigonally-compressed octahedral coordination of 6 equidistant oxygen ions (denoted as In(1) or b sites). The remaining 24 cations are located in the centers of the tetragonally-distorted polyhedra having three different In-O bond distances [denoted as In(2) of d sites]. It has been suggested that molybdenum ions preferentially occupy b sites in In_2O_3,[181] similarly to Sn^{4+} dopants in indium tin oxide (ITO) NCs.[182] The pre-edge band is observed in all IMO NC samples, but increases in intensity with increasing doping concentration. These observations indicate a change in dopant speciation with increasing doping concentration. As the doping level increases fewer In(1) sites are available, forcing additional Mo ions to begin to occupy other available sites, including In(2).

In contrast to molybdenum, tungsten dopants in In_2O_3 NCs prepared under described conditions predominantly reside in 6+ oxidation states, based on XPS spectra (Figure 4.2d and e). No definitive evidence of the presence of lower oxidation states was found. Although W K-edge lies in an energy range that is inaccessible at the 20BM beamline at APS (> 69.5 keV), L_3-edge has been shown to be a useful alternative for assessing the tungsten oxidation state and geometry.[183] Tungsten L_3-edge XANES spectra of IWO NCs are very similar to that of WO_3 and show negligible shift for different doping concentrations (Figure 4.2f), confirming insignificant changes in the dopant oxidation state. A small but of noticeable shift to lower energy has been observed for more reduced tungsten (Figure 4.3).[183] A slight increase in the amplitude of the white line with increasing doping concentration is mostly related to an increase in local distortion of WO_6 octahedra, as expected.[184]

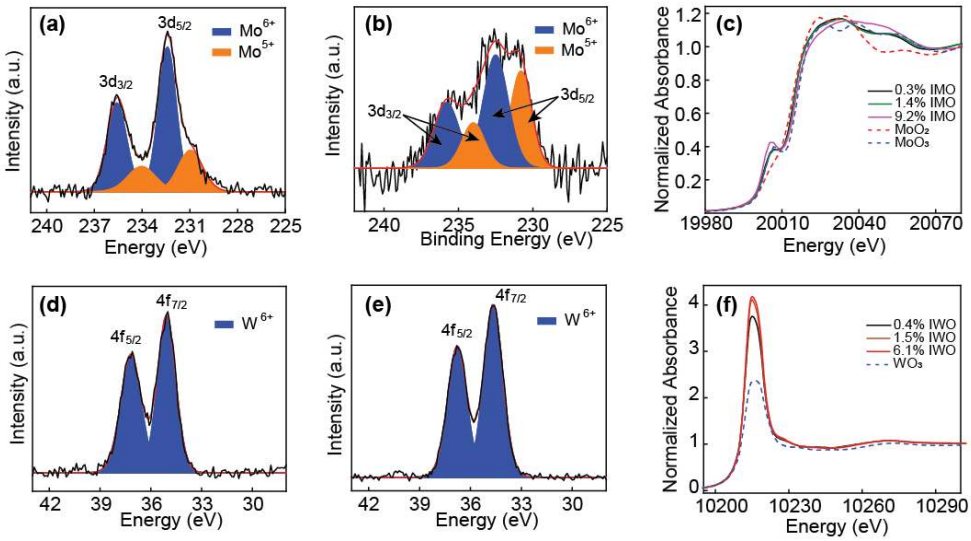

Figure 4.2 (a,b) Molybdenum 3d XPS spectrum of 4.2% (a) and 9.2% (b) IMO NCs (black lines). Spin-orbit components obtained by Voigt fitting are shown with blue and orange shaded areas for Mo^{6+} and Mo^{5+}, respectively, as indicated in the graph. The overall fits to the experimental spectrum are shown with red lines. (c) Molybdenum K-edge XANES spectra of IMO NCs having different doping concentrations and molybdenum oxide standards (MoO_2 and MoO_3), as indicated in the graph. (d,e) Tungsten 4f XPS spectrum of 1.5% (d) and 6.1% (e) IWO NCs (black lines). Spin-orbit components corresponding to W^{6+} obtained by Voigt fitting are shown with blue shaded area. The overall fits to the experimental spectrum are shown with red lines. (d) Tungsten L-edge XANES spectra of IWO NCs having different doping concentrations and WO_3, as indicated in the graph.

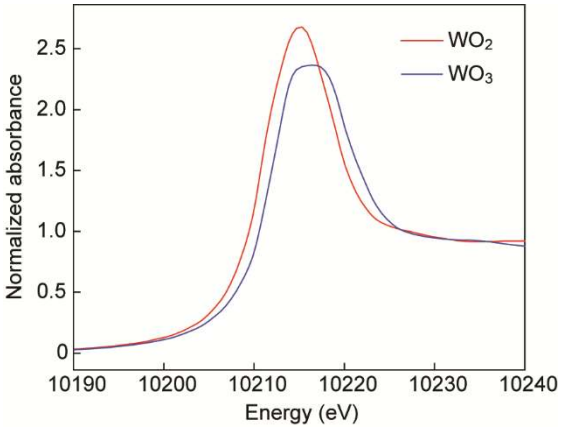

Figure 4.3 W L_3-edge XANES spectra of WO_3 and WO_2, demonstrating a shift of the main absorption band (white line) to lower energy with decreasing oxidation state.

Absorption spectra of IMO and IWO NCs are shown in Figure 4.4. The spectra of IMO NCs in the MIR region display a characteristic LSPR band, which increases in intensity and shifts to higher energy with increasing doping concentration (Figure 4.4a). This trend is associated with an increase in the free electron density, and is accompanied by a blue shift of the NC band edge absorption (Figure 4.4b) due to an increased occupancy of the conduction band states (Burstein-Moss shift).[15] Qualitatively similar behavior is observed for IWO NCs at low doping levels (Figure 4.4c and d). However, in contrast to the spectra of IMO NCs, the maximum LSPR energy and intensity are attained at starting tungsten precursor concentration of 5%. Further increase in the doping concentration leads to a decrease in the absorption intensity and the red shift of LSPR band (Figure 4.4c). The same reversal is observed for IWO band edge absorption (Figure 4.4d). The effective free electron concentration responsible for plasmonic properties of semiconductor NCs is a result of two opposing effects by aliovalent dopants - free electron generation and electron scattering effects.[15] The maximum carrier density is evidently achieved for significantly lower doping concentration in IWO than in IMO NCs, suggesting a higher tungsten dopant activation.

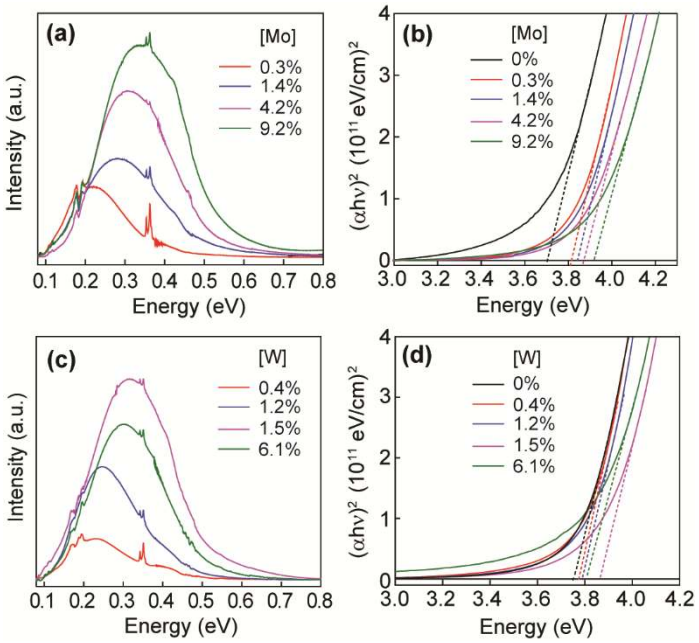

Figure 4.4 (a) LSPR absorption spectra of IMO NCs having different doping concentrations, as indicated in the graph. (b) Tauc plots for IMO NCs from panel (a) used to determine optical band gaps. (c) LSPR absorption spectra of IWO NCs having different doping concentrations, as indicated in the graph. (d) Tauc plots for IWO NCs from panel (c) used to determine optical band gaps.

To investigate the origin of this difference we performed comparative DFT calculations for Mo and W-doped In_2O_3 by replacing one In atom sitting in the b site of a 80 atom In_2O_3 unit cell with Mo or W, which corresponds to the doping concentration of 3.125%. The optimized lattice parameters were found to be very similar, consistent with the negligible difference in ionic radii of Mo and W (Table 4.2). The calculated density of states for IMO and IWO are plotted in Figure 4.5a and b, respectively. The total density of states diagrams for IMO and IWO (top panels) show nearly identical features suggesting a similar electronic structure of the two systems. The conduction band is comprised of In 5s and 5p states, as previously reported,[12,158] and both dopants have localized d states at the Fermi level, suggesting their relatively weak overlap with the oxygen orbitals. Furthermore, conduction band width and dispersion are similar for both IMO and IWO (Figure 4.6), implying a similar effect of both Mo and W dopants on the host lattice electronic structure and carrier mobility. Given the analogous effect of molybdenum and tungsten dopants on the electronic structure of In_2O_3, the difference in dopant activation can be at least partly associated with a different ratio of dopant ions in 5+ and 6+ oxidation states. As discussed above, a significant fraction of molybdenum dopants is in 5+ oxidation states, while tungsten exists predominantly, if not exclusively, as W^{6+}. Taken together, the theoretical and spectroscopic results suggest that Mo^{5+} is electrically inactive, requiring larger doping concentration to achieve the same free carrier density.

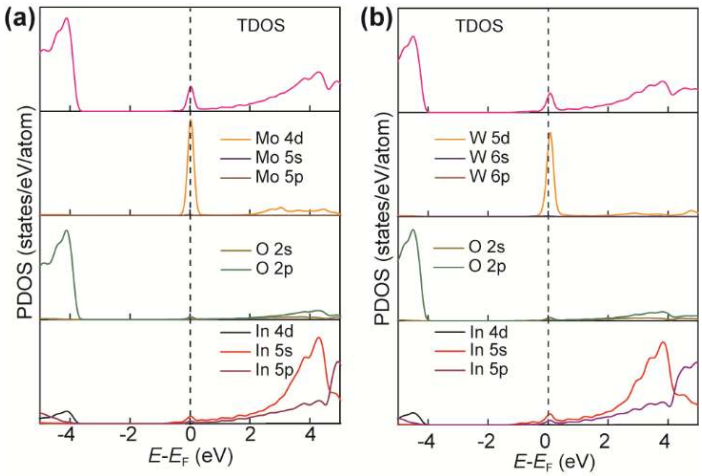

Figure 4.5 Projected density of states diagrams for (a) 3.125% IMO, and (b) 3.125% IWO calculated by DFT. Fermi levels are indicated with the dashed lines. Contributions from specific orbitals of Mo, In, and O atoms to the total density of states (TDOS) are labeled in the graphs.

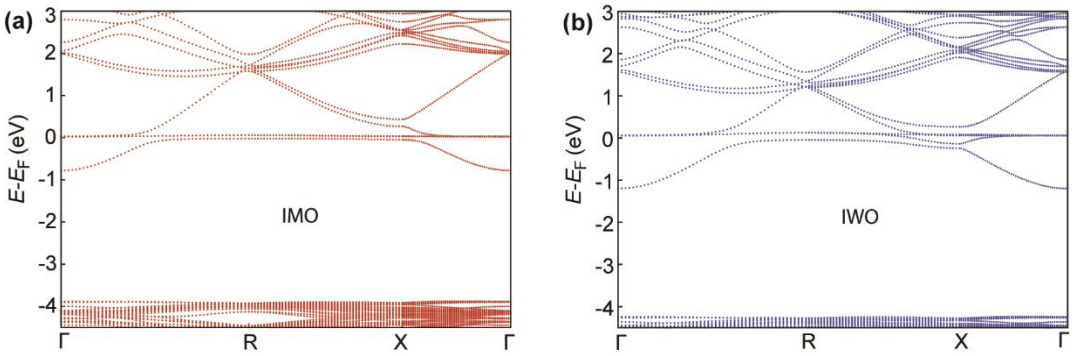

Figure 4.6 Band structure diagram of (a) 3.125% Mo-doped In_2O_3 (IMO) and (b) 3.125% W-doped In_2O_3 (IWO) calculated by DFT as described in Experimental section 2.3.12.2.

Table 4.2 Structural parameters from DFT calculations

System	Lattice Parameter (Å)
In_2O_3	10.116
Mo:In_2O_3 (IMO)	10.114
W:In_2O_3 (IWO)	10.128

4.3 Carrier Polarization in IMO and IWO NCs

Figure 4.7a (bottom panel) shows MCD spectra of 9.2% IMO NCs in the UV-visible region, collected at 7 T. The negative MCD bands with a maximum intensity at ca. 4.05 eV coincide with the band gap absorption (top panel), confirming their excitonic origin. The MCD intensity exhibits a linear increase with magnetic field strength (inset in Figure 4.7a). This linearity uniquely reflects the magnetic field dependence of the MCD intensity of cyclotron magnetoplasmonic modes, as described before (see also MCD data for another representative IMO NC sample in Figure 4.8).[63,81] The fact that the excitonic signal with identical magnetic field dependence was observed without direct excitation of LSPR, attests to non-resonant plasmon-exciton coupling as a means of excitonic splitting and carrier polarization. This coupling enables not only the formation of magnetoplasmonic modes upon band gap excitation with circularly polarized light in a magnetic field, but also the transfer of the angular momentum from the magnetoplasmons to the conduction band states.[31] The temperature dependence of the excitonic

MCD band for IMO NCs having different doping concentrations is shown in Figure 4.7b. All samples show a decrease in MCD intensity on warming up the samples from 5 to 100 K, that obeys the Curie-Weiss law. However, the majority of the excitonic MCD intensity is temperature independent and remains unchanged up to 100 K. The extent of the temperature-induced depletion of MCD intensity decreases with increasing doping concentration; for 0.3% IMO NCs the MCD signal drops by ca. 35% from 5 to 100 K, while for 9.2% IMO NCs the reduction in MCD intensity in the same temperature range is only 12%. This difference in MCD temperature dependence is consistent with the increased C-term MCD contribution for lower doping concentrations,[31,151] due to the interactions involving paramagnetic species in the ground state. Comparable data were obtained for IWO NCs (Figure 4.9).

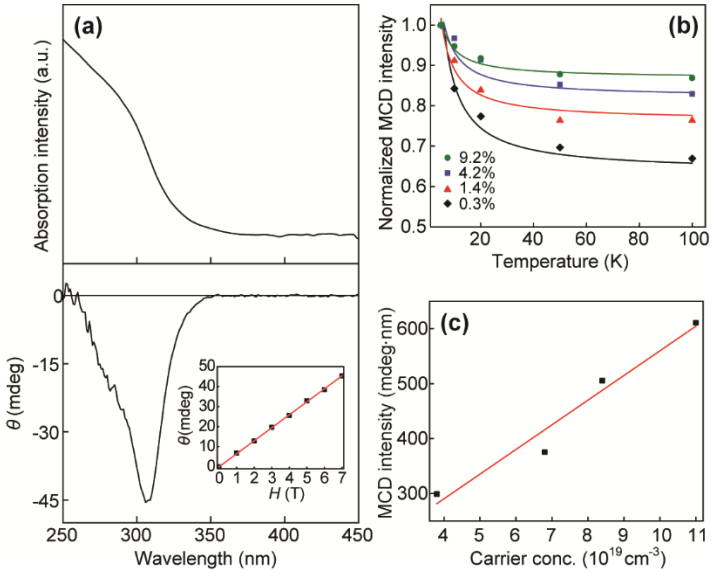

Figure 4.7 (a) Optical absorption (top panel) and 7 T MCD (bottom panel) spectra of 9.2% IMO NCs collected at 5 K. Inset: magnetic field dependence of the excitonic MCD intensity maximum. (b) Normalized 7 T excitonic MCD intensity as a function of temperature for IMO NCs having different doping concentrations, as indicated in the graph. (c) Dependence of the integrated 7 T excitonic MCD signal intensity at 300 K on carrier concentration for IMO NCs.

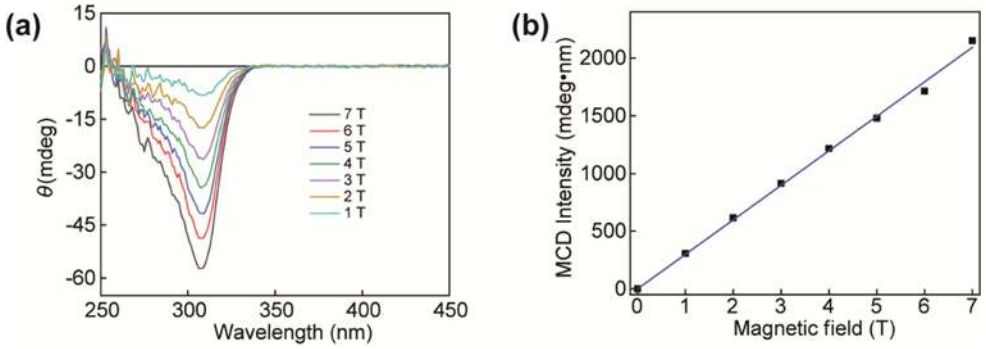

Figure 4.8 (a) 5 K MCD spectra of 4.2% IMO NCs collected at different magnetic fields from 1 to 7 T, as indicated in the graph. (b) Magnetic field dependence of the integrated excitonic MCD intensity for the spectra in (a).

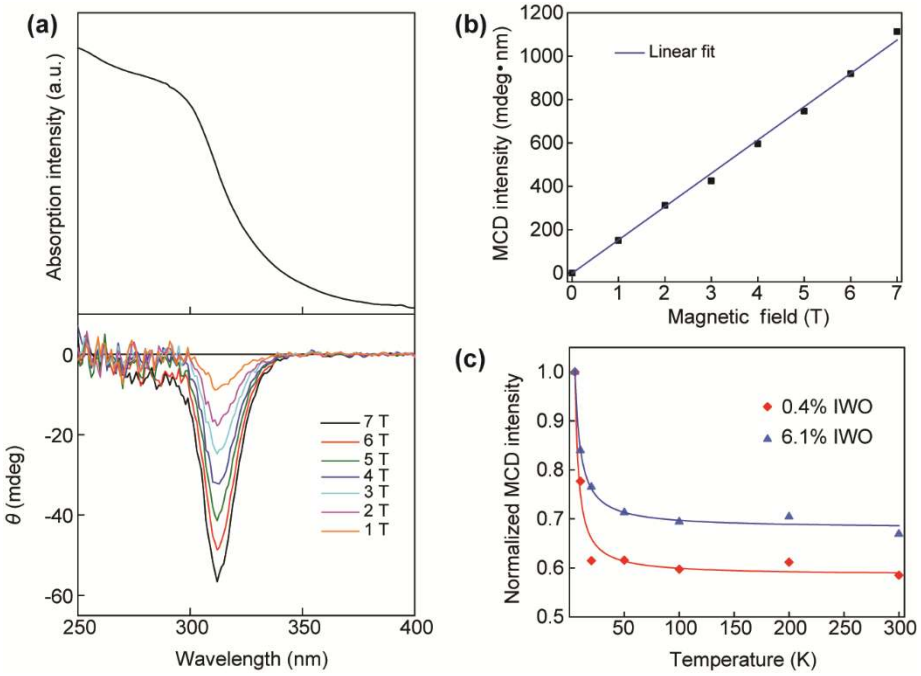

Figure 4.9 (a) Optical absorption (top panel) and variable-field MCD (bottom panel) spectra of 6.1% IWO NCs in the band gap region collected at 5 K. Magnetic fields corresponding the spectra in the bottom panel are indicated in the graph. (b) Magnetic field dependence of the integrated excitonic MCD intensity in (a). (c) Normalized 7 T excitonic MCD intensity as a function of temperature for IWO NCs having different doping concentrations, as indicated in the graph.

As we have shown in the Chapter 3, the spin-splitting (anomalous Zeeman splitting) of excitonic states in plasmonic metal oxide NCs can arise not only from coupling of the conduction band states with unpaired d electrons on aliovalent transition metal dopant ions, but also with localized electrons on oxygen vacancy sites.[26] In this study, dopant-induced spin-splitting would require the molybdenum or tungsten to exist in NCs in a reduced form relative to their precursors (Mo^{6+} or W^{6+}). The appreciable amount of reduced dopants is found only in IMO NCs. Given a similar Curie-type temperature dependence of the excitonic MCD intensity for IMO and IWO NCs, it can be concluded that the NC excited state splitting is predominantly due to exchange interactions of the conduction band states with electrons trapped on native defect sites (e.g., oxygen vacancies) rather than with unpaired d electrons on dopant ions. The A-term excitonic MCD intensity for IMO NCs, expressed as a relative difference in absorption of LCP and RCP light at 300 K,[31,151] is plotted as a function of carrier density in Figure 4.7c. The magnitude of magnetoplasmon-induced excitonic splitting increases linearly with carrier concentration, suggesting that free carriers are directly correlated with the degree of excitonic spitting.

To independently test the effects of specific plasmonic properties on the excitonic Zeeman splitting, we compared the results of room-temperature MCD measurements for IMO and IWO NCs. Although molybdenum and tungsten have similar chemical behavior and ionic radii, they exhibit different average oxidation states and activation energies in In_2O_3 NCs, allowing for concurrent modulation of the plasmonic properties (LSPR frequency and intensity, and the carrier mobility and scattering). Figure 4.10a shows LSPR absorption spectra of IMO and IWO NCs having low doping concentrations, normalized to the band gap absorbance. The band energy and broadening for these two samples are similar, but the maximum intensity is nearly two-fold higher for IMO NCs. The difference in excitonic MCD intensities (Figure 4.10b) follows the difference in LSPR intensity, consistent with the results in Figure 4.7c. Similar effect of the LSPR intensity on excitonic MCD was consistently observed for all available IMO and IWO NC samples (Figure 4.11). On the other hand, Figure 4.10c compares the LSPR spectra of IMO and IWO NCs having high doping concentrations. These samples also have nearly identical LSPR peak energy and intensity, but show noticeable difference in spectral broadening. The LSPR absorption band width is determined by electron damping (Γ), which typically arises from impurity-related electron scattering (ionized impurity scattering).[73] Based on the modified Drude-Lorentz model, Γ is related to the frequency-dependent dielectric function of the material ($\varepsilon(\omega)$) via following expression:[67]

$$\varepsilon(\omega) = \varepsilon_{\infty}\left(1 - \frac{\omega_p^2}{\omega^2 + i\omega\Gamma}\right) \qquad \textbf{(Equation 4.1)}$$

where ε_{∞} is the high-frequency dielectric constant ($\approx$4 based on ITO).[185] The frequency-dependent dielectric function in Eq. 4.1 is related to the LSPR absorbance through Mie approximation, as shown in Appendix E.[185] Fitting the spectra in Figure 4.10c (see Figure E.1) allows us to extract the values of Γ as a free parameter. The damping of plasmon oscillations is ca. 15% larger, while the excitonic MCD intensity is ca. 10 % lower for IMO relative to IWO NCs (Figure 4.10d), implying that the plasmon dephasing and carrier polarization are also well correlated.

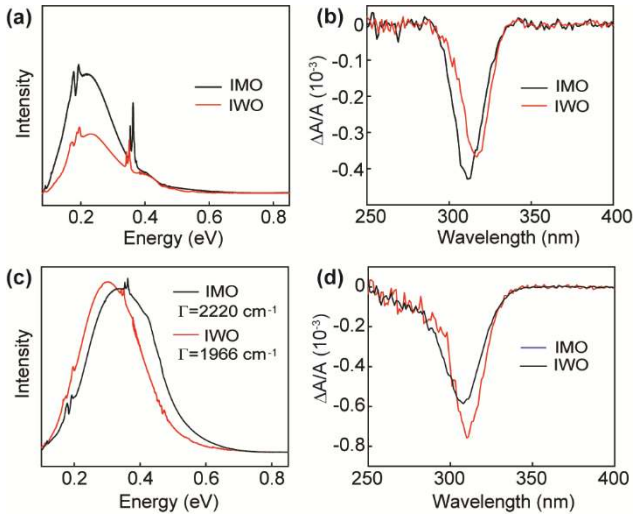

Figure 4.10. (a,b) LSPR absorption spectra (a) and 7 T excitonic MCD spectra (b) of IMO and IWO NCs having different LSPR band intensity but nearly identical broadening (carrier damping). (c,d) LSPR absorption spectra (c) and 7 T excitonic MCD spectra (d) of IMO and IWO NCs having similar LSPR band maximum energy and intensity but different broadening. The damping constant (Γ) was determined from the LSPR spectral broadening by fitting the spectra to the Drude-Lorentz model. The LSPR spectra were normalized to the band gap absorption intensity. All MCD spectra were collected at 300 K.

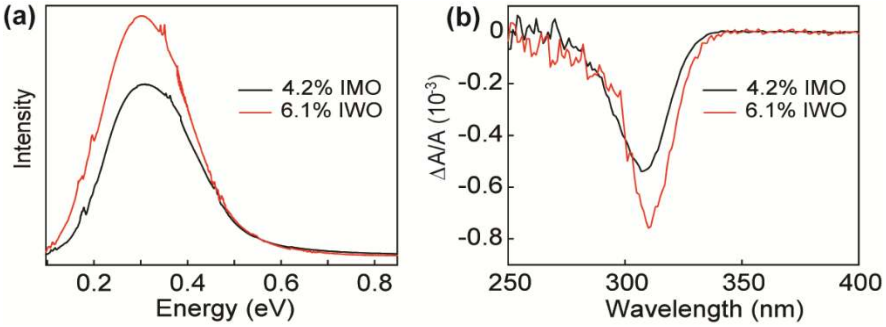

Figure 4.11 (a) LSPR absorption spectra and (b) 7 T excitonic MCD spectra of 4.2% IMO and 6.1% IWO NCs having different LSPR band intensity but nearly identical broadening (carrier damping). The LSPR spectra were normalized to the band gap absorption intensity. MCD spectra were collected at 300 K. The MCD intensities are well-correlated with LSPR intensities, similarly to the data from Figure 4.10, reflecting the role of plasmon oscillator strength in magnetoplasmon-induced excitonic splitting.

Taken together, the results of Figures 4.7 and 4.10 demonstrate that the magnitude of the observed magnetoplasmon-induced excitonic splitting in In_2O_3 NCs is determined by a complex interplay between the NC electronic and structural parameters. The sensitivity of the excitonic MCD signal to LSPR intensity indicates that the increased carrier density promotes the angular momentum transfer to the conduction band excited states, owing to the increased magnetoplasmonic oscillator strength. By contrast, increased dephasing of LSPR oscillations due to ionized impurity scattering reduces the ability of the magnetoplasmonic modes to transfer angular momentum to the conduction band electrons.

4.4 Conclusions

In this chapter, I report the synthesis of colloidal plasmonic IMO and IWO NCs. Despite the similar chemical properties of Mo and W, the XPS and XANES results indicate a significant fraction of molybdenum dopants is in 5+ oxidation states, while tungsten exists predominantly as W^{6+}. Both IMO and IWO NCs exhibit tunable LSPR absorption in the MIR range. However, for IWO NCs, the highest LSPR energy (maximum carrier density) is achieved for significantly lower doping concentration compared to that of IMO NCs, suggesting a higher tungsten dopant activation. DFT calculations show similar effect of molybdenum and tungsten dopants on the electronic structure of In_2O_3, thus the difference in dopant activation can be at least partly associated with a different ratio of dopant ions in 5+ and 6+ oxidation states. The different activation energy of molybdenum and tungsten allowing us to obtain structurally similar NCs with different LSPR properties. Comparative MCD measurements

suggest the excitonic splitting of the NC host lattice is correlated with the LSPR intensity, suggesting the key role of the oscillator strength of the magnetoplasmonic modes in imparting angular momentum to the conduction band states. Furthermore, LSPR damping lead to the dephasing of the magnetoplasmonic oscillations and reduce the magnitude of the angular momentum transfer to the excitonic states.

Chapter 5

Faceting Controlled Carrier Polarization in TiO_2 Nanocrystals

In previous Chapters, we demonstrated the magnetic-field-mediated plasmon-induced carrier polarization in aliovalently doped In_2O_3 NCs. LSPR also can be generated in vacancy-doped TiO_2 NCs. Additionally, the formation of oxygen vacancies in TiO_2 is accompanied by the formation of Ti^{3+}, which is responsible for the generation of new energy states with the band gap.[186] Thus it is intriguing to study the plasmon-induced carrier polarization in oxygen-deficient TiO_2 NCs. In this chapter, using MCD spectroscopy, we demonstrated unique excitonic splitting patterns in plasmonic TiO_2 NCs enabled by simultaneous control of their faceting and the degree of electron delocalization. This work has been published as: Yin, P.; Hegde, M.; Garnet, N.S.; Tan, Y.; Radovanovic, P.V. "Faceting-Controlled Zeeman Splitting in Plasmonic TiO_2 Nanocrystals" *Nano Lett.* **2019**, *19*, 6695-6702. Copyright © 2019, American Chemical Society.

5.1 Structural and Optical Properties of TiO_2 NCs

The TiO_2 NC morphology and faceting, as well as the defect formation in the NCs were controlled by the selection of titanium(IV) halide precursor [TiF_4 (F), $TiCl_4$ (Cl), or their mixture (M)] and the coordinating ligand [oleylamine (OLAM) or 1-octadecanol (ODOL)]. We adopted the designation previously used for these types of samples, which specifies the precursor and coordinating ligand using the above abbreviations (F-OLAM, M-OLAM, and Cl-ODOL).[27] All NC samples exhibit tetragonal anatase crystal structure, as evident from the XRD patterns shown in Figure 5.1a. The shifting and broadening of (004) and (200) peaks, and the ratio of (105) to (211) peaks have been associated with the degree of truncation of tetragonal bipyramidal anatase NCs perpendicular to <001> direction.[27] In case of TiF_4 precursor, F^- ions can selectively bind to facets of the nucleated anatase TiO_2 NCs and act as a morphology-controlling agent,[187] allowing F-OLAM TiO_2 NCs to adopt strongly truncated bipyramidal morphology with a dominant fraction of {001} facets. Such a high degree of truncation effectively gives rise to the formation of nanoplatelets, as shown in the inset of Figure 5.1a (top panel). On the other hand, M-OLAM and Cl-ODOL samples have reduced {001} faceting and dominant {101} faceting (insets in Figure 5.1a). The morphology of the NCs from these samples was confirmed by TEM imaging (Figure 1b and Figures F.1-F.3 in Appendix F). Additional discussion about the NC formation mechanism and morphology is also given in Appendix F. As expected based on the XRD

peak broadening, which is particularly evident for $2\theta \approx 38°$ and 55°, the average size of NCs of Cl-ODOL sample is larger than that of M-OLAM sample by a factor of 2 (Figure 5.2).

The absorption spectra of TiO_2 NC samples in the UV-visible and IR range, normalized to the band gap absorbance (i.e., NC volume), are shown in Figure 5.1c and d, respectively. In contrast to Cl-ODOL NCs, a strong broad band in the MIR range is observed for F-OLAM and M-OLAM NCs (Figure 5.1c). This band is characteristic for LSPR and gives F-OLAM and M-OLAM colloidal suspensions characteristic blue-green color (inset in Figure 5.1c). The intensity of LSPR is nearly two times higher for M-OLAM than for F-OLAM sample, indicating a higher density of free conduction band electrons in the former. This increase in electron density is accompanied only by a relatively small blue shift of the LSPR band maximum.[19] A low sensitivity of plasma frequency (ω_p) on carrier density could arise from nonparabolicity of the conduction band in anatase TiO_2,[188] similarly to degenerately-doped InN.[38] It is generally accepted that extra electrons in TiO_2 arise from oxygen vacancies, which are responsible for high conductivity of TiO_2 bulk samples,[189] thin films,[190] or nanostructures.[191] While the redox titration method[38,192-193] for counting free electrons in these NCs proved to be challenging, based on Drude model fitting of the LSPR spectra we estimate that the free electron densities of F-OLAM and M-OLAM NCs are on the order of 10^{20} cm^{-3}.[67] The concentration of localized electrons is expected to be only a fraction of this value (see below). The increase in the LSPR intensity is accompanied by a blue shift in the band edge absorption (Figure 5.1d) due to increased filling of the conduction band states (Burstein-Moss shift). It is relevant to note that the band edge absorption of M-OLAM lies at a higher energy relative to that of F-OLAM sample, in spite of F-OLAM NCs being significantly smaller in one dimension (truncated bipyramid height), confirming that the blue shift is not due to quantum confinement. Given the absence of LSPR in Cl-ODOL NCs, this sample will serve as a control experiment in the magneto-optical measurements (see below).

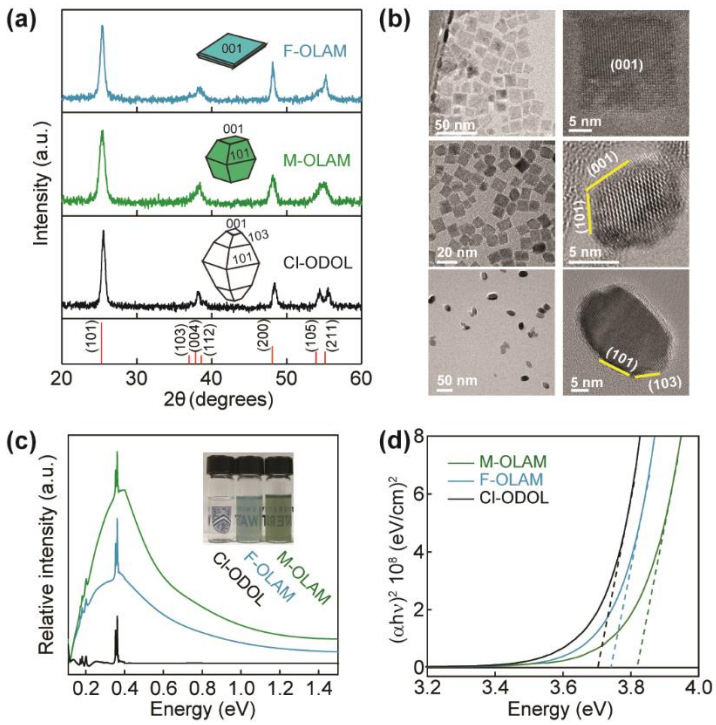

Figure 5.1 (a) XRD patterns of F-OLAM, M-OLAM and Cl-ODOL TiO_2 NCs described in the text. The corresponding NC shapes are shown as insets. (b) Overview (left) and lattice-resolved (right) TEM images of F-OLAM (top panels), M-OLAM (middle panels) and Cl-ODOL (bottom panels) NC samples in (a). The relevant lattice planes are indicated in the lattice-resolved images in the right hand side panels. (c,d) Optical absorption spectra of the same NC samples in the MIR range (c) and UV-visible range (d), showing LSPR and band gap absorption, respectively. The absorption spectra are normalized to the NC volume. The photographs of the colloidal suspensions of NCs are shown in the inset in (c).

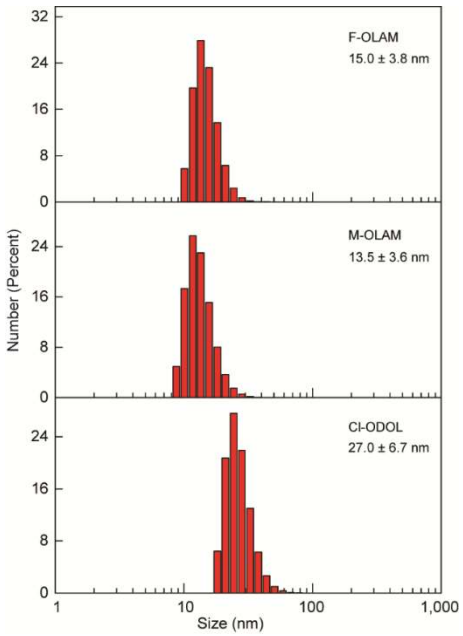

Figure 5.2 Size distribution histograms for F-OLAM (top), M-OLAM (middle) and Cl-ODOL (bottom) TiO_2 NCs determined from dynamic light scattering measurements on toluene suspensions. The average nanocrystal sizes and standard deviations are shown in the corresponding graphs.

5.2 Electronic Structure of TiO_2 NCs

To investigate the local electronic structure of TiO_2 NCs we performed comparative X-ray photoelectron spectroscopy (XPS) and X-ray absorption near-edge spectroscopy (XANES) investigations. Figure 5.3a shows Ti 2p XPS spectra of M-OLAM (bottom), F-OLAM (middle), and Cl-ODOL (top) TiO_2 NCs. The two peaks centered at 458.5 eV and 464.3 eV in the spectra of Cl-ODOL and F-OLAM samples are readily assigned to the $2p_{3/2}$ and $2p_{1/2}$ doublet transition, respectively, characteristic for Ti^{4+}. However, in contrast to the spectra of F-OLAM and Cl-ODOL, M-OLAM spectrum clearly shows asymmetric structure and broadening at the low energy side of both spectral bands. Multiple peak fitting reveals the presence of additional peaks at 457.7 eV and 462.6 eV, which are characteristic for Ti^{3+} $2p_{3/2}$ and $2p_{1/2}$, respectively. We further investigated the coordination number and local symmetry of Ti sites using XANES (Figure 5.4). The pre-edge features of XANES spectra are particularly sensitive to the Ti coordination environment, because the local symmetry affects the degree of p-d orbital mixing.[194] The pre-edge spectrum of Cl-ODOL (Figure 5.3b, top panel) shows four characteristic peaks with relative intensities similar to the spectra reported for anatase TiO_2.[195-196]

On the basis of an empirical correlation between the A2/A3 peak ratio and the particle size, the increased A2 peak intensity has been attributed to the increased contribution from five-coordinate Ti centers mostly residing in the surface vicinity.[195] Similar trend is observed in Figure 5.3b. The A2/A3 peak ratio for F-OLAM (middle panel) and M-OLAM (bottom panel) increases noticeably compared to that for Cl-ODOL sample, consistent with their smaller sizes and larger surface-to-volume ratios. Importantly, although F-OLAM NCs have larger surface area to volume ratio than M-OLAM NCs, owing to their platelet-like morphology, the A2/A3 peak ratios are similar. This observation suggests that the additional Ti sites with a lower coordination number reside in the interior of M-OLAM NCs, which can be associated with internal oxygen vacancies.

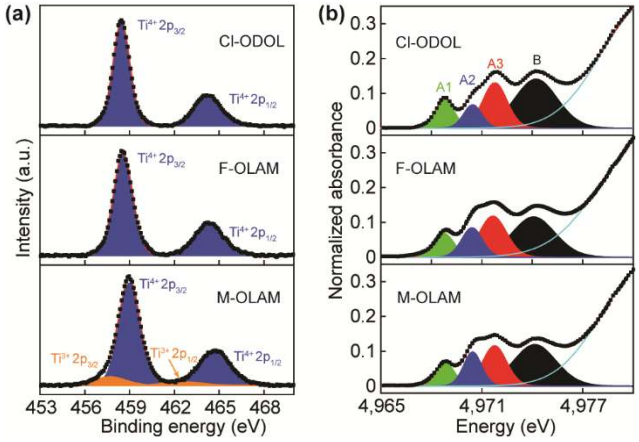

Figure 5.3 (a) Ti 2p XPS spectra of Cl-ODOL (top panel), F-OLAM (middle panel) and M-OLAM (bottom panel) TiO_2 NC samples. Best fits to the experimental data (black squares) are shown with red lines and the shaded areas represent deconvoluted Ti^{4+} (blue) and Ti^{3+} (orange) 2p doublets. (b) Pre-edge XANES spectra of Cl-ODOL (top panel), F-OLAM (middle panel) and M-OLAM (bottom panel) samples. Best fits to the experimental data (black squares) are shown with red lines and the shaded areas represent deconvoluted characteristic peaks indicated in the top panel. Light blue line is the fit to the leading edge of the shoulder feature in the XANES spectrum located at ca. 4980 eV.

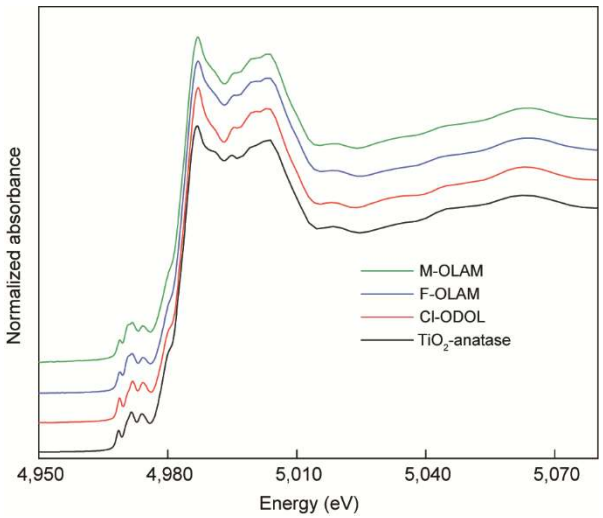

Figure 5.4 Overview XANES spectra of F-OLAM, M-OLAM, and Cl-ODOL nanocrystal samples, as indicated in the graph. Spectrum of commercial anatase TiO_2 powder (black trace) is shown for comparison.

To examine the electronic states of plasmonic TiO_2 NCs we performed density functional theory (DFT) calculations of ideal and vacancy-containing TiO_2. The calculated electronic structure of the ideal and vacancy-doped TiO_2 supercell is shown in Figure 5.5. Figure 5.5a plots the projected density of states of ideal anatase TiO_2. The valence and conduction bands have mostly oxygen 2p and titanium 3d character, respectively, as expected. The calculated band gap energy is 2.33 eV, which is in reasonable agreement with the experimental value of the optical band gap (3.2 eV), given the well-documented propensity of DFT methods to underestimate the band gap energy of semiconductors. Introduction of a single oxygen vacancy in the supercell leads to the formation of sub-band-gap states ca. 0.22 eV below the conduction band (Figure 5.5b and c). These states have Ti 3d character, and are associated with the formation of Ti^{3+}. These results are consistent with the premise that oxygen vacancies can act as trap states which foster the reduction of the Ti^{4+} host lattice cations and the subsequent Ti^{3+} self-doping. The introduction of oxygen vacancy also shifts the Fermi level to higher energies, associated with the formation of electron donor states. The formation of shallow Ti^{3+} states near the conduction band edge can explain that the individual Ti^{3+} centers and complexes involving exchange-coupled Ti^{3+} contribute to the observed band splitting in addition to magnetoplasmonic modes. (See below)

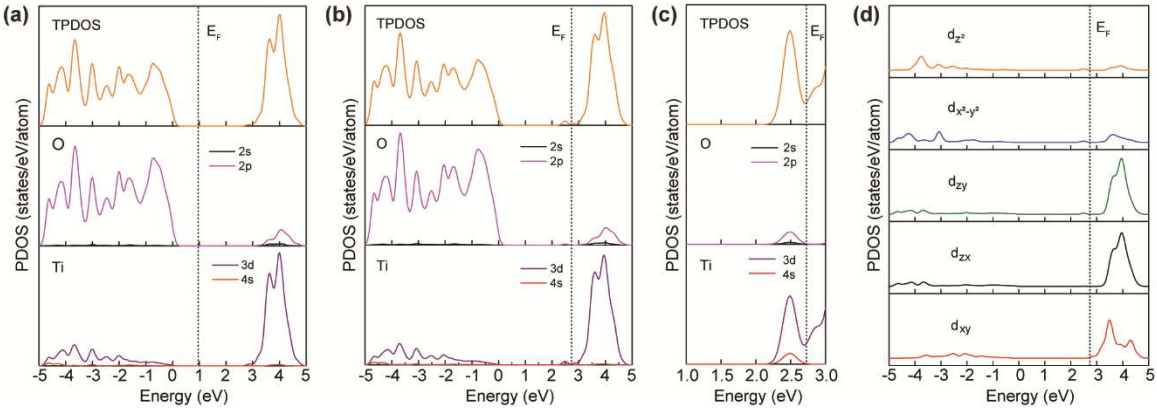

Figure 5.5 Density functional theory calculations for TiO_2 NCs. (a-c) Projected density of states for Ti (bottom panels) and O (middle panels), and total projected density of states (top panels) for (a) ideal TiO_2 supercell, (b) vacancy-containing TiO_2 supercell, and (c) vacancy-containing TiO_2 supercell near the conduction band edge. The Fermi levels are shown with dashed lines. The valence and conduction bands have mostly oxygen 2p and titanium 3d character, respectively. (d) Titanium d-orbital contribution to the Ti projected density of states, indicating that the lower part of the conduction band is dominated by d_{xy} orbitals.

5.3 Magneto-optical properties of TiO_2 NCs

Figure 5.6 (lower panel) compares the MCD spectra of F-OLAM and M-OLAM samples in the UV-visible range. The dominant feature in both spectra is the positive band that coincides with the corresponding band edge absorption (upper panel of Figure 5.6). In contrast to F-OLAM and M-OLAM, no MCD signal is observed for non-plasmonic Cl-ODOL TiO_2 NCs (dashed trace in Figure 5.6) which is consistent with the previous magneto-optical studies on anatase TiO_2 thin films.[197-198] This comparison confirms that the LSPR is necessary for inducing band splitting in TiO_2 NCs using magnetic field and circularly polarized light. Unlike LSPR MCD signal, which originates from cyclotron motion of free electrons,[81-82] the excitonic MCD intensity involves Zeeman splitting of the excited electronic states. LSPR can be indirectly excited by circularly polarized light via coupling with the exciton, while the resulting magnetoplasmonic modes induced by an external magnetic field impart angular momentum to the excited states around the Fermi level.[31] The mechanism by which cyclotron magnetoplasmonic modes are generated and coupled with exciton to produce aforementioned Zeeman splitting is a subject of an ongoing investigation. However, an important component of this mechanism could be lattice phonons, because they satisfy key requirements to mediate the process; phonons can

couple with both excitons[162] and plasmons[92] in semiconductors, and simultaneously transfer angular momentum,[163] allowing for the formation of the magnetoplasmonic modes and splitting of the conduction band states in a magnetic field. Importantly, the sign of the excitonic MCD band is opposite from that observed for plasmonic In_2O_3 NCs (Figure 5.7),[26,31] indicating reversed splitting pattern of the excited states. The ramification of these results is that plasmon-induced carrier polarization can be controlled by the electronic structure of the NC host lattice. While these considerations require further investigations and are beyond the scope of this work, one of the notable differences between In_2O_3 and TiO_2 is that the nature of the conduction band states.[12,199] Unlike the conduction band of In_2O_3, which has In s-orbital character, the conduction band of anatase TiO_2 consists predominantly of symmetry-sensitive Ti d-states (Figure 5.5).[199] Specifically, the lower part of the TiO_2 conduction band is dominated by d_{xy} orbitals (Figure 5.5d). This hypothesis was confirmed for $WO_{2.72}$ NCs (Appendix G), which also have the conduction band states made up of W 5d orbitals.[200]

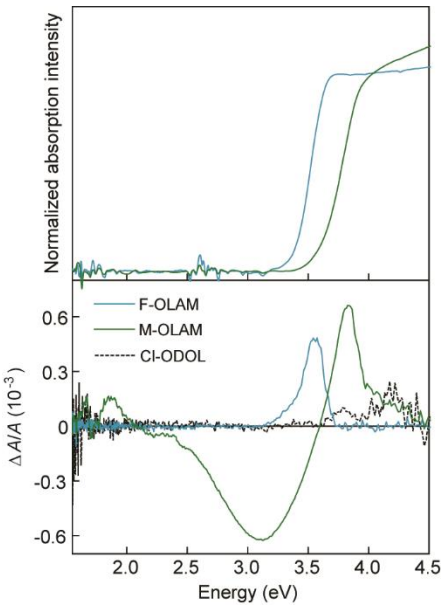

Figure 5.6 Optical absorption (top panel) and MCD (bottom panel) spectra of F-OLAM (blue trace) and M-OLAM (green trace) NCs in the UV-visible region. MCD spectrum of Cl-ODOL (black dashed trace) is shown for comparison.

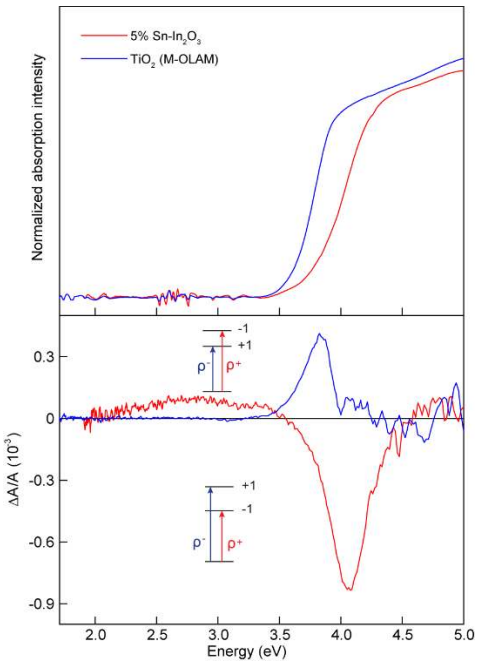

Figure 5.7 Comparison between 300 K MCD spectra of M-OLAM TiO_2 and 5 % Sn-doped In_2O_3 (ITO) NCs. The opposite sign of MCD bands attests to the role of the nanocrystal electronic structure on the magnetoplasmon-induced excitonic splitting (illustrated in the insets).

Although the excitonic splitting is common for both M-OLAM and F-OLAM TiO_2 NCs, there are some notable differences between the MCD spectra of these two samples. The spectrum of M-OLAM has a set of low-intensity spectral features around 1.8 eV (see also Figure 5.8), and a broad structureless band having a negative sign and a maximum intensity at ca. 3.1 eV (400 nm). We assign the low-energy spectral features from 1.6 to 2.1 eV to symmetry-split $^2T_2 \rightarrow {}^2E$ transition, characteristic for six-coordinate Ti^{3+}, based on their energy and intensity.[201] The energy range of the band centered at 3.1 eV appears to be too high for intra-ionic (d-d) ligand-field transitions. Instead, in d^1 complexes, such as Ti(III) and V(IV), such strong broad bands lying above ~ 2.5 eV are generally assigned to interionic (charge transfer) transitions (see below).[202-203] Another difference between M-OLAM and F-OLAM MCD spectra, which is particularly important for this work, is related to high-temperature excitonic MCD intensity (Figure 5.9). The signal intensity at 300 K is stronger for M-OLAM sample, and concurs with the trend of LSPR intensity in Figure 5.1c. This result is consistent with the conclusion that MCD spectra of the excitonic transitions gain intensity through coupling with the magnetoplasmonic modes.[26]

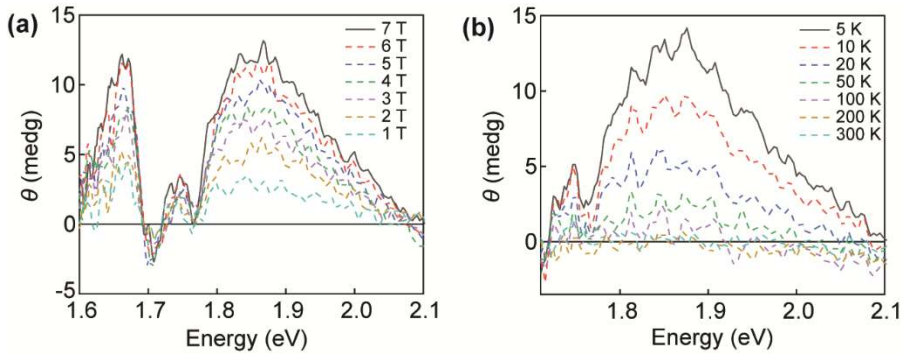

Figure 5.8 Ligand-field MCD spectra of M-OLAM TiO_2 NCs in the low-energy region, assigned to symmetry-split $^2T_2 \rightarrow 2E$ transitions characteristic for six-coordinate Ti^{3+}. (a) Variable-magnetic-field MCD spectra showing saturation behaviour of MCD intensity with increasing magnetic field strength. (b) Variable-temperature MCD spectra showing decreased intensity with increasing temperature. Both magnetic field and temperature dependencies are consistent with paramagnetic behavior.

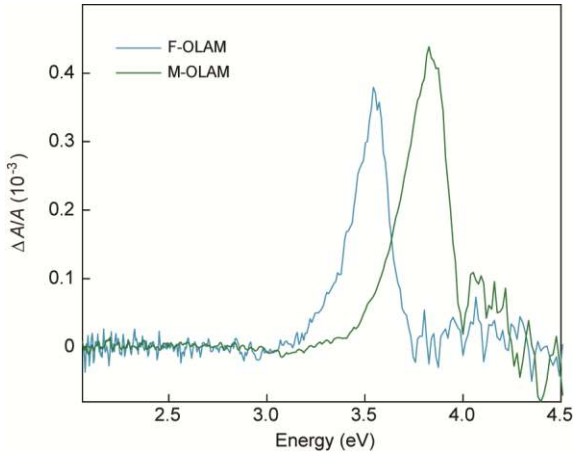

Figure 5.9 300 K MCD spectra of F-OLAM (blue trace) and M-OLAM (green trace) NCs in the band gap region. The MCD intensities are shown normalized to band edge absorbance (ΔA/A), and thus are directly comparable.

The MCD spectra of F-OLAM TiO_2 NCs collected at 5 K and different magnetic fields from 1 to 7 T are shown in Fig 5.10a. The integrated excitonic MCD intensity follows ideal linear dependence on the magnetic field (Figure 5.10b), reflecting the magneto-optical behavior of LSPR. The intensity of this MCD signal decreases with temperature from 5-300 K by ca. 20 % (Figure 5.10c). The excitonic MCD intensity decay with temperature can be fit to Curie-Weiss law (Eq. 2.5). The agreement of the

fit with the experimental data, as shown in Figure 5.10d, suggests that the decrease in the signal intensity with temperature is associated with paramagnetic Ti^{3+} centers formed by reducing a small fraction of Ti^{4+} host lattice cations.[204] Importantly, these results suggest that excitonic splitting in self-doped TiO_2 NCs can be attained without the need for an external magnetic impurity.[205] The component of the excitonic MCD signal that remains constant at high temperatures represents the contribution from the magnetoplasmon-induced carrier polarization, which is independent of temperature.

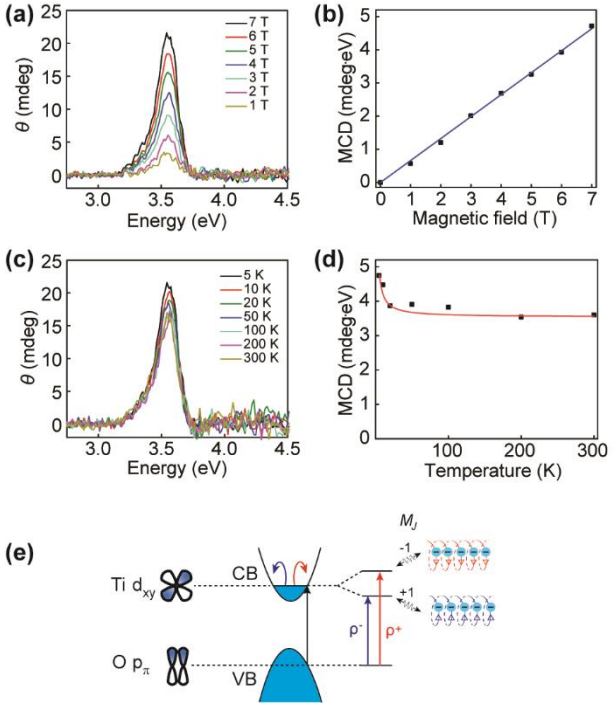

Figure 5.10 (a) 5 K MCD spectra of F-OLAM TiO_2 NCs in the band gap region collected for different magnetic field strengths (1-7 T). (b) Magnetic field dependence of integrated MCD intensities determined from the spectra in (a). (c) 7 T MCD spectra of F-OLAM TiO_2 NCs in the band gap region collected for different temperatures (5-300 K). (d) Temperature dependence of the integrated MCD intensities determined from the spectra in (c). (e) Schematic representation of the excited state splitting in TiO_2 NCs induced by angular momentum of the cyclotron magnetoplasmonic modes (dashed red and blue lines). The splitting causes the difference in absorption of LCP (vertical blue arrow) and RCP (vertical red arrow) light with selection rule $\Delta M_J = \pm 1$.

The field and temperature dependences are more complex for M-OLAM samples (Figure 5.11). The MCD spectra of this sample for different magnetic fields are shown in Figure 5.11a. The intensities of

symmetry-split ligand-field transitions at ~ 1.8 eV saturate with increasing magnetic field strength (Figure 5.8a), although they are too weak to accurately integrate. Even though the negative band at ca. 3.1 eV and the excitonic transition overlap to some degree, their deconvolution through peak fitting (see Experimental Section 2.3.9.3) allows for extraction of the integrated intensities (Figure 5.12). The field dependencies of these integrated intensities are compared in Figure 5.11b. Surprisingly, the Brillouin function (Eq. 2.4) fits best to the intensities of the negative band (red diamonds in Figure 5.11b) for the net spin state S=1 (rather than S=1/2 which would correspond to isolated non-interacting Ti^{3+} sites) and the Landé g-factor of 1.97 characteristic for six-coordinate Ti^{3+}.[206-207] This analysis further suggests that this band is not due to a ligand-field (d-d) transition, but rather charge transfer between a neighboring oxygen ion (as a ligand) and Ti^{3+} ion (as a metal) involved in a dinuclear complex consisting of two ferromagnetically-coupled Ti^{3+} centers. From the solid-state band structure perspective, ligand can also be viewed as a part of the valence band given its O 2p character (Figure 5.5). This conclusion is consistent with the formation of a triplet ground state (S=1) involving exchange coupling of two Ti^{3+} ions, enabled by a bridging oxygen vacancy (Figure 5.11e).[208] It has been proposed that two extra electrons trapped by initially ionized oxygen vacancy site ($V_O^{\bullet\bullet}$) are localized on two individual nearest-neighbor cations, forming a pair of Ti^{3+} ions which are exchange-coupled to give the net spin state of 1.[209] Even higher net spin states have been reported in some reduced anatase TiO_2 NCs, with four ferromagnetically coupled Ti^{3+} ions having an effective spin state S=2.[210] Based on the comparison with the absorption spectra of six-coordinate Ti^{3+} complexes and the observed magnetic field dependence, we assign the negative MCD band in Figure 5.11a to Ti^{3+}-O ligand-to-metal change transfer transition involving exchange-coupled Ti^{3+} (Figure 5.11e).

We were particularly interested in the magnetic field and temperature dependences of the excitonic MCD spectrum of M-OLAM relative to F-OLAM sample. Although the MCD dependence on the magnetic field for the excitonic transition of M-OLAM (Figure 5.11b, blue triangles) differs from that for the charge transfer band (Figure 5.11b, red diamonds), it also significantly deviates from linearity expected for magnetoplasmon-induced band splitting. The difference between the temperature dependences of these two transitions is even more pronounced (Figs. 5.11c and d). The charge transfer band decreases more strongly with temperature, and becomes undetectable at 300 K. On the other hand, excitonic band retains ca. 60 % of its 5 K intensity at room temperature. The decrease in both signals follows the Curie-Weiss law (Eq. 2.5), consistent with spin-induced Zeeman splitting (solid lines in

Figure 5.11d). These results suggest that excitonic splitting consists of two contributions, similarly to F-OLAM samples — magnetoplasmon-induced splitting which is temperature independent, and anomalous Zeeman splitting which decreases with temperature. However, the best fit for the field dependence of the excitonic MCD intensity is obtained for a combination of the linear fit and the Brillouin function for S=1 (solid blue line in Figure 5.11b and Figure 5.13). These results demonstrate not only that the oxygen vacancies serve a dual purpose (to mediate the formation of high-spin state complexes involving Ti^{3+} and to generate LSPR), but that the newly formed high-spin complexes can act as highly-selective spin polarizers in TiO_2 NCs. To our knowledge, this is the first demonstration of a complex consisting of exchange-coupled impurity sites serving as an artificial quasi-molecular dopant that selectively induces splitting of the semiconductor band states. This result opens the door for using redox chemistry involving native defects to engineer and control quantum states.

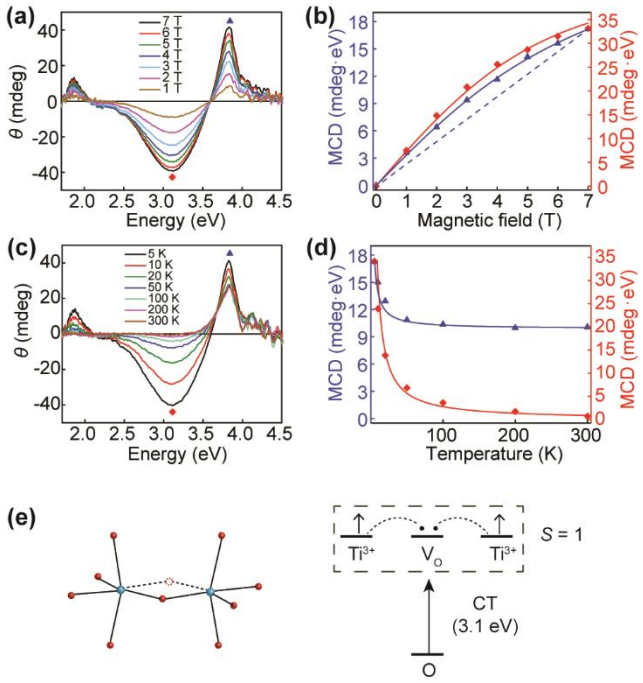

Figure 5.11 (a) 5 K MCD spectra of M-OLAM TiO_2 NCs collected for different magnetic field strengths (1-7 T). (b) Magnetic field dependence of the integrated MCD intensities determined from the spectra in (a) for different transitions, as indicated with the corresponding symbols. Red line is the best fit of the integrated intensity of the negative band centered at ca. 3.1 eV with the Brillouin function (equation 2) for S=1. Blue line is the best fit of the integrated excitonic intensity with a combination of the linear dependence and Brillouin function for S=1. Dashed blue line designates ideal linear

dependence characteristic for magnetoplasmon-induced excited state splitting. (c) 7 T MCD spectra of M-OLAM TiO_2 NCs collected for different temperatures (5-300 K). (d) Temperature dependence of the integrated MCD intensities determined from the spectra in (c) for different transitions, as indicated with the corresponding symbols. The lines are best fits of the Curie-Weiss law (equation 2.5) to the corresponding experimental data points. (e) Schematic representation of a complex involving two neighboring Ti ions (left) and their reduction and coupling induced by oxygen vacancy (right). Titanium sites are shown with light blue spheres, oxygen sites with red spheres, and oxygen vacancy with open dotted circle. The two neighbouring titanium ions reduced by the oxygen vacancy are exchange-coupled giving the net spin state S=1. Charge transfer transition involving exchange-coupled Ti^{3+} are indicated with the arrow.

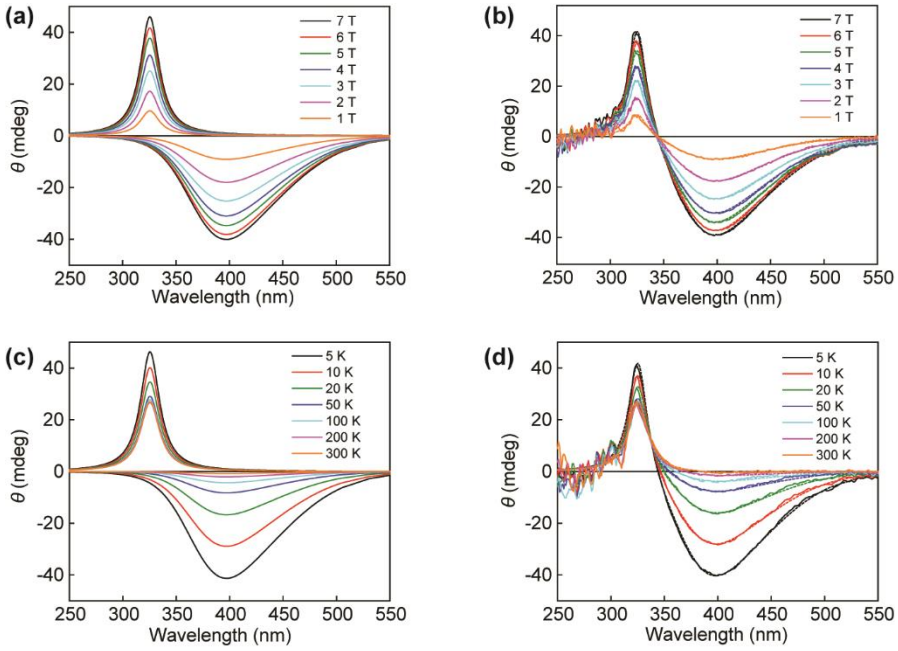

Figure 5.12 (a) Deconvoluted bands for charge transfer transition (negative band) and excitonic transition (positive band) for different magnetic field strengths. (b) Best overall fits (dashed lines) to the experimental spectra (solid lines) for different magnetic field strengths. (c) Deconvoluted bands for charge transfer transition and excitonic transition for different temperatures. (d) Best overall fits (dashed lines) to the experimental spectra (solid lines) for different temperatures. The overall fits are in excellent agreement with the experimental spectra in both (b) and (d).

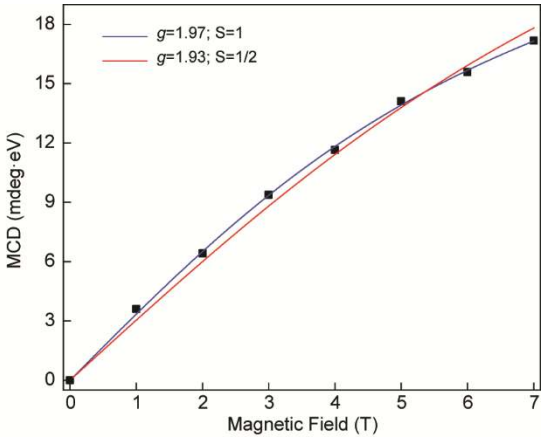

Figure 5.13 Magnetic field dependence of the integrated excitonic MCD intensity for M-OLAM TiO_2 nanocrystal sample (black squares). Solid lines are best fits involving a combination of linear dependence (representing the magnetoplasmon-induced splitting) and Brillouin function (blue line corresponds to g=1.97 and S=1, and red line to g=1.93 and S=1/2). The best agreement is obtained for high net spin state (S=1).

5.4 Magnetic Properties of TiO_2 NCs

The origin of Ti^{3+} formation and the correlation between oxygen vacancies and Ti^{3+} in different TiO_2 NC samples were further explored by EPR spectroscopy (Figure 5.14a). In the case of F-OLAM sample, a relatively strong signal at g≈1.93 and a weaker narrower signal at g≈2.00 were observed. The signal at g=2.00 can be associated with oxygen radical species (e.g., O^- or O_2^-) on TiO_2 surfaces,[211] while that at g≈1.93 to paramagnetic Ti^{3+} ions located on or near the surface of the NCs.[186,211] These EPR features are also observed for M-OLAM sample, although they appear less pronounced owing to the reduced fraction of {001} facets relative to F-OLAM NCs. In addition, the EPR spectrum of M-OLAM sample shows a strong broad signal at g≈1.97. This signal, which has been attributed to the presence of internally-incorporated Ti^{3+}, is frequently associated with the formation of bulk oxygen vacancies (see also Figure 5.5 and the associated discussion),[207] and its broadening is indicative of Ti^{3+} interactions. Internal vacancy-enabled self-doping of TiO_2 NCs with Ti^{3+} results in the formation of Ti^{3+} exchange-coupled pairs which generate high net spin state and contribute to the NC band splitting. To gain further insight into the mechanism of band splitting in TiO_2 NCs, we compared the magneto-optical results with those of the magnetization measurements. The saturation magnetization for M-OLAM sample is ca. 60 times larger than that for F-OLAM, suggesting a higher concentration of

paramagnetic centers (Figure 5.14b). The saturation magnetization for F-OLAM NCs is best fit with S=1/2 Brillouin function, assuming Landé g-factor characteristic for surface-bound Ti^{3+} (g=1.93). A small deviation from the ideal spin-only saturation behavior is likely related to site symmetry-induced spin-orbit coupling (Figure 5.14b, inset). The best fit to the magnetization data for M-OLAM sample, on the other hand, is achieved for S=1 spin state which corresponds to Ti^{3+} exchange-coupled pairs, as discussed above (see also Figure 5.15). From these and the results in Figure 5.1c, it is evident that both free electron concentration (responsible for LSPR intensity) and localized Ti^{3+} centers (responsible for saturation magnetization) increase in parallel, enabled by the formation of the oxygen vacancy defects. The main difference between Ti^{3+}-induced band splitting in F-OLAM and M-OLAM samples is related to the NC dimensionality. The concentration of internal oxygen vacancies and the resulting Ti^{3+}-V_O-Ti^{3+} complexes, which are dominant in M-OLAM NC sample, are negligible in F-OLAM nanoplatelets because of the small fraction of bulk. The Ti^{3+}-related band splitting in F-OLAM can, therefore, be associated only with non-coupled Ti^{3+} in the vicinity of the NC surfaces.

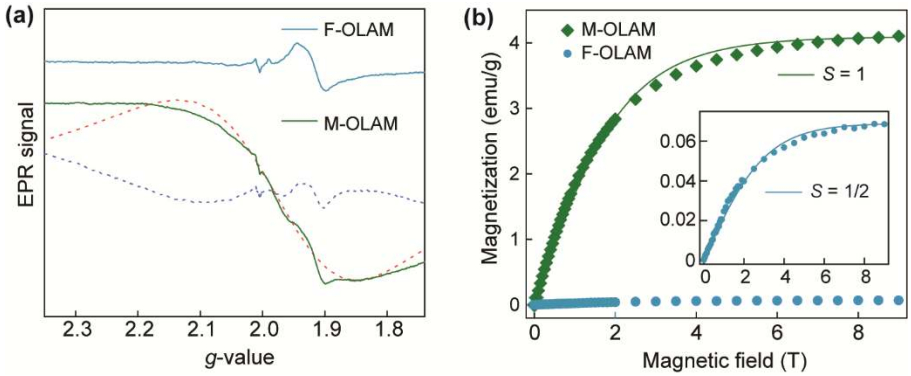

Figure 5.14 (a) EPR spectra of F-OLAM (blue trace) and M-OLAM (green trace) nanocrystal samples. Red dashed line represents the Lorentzian fit to the broad signal arising from strongly interacting internal Ti^{3+}, and dashed dark blue line is a spectrum of M-OLAM sample upon subtraction of the Lorentzian fitting curve. (b) Magnetization as a function of applied magnetic field for F-OLAM and M-OLAM nanocrystal samples. Best fits of the Brillouin function (Eq. 2.4 in the Experimental Section) to the experimental data are shown by corresponding lines. Based on the MCD and EPR results the fitting was performed using S=1/2 and g=1.93 for F-OLAM, and S=1 and g=1.97 for M-OLAM NCs. Inset shows zoomed-in data for F-OLAM sample (a relatively small deviation from ideal S=1/2 behavior is due to coupling with the residual orbital magnetic moment associated with the Ti^{3+} site symmetry).

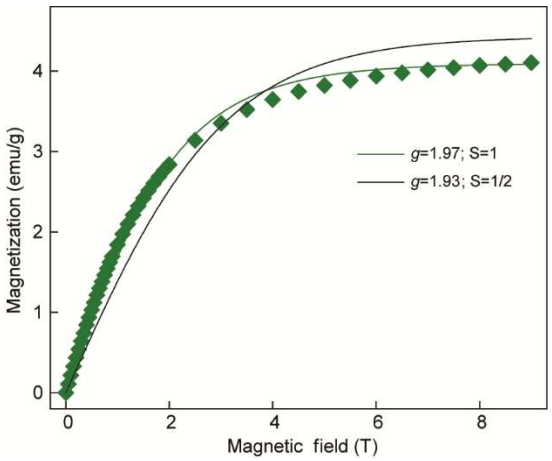

Figure 5.15 Comparison between the Brillouin fits (solid lines) to the experimental magnetization data for M-OLAM sample (green diamonds) for S=1/2 (black line) and S=1 (green line). The g-values used for fitting are the characteristic values for different Ti^{3+} species, as discussed in the main text. The best agreement between the fit and the experimental data is obtained for high spin state (S=1), which corresponds to Ti^{3+} exchange-coupled pairs. Minor deviation of the experimental data points from the S=1 Brillouin fit can be associated with the presence of a small fraction isolated Ti^{3+} (S=1/2).

5.5 Conclusion

TiO_2 NCs with different morphologies were synthesized. The detailed XRD and TEM analysis demonstrates the correlation between the degree of truncation and a percentage of {001} plane, which is associated with plasmonic properties as shown by the absorption measurements. The structural analysis also indicates the existence of surface oxygen vacancies in F-OLAM, while M-OLAM has appreciable amount of bulk oxygen vacancies. The location of oxygen vacancies was associated with the formation of individual or exchanged-coupled Ti^{3+} pairs as implied by the EPR and magnetization measurements. The MCD measurement shows the room-temperature MCD splitting in plasmonic TiO_2 NCs enabled by the coupling between magnetoplasmonic modes and exciton which attests the generality of this phenomenon. In addition, at low temperature, both individual Ti^{3+} in F-OLAM, and exchanged coupled Ti^{3+} pairs in M-OLAM can induce the splitting of semiconductor band states.

Chapter 6
Conclusions and Future Work

6.1 Conclusion

The studies performed as a part of this thesis focus on the plasmon-induced carrier polarization in plasmonic semiconductor NCs. I demonstrated a robust electron polarization in degenerately doped In_2O_3 NCs, enabled by non-resonant coupling of cyclotron magnetoplasmonic modes with the exciton at the Fermi level. We hypothesize that optical phonons play a particularly important role in this non-resonant coupling, because they couple with both excitons and plasmons in semiconductor NCs. Importantly, the phonons can transfer angular momentum, which allows for both the generation of the magnetoplasmonic modes and the splitting of the band states in an external magnetic field. In addition, we studied the exciton splitting in In_2O_3 NCs synthesized under different conditions and different Sn^{4+} doping concentrations. The results demonstrated the control of the nature of band splitting in plasmonic semiconductor NCs that do not contain any magnetic dopants by controlling their electronic structure and the type and concentration of defects acting as electron donors and traps. The extent of carrier localization in point-defect states is determined by the defect configuration in the NC lattice having a particular crystal structure, and the sample preparation conditions. In addition to enhanced LSPR, increase in aliovalent doping concentration also induces the formation of additional lattice defects due to charge compensation, leading to an increase in the number of localized carriers trapped in these sites. The concentration of carriers in plasmonic semiconductor NCs can be effectively controlled either electrochemically or chemically via charge transfer-based electron injection, potentially enabling a dynamic control of carrier polarization in this class of materials. The ability to control exciton polarization in In_2O_3 NCs using both individual (localized) and collective (plasmonic) electronic properties asserts them as multifunctional materials with interacting degrees of freedom (charge, spin, and plasmon) and allows for the possibility of using these materials for spintronics and quantum information processing.

To develop deeper understanding of the effects governing magnetoplasmon-induced excitonic splitting, I also reported the synthesis and comparative characterization of the electronic structure and plasmonic properties of IMO and IWO NCs. Although both Mo and W belong to group VI of the periodic table of elements and have very similar ionic radii and chemical behavior in a given oxidation state, they also exhibit some notable differences as aliovalent dopants in In_2O_3 NCs. Most notably, W exists predominantly in 6+ oxidation state, while Mo coexists as Mo^{5+} and Mo^{6+}, with Mo^{5+} having

negligible contribution to the generation of free conduction band electrons. This difference in average oxidation states is responsible for lower dopant activation in IMO compared to IWO NCs. The ability to achieve different dopant activation in IMO and IWO NCs enabled us to modulate plasmonic properties of otherwise structurally and chemically similar systems and observe phenomena associated with non-resonant interactions between plasmon and exciton in an external magnetic field. Using MCD spectroscopy, this thesis demonstrates that that the excitonic splitting of the NC host lattice is correlated with the LSPR intensity, suggesting the key role of the oscillator strength of the magnetoplasmonic modes in imparting angular momentum to the conduction band states. However, in aliovalently doped semiconductor NCs dopant-related increase in the free electron density is accompanied by ionized impurity scattering and a decrease in carrier mobility. This phenomenon leads to dephasing of the magnetoplasmonic oscillations and reduces the magnitude of the angular momentum transfer to the excitonic states. The achieved excitonic splitting is a result of the trade-off between these two opposite effects - plasmon oscillator strength and electron damping. It is quite possible and even likely that other structural parameters (electronic and lattice) also play an important role, which is a subject of ongoing investigations. The results of this work provide a guideline for the rational design and optimization of plasmonic semiconductor NCs as multifunctional materials with correlated plasmon and charge degrees of freedom.

I also demonstrated highly selective morphology-induced control of carrier polarization in oxygen-deficient TiO_2 NCs. Simultaneous generation of LSPR and self-doping in TiO_2 NCs arise from the intrinsic redox chemistry involving oxygen vacancies, which can be controlled via surface ligation and NC morphology. The fluoride-induced oxygen vacancy electronic states are responsible for donating free electrons to the conduction band and the formation of cyclotron magnetoplasmonic modes upon excitation with circularly polarized light in a magnetic field. Free electrons arising from the presence of oxygen vacancies can also localize on titanium sites, reducing Ti(IV) to Ti(III) which acts as a self dopant. In F-OLAM TiO_2 nanoplatelets having a large fraction of fluoride-stabilized {001} facets, oxygen vacancies are predominantly formed as near-surface defects, resulting in localized surface-segregated Ti(III) sites with single unpaired electrons (S = 1/2). On the other hand, in truncated square bipyramidal M-OLAM NCs having a smaller percentage of {001}surface area and larger bulk volume oxygen vacancies can be stabilized internally, resulting in the formation of two adjacent vacancy-bridged Ti(III) sites which are exchange-coupled to produce triplet state (S = 1). Surprisingly, all species (magnetoplasmon, individual and exchange-coupled Ti(III) centers) lead to distinct excitonic splitting pattern. Controlling the redox properties of specific vacancy sites allows for selective carrier

polarization and the formation of discrete quantum states. The main ramification in this work is that complex multifunctional materials with multiple interacting degrees of freedom (plasmon, spin, and charge), relevant for emerging quantum technology applications, can be designed by simple control of the morphology and faceting of colloidal plasmonic semiconductor NCs.

6.2 Future Work

We propose that the plasmon-induced carrier polarization in plasmonic semiconductor NCs is mediated by optical phonons. To shine more light on the mechanism, it is important to further expand the library of plasmonic samples of in which the phonon and magneto-optical properties will be thoroughly investigated. Nonstoichiometric InN NCs could be one of the intriguing systems because it is a more technologically relevant III-V semiconductor. In addition, as discussed in section 1.4.1, the plasmon-phonon interaction in III-V semiconductor thin films has been extensively studied which provides the base for our investigation of the possible plasmon-phonon coupling in InN NCs. The resonant Raman spectroscopy allows us to probe the coupled plasmon-phonon modes and in conjunction with the excitonic splitting measured by MCD spectroscopy, we could establish the correlation between the phonon and the carrier polarization in InN NCs. Furthermore, we could perform the time-resolved absorption experiments in which we will pump InN NCs using radiation above its band-gap energy and probe the plasmon absorption and possibly even the coupled phonon modes. This experiment can reveal the dynamics of exciton, plasmon, as well as phonon in InN NCs and provide more evidence of the interaction between these quasiparticles. It is also an intriguing possibility to use helicity-resolved Raman spectroscopy to investigate the interaction between optical phonons and photons with opposite helicity which could help us understand angular momentum transfer process associated with optical phonons and the resulting carrier polarization in plasmonic semiconductor NCs.

Dynamic tuning of magnetoplasmonic properties and the subsequent carrier polarization will also be important for both comprehensive understanding of the plasmon-exciton interaction in semiconductors and the practical use of plasmonic semiconductor NCs in the optoelectronic devices. As mentioned before (see section 1.1.4), LSPR in semiconductor NCs can be readily tuned by electrochemical charging/discharging. Thus, it is highly relevant to perform *in-situ* MCD measurement of semiconductor NCs in the battery-type cell under different potentials. This would allow us to identify unambiguously the effect of carrier concentration on the magneto-plasmonic properties and the

plasmon-exciton coupling in semiconductor NCs without the interference of structural change associated with aliovalent doping or change in synthesis conditions.

Appendix A

Low-Frequency Absorption Measurement of Oxygen Deficient In_2O_3 NCs

The absorption spectra of pure In_2O_3 nanoparticles synthesized under argon atmosphere at low energy range were confirmed by using the set-up illustrated in Figure A.1a. Black body radiator (Newport Oriel 67000 series) was set at 1000 K to generate the low-frequency emission as a source. After the beam passes through a KBr beam splitter and CsI substrate with deposited sample, the transmission spectrum is collected by the MIR detector (DTGS-PE, Bruker IFS 66v/S). The black trace in Figure A. 1b shows the emission spectrum after passing the radiation beam through beam splitter and CsI pellet without a sample. With successive deposition of a NC suspension on the CsI substrate, the intensity of transmitted light decreased accordingly, indicating the absorption by In_2O_3 NCs. The absorption spectrum shown as black trace in Figure A.1c was obtained by taking the difference between the transmitted spectra before and after adding sample suspension. The result is in a good agreement with the spectrum acquired by FTIR measurement.

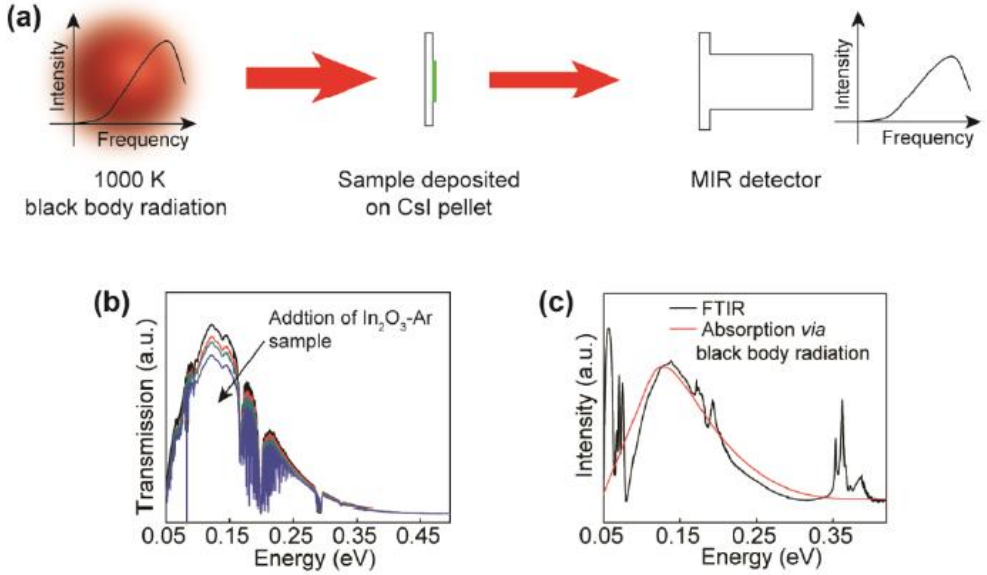

Figure A. 1 (a) Schematic representation of the set-up for measurement of absorption spectra in MIR range using black body radiation source. (b) Raw transmission data for In_2O_3 NCs synthesized in argon for different amounts of sample deposited on CsI substrate. (c) Comparison of the absorption spectra obtained by FTIR spectrometer and using a set-up in (a). The LSPR spectra are essentially identical for both methods.

Appendix B
Landau Level Spectroscopy

The cyclotron motion of a free electron in solid state materials caused by an external magnetic field can also give rise to the formation of Landau states, which are associated with the Landau diamagnetism. It is therefore instructive to briefly compare and contrast the spectroscopic properties of the Landau states with those of the magnetoplasmonic modes observed in this work. The Schrödinger equation for the cyclotron motion of free electrons in a magnetic field has a harmonic oscillator form[212], with the characteristic angular rotation frequency (ω_c) of the harmonic oscillator expressed as:

$$\omega_c = \frac{eB}{m*c} \qquad \textbf{(Equation B1)}$$

where m* is the effective mass of the carrier. The energy eigenvalues (known as Landau levels) for an electron in a parabolic band in a semiconductor are then given by:

$$E_{N,m_S} = \frac{\hbar^2 k_z^2}{2m_{||}^*} + \hbar\omega_c\left(N + \frac{1}{2}\right) - g_S\mu_B m_S B \qquad \textbf{(Equation B2)}$$

where $m_{||}^*$ is the effective mass component along the magnetic field, k_z is the wave vector in the direction of the magnetic field, N is the Landau quantum number (N =0, 1, 2,…), and m_S is the magnetic spin quantum number ($m_S = \pm 1/2$). According to last term of eq. B2 each Landau level is split into two sublevels due to spin-orbit coupling determined by the Landé g factor (Figure B.1a). This quantization of the Landau levels gives rise to a variety of magneto-oscillatory phenomena. Importantly for this work, the interband (exciton) absorption transitions involving Landau levels obey the selection rule $\Delta N = 0$ (Figure B.1a).[213] The transition energies for the corresponding MCD spectra in Faraday configuration for left ($h\nu_N^-$) and right ($h\nu_N^+$) circularly polarized light are defined as:

$$h\nu_N^{\mp} = E_g + \frac{\hbar^2 k_z^2}{2m_r^*} + \hbar\omega_c\left(N + \frac{1}{2}\right) \pm \frac{1}{2}\bar{g}\,\mu_B B \qquad \textbf{(Equation B3)}$$

where E_g is the optical bandgap energy, m_r^* is the reduced effective mass of the bands and ω_c is the associated cyclotron frequency, and $\bar{g}$ is the combined g-factor of both bands. The dependence of transitions energies on N results in the periodic oscillatory structure of both absorption and MCD spectra (Figure B.1b), which is a signature of the Landau level spectroscopy.[213] Furthermore, the spin-orbit splitting of the Landau states shown in Figure B.1a leads to both positive and negative MCD bands. As emphasized in the main text, in addition to robust MCD signal at high temperature (above 300 K) and low field (below 1 T), the absence of any periodic variations in either absorption or MCD spectra and the presence of only negative MCD signal at high temperatures demonstrate that carrier polarization in plasmonic semiconductor NCs reported in this work is associated with circular magnetoplasmonic resonance as a collective behaviour of free electrons.

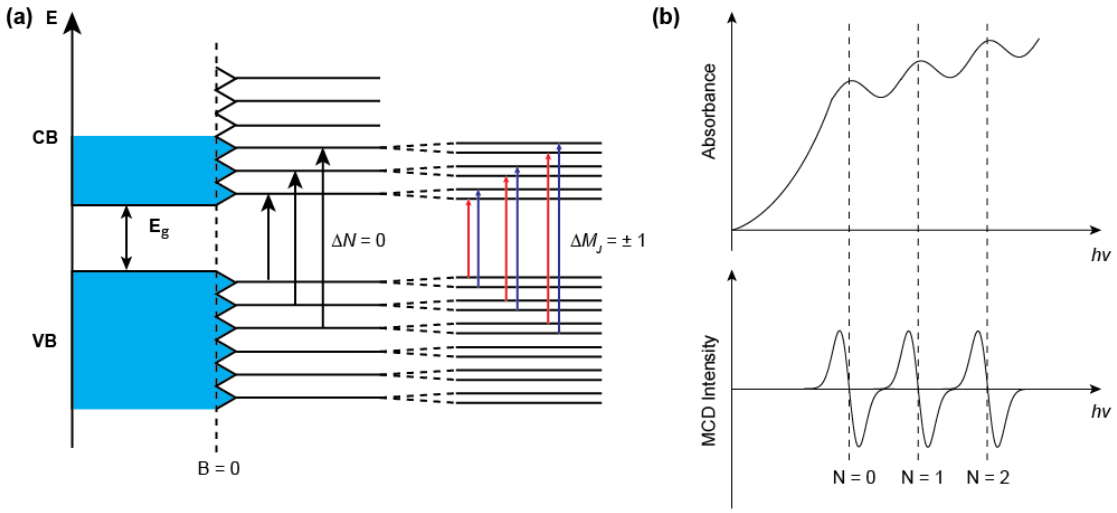

Figure B. 1 (a) Schematic representation of the Landau levels for the valence band (VB) and the conduction band in an external magnetic field (B). Interband absorption and MCD transitions involving these Landau levels are shown with arrows; b, Exciton absorption (top part) and MCD (bottom part) spectra corresponding to the transitions indicated in (a) which result in the characteristic oscillatory patterns.

Appendix C

Calculated Band Structure of In_2O_3 and ITO

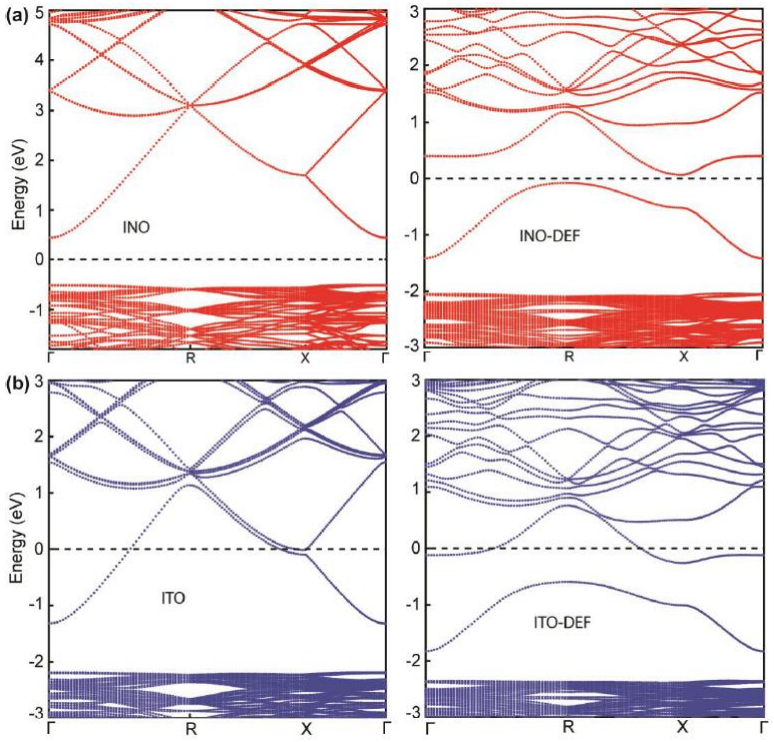

Figure C.1 Calculated band structures for (a) In_2O_3 and (b) 3.125 % Sn^{4+}-doped In_2O_3 (ITO). The calculations were performed for the ideal lattices (left panels) and upon introduction of one oxygen vacancy per supercell (right panels). The electronic structures of In_2O_3 and ITO are in a very good agreement with the theoretical results reported in the literature.

Appendix D

Additional Structural Information of IMO and IWO NCs

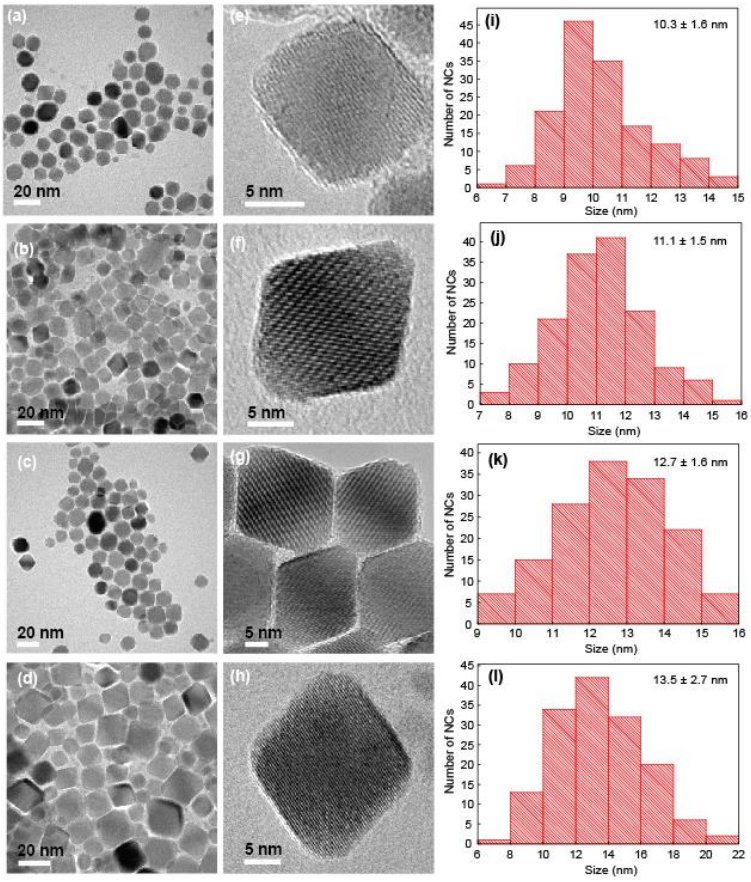

Figure D.1 a-d, Overview TEM images of IMO NCs with (a) 0.3 %, (b) 1.4 %, (c) 4.2 %, and (d) 9.2 % Mo doping concentrations, and corresponding high-resolution TEM images (e-h), andsize distribution histograms (i-l).

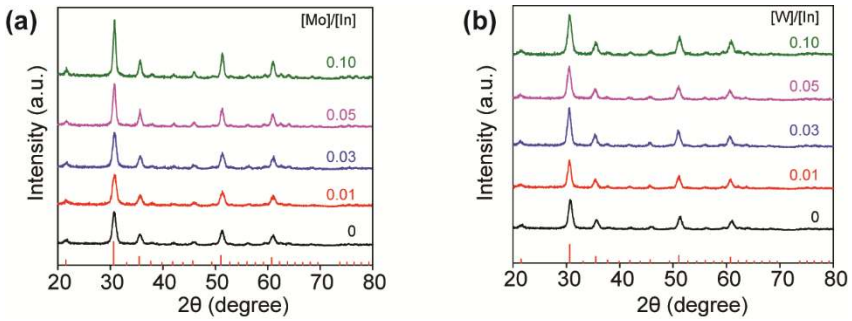

Figure D.2 XRD patterns of (a) IMO and (b) IWO NCs synthesized with different dopant to indium precursor ratio, as indicated in the graph. Vertical lines indicate the bulk XRD pattern of cubic bixbyite-type In_2O_3.

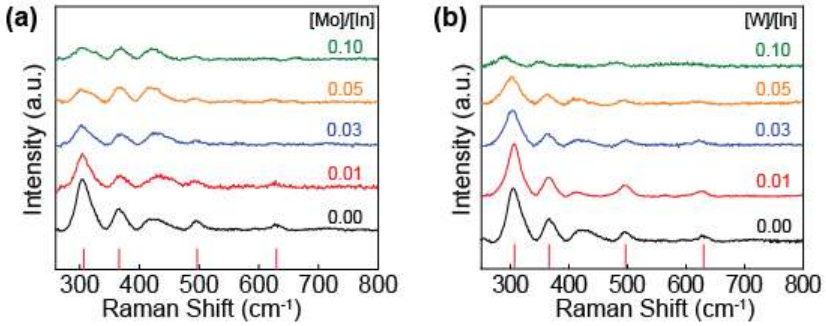

Figure D.3 Raman Spectra of (a) IMO and (b) IWO NCs synthesized with different dopant to indium precursor ratio, as indicated in the graph. Vertical lines indicate the position of Raman spectrum of bulk cubic bixbyite-type In_2O_3.

Appendix E

Modelling of the LSPR Spectra Using Drude Model

The extraction of the plasmonic parameters from LSPR absorption spectra can be performed starting with the fundamental expression for absorbance (A):

$$A = \rho_{\mathrm{NC}} \sigma l \qquad \textbf{(Equation E1)}$$

where ρ_{NC} is the NC density in a colloidal suspension (i.e., number of NCs/cm^3), l is the absorption path length, and σ is the NC absorption cross section defined as:

$$\sigma = 4\pi k R^3 \,\mathrm{Im}\left\{\frac{\varepsilon(\omega) - \varepsilon_{\mathrm{KBr}}}{\varepsilon(\omega) + 2\varepsilon_{\mathrm{KBr}}}\right\} \qquad \textbf{(Equation E2)}$$

where $\varepsilon(\omega)$ is the frequency-dependent dielectric function for doped In_2O_3, ε_{KBr} is the dielectric constant of KBr as a matrix for infrared absorption measurements (2.36),[214] $k = \frac{\sqrt{\varepsilon_{\mathrm{KBr}}}\,\omega}{c}$, and R is the average NC radius. Using Eq. 4.1 in the main text for , σ the can be expressed in terms of plasmonic parameters (ω_p and Γ), allowing for fitting the absorption spectra in Figure E.1.

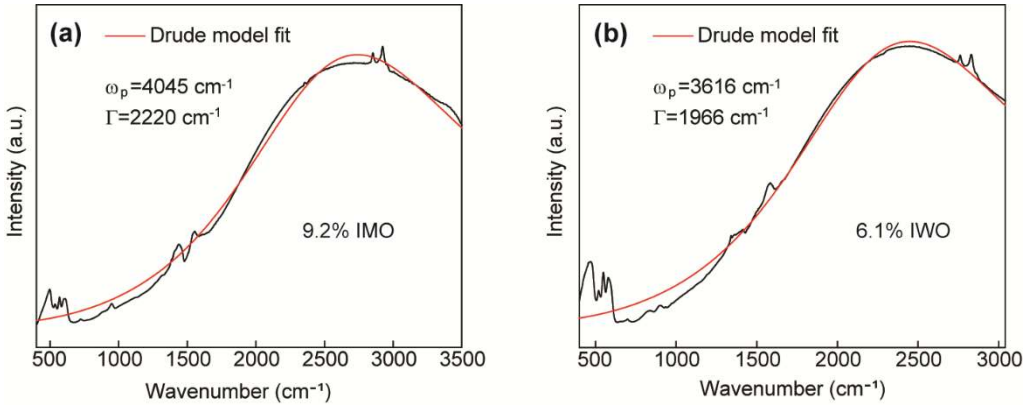

Figure E.1 (a) Drude model analysis of the LSPR spectra of (a) 9.2% IMO and (b) 6.1% IWO NCs. Modeling of the LSPR spectra was performed as described in ref. 56 in the Chapter 4 (see details above). The plasmonic parameters (ω_p and Γ) indicated in the graph were obtained as free parameters from the best fits to the experimental spectra.

Appendix F

Origin of the Difference in Morphology of TiO_2 NCs

In case of TiF_4 precursor, F^- ions, formed in situ during the coordination of oleic acid to dissolved Ti^{4+}, can selectively bind to {001} facets of nucleated anatase TiO_2 NCs and act as a morphology-controlling agent (ref. 185 in the main text). This selective coordination of fluoride ions hinders nanocrystal growth along <001> direction, and results in the formation of platelet-like NCs. When TiF_4 and $TiCl_4$ mixture is used, the amount of HF generated during the synthesis is significantly reduced, which leads to the formation of truncated bipyramidal NCs with a relatively small surface area percentage of {001} facets, and a large percentage of {101} facets. Correspondingly, by using $TiCl_4$ precursor alone, the fraction of the {001} facets is expected to be the smallest among the three samples shown in Figure 5.1. It has been reported that ODOL could be used as the provider of the hydroxyl groups in non-aqueous colloidal synthesis of metal oxide NCs.[215] The presence of ODOL as a coordinating ligand (or co-surfactant) in this synthesis can therefore accelerate the hydroxylation of Ti^{4+} in solution and the ensuing polymerization, resulting in the faster NC growth, as evident from the results in Figure 5.1 and Figure 5.2. By using a specific combination of precursors and coordinating ligands, one can systematically control the morphology and size of the TiO_2 NCs, and ultimately the formation of native defect states (see the discussion in the main text).

We note that majority of F-OLAM and M-OLAM NCs in Figures F.2 and F.3 appear relatively similar. The main reason for that similarity is that most F-OLAM and M-OLAM NCs are oriented along <001> direction (i.e., they rest on a {001} facet formed by truncation of the square bipyramidal NCs during their growth in solution), resulting in square projections when viewed along [001] zone axis. However, M-OLAM NCs have a significantly higher contrast, indicating a higher thickness due to lower degree of NC truncation, consistent with the nanocrystal drawing in Figure 5.1a (inset).

The average thickness of F-OLAM NCs is measured to be ca. 5 nm for nanoplatelets oriented perpendicular to the square base (Figure F.2). On the other hand, M-OLAM samples do not show any "rod-like" features expected for nanoplatelets rotated 90 degrees relative to the square base (Figure F.3). A different orientation of these non-spherical M-OLAM NCs is the reason why some NCs appear to have a different shape in TEM images. Nevertheless, based on the large overview image (Figure F.3), it is clear that these M-OLAM NCs are highly uniform in size. Importantly, using CrysTBox program analysis, we performed a detailed analysis of high resolution TEM images and the corresponding electron diffraction patterns, which allowed us to elucidate the orientation and faceting

of the representative NCs (Figure 5.1b and Figure F.1), as discussed in the manuscript. Specifically, a lower degree of truncation implies smaller fraction of {001} faceting in M-OLAM relative to F^-OLAM NCs which is also well-correlated with the concentration of free electrons. Similar analysis for Cl-ODOL NCs (Figure 5.1b and Figure F.1) revealed somewhat more complex NC faceting, but most importantly confirmed a much lower degree of truncation along <001> direction. This faceting results in elongated "rice-like" morphology of Cl-ODOL NCs, which is one of the common morphologies of TiO_2 NCs.[216] This elongated "nanorice" morphology is also evident from the overview TEM images in Figure 5.1b (bottom panels), despite varying NC orientation, similarly to M-OLAM NCs. Importantly for this study, the fraction of {001} faceting is well-correlated with the concentration of charge carriers, which is ultimately enabled by fluoride ions, as discussed above. This analysis unambiguously demonstrates the correlation between the degree of truncation and a percentage of {001} plane, which is associated with plasmonic properties.

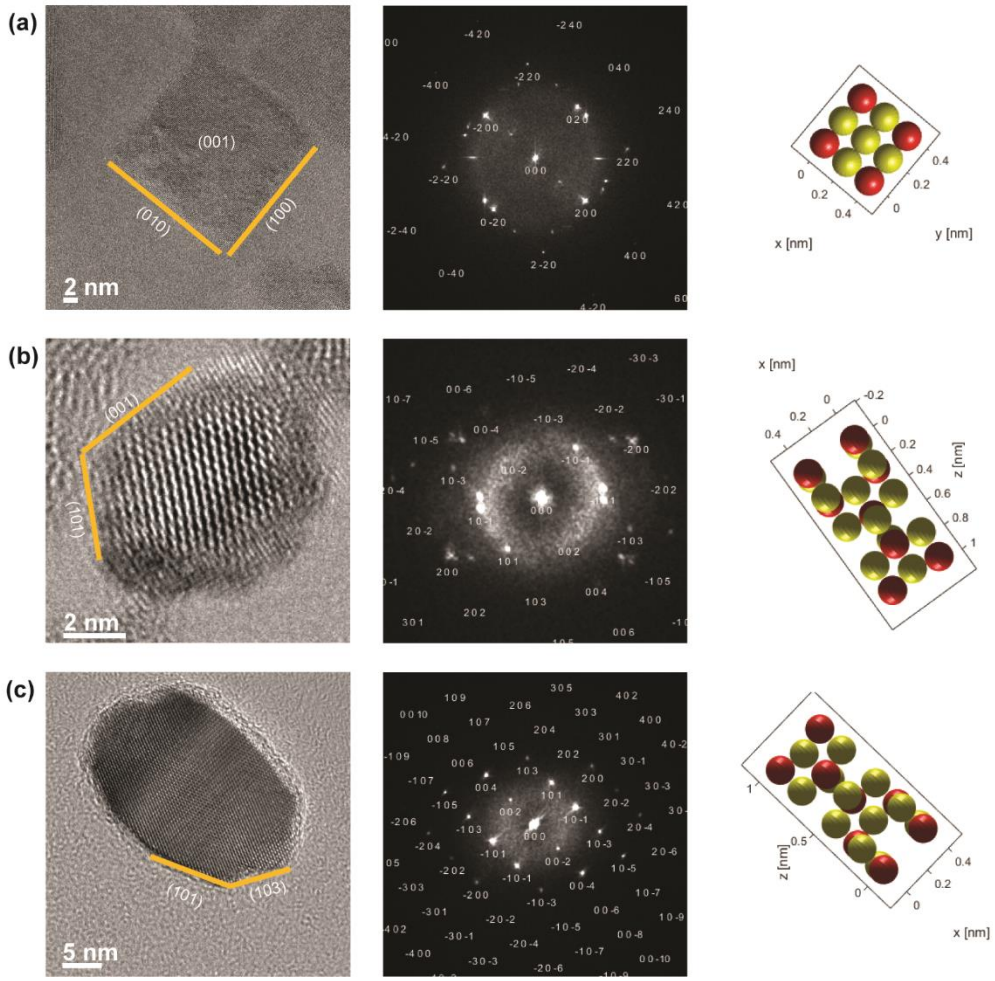

Figure F.1 Lattice-resolved TEM images (left panels), their Fourier transform (middle panels), and atomic simulation of the corresponding crystal lattice orientation (right panels) for (a) F-OLAM NCs, (b) M-OLAM NCs, and (c) Cl-ODOL NCs. Orange lines in TEM images designate the lattice planes, as indicated. Red spheres in right hand side panels indicate titanium and yellow spheres oxygen atoms.

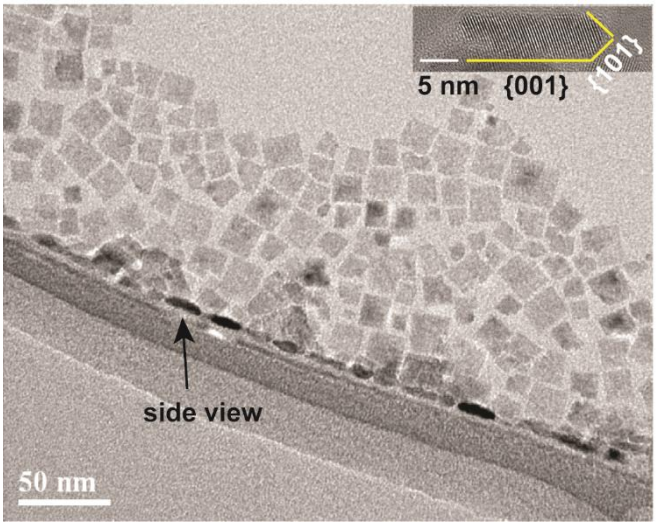

Figure F.2 Overview TEM image of F-OLAM NCs showing different NC orientations. Side view of a typical nanoplatelet oriented perpendicular to the square base is indicated with an arrow. Inset: high-resolution TEM image of a nanoplatelet oriented perpendicular to the square base, indicating relevant lattice planes.

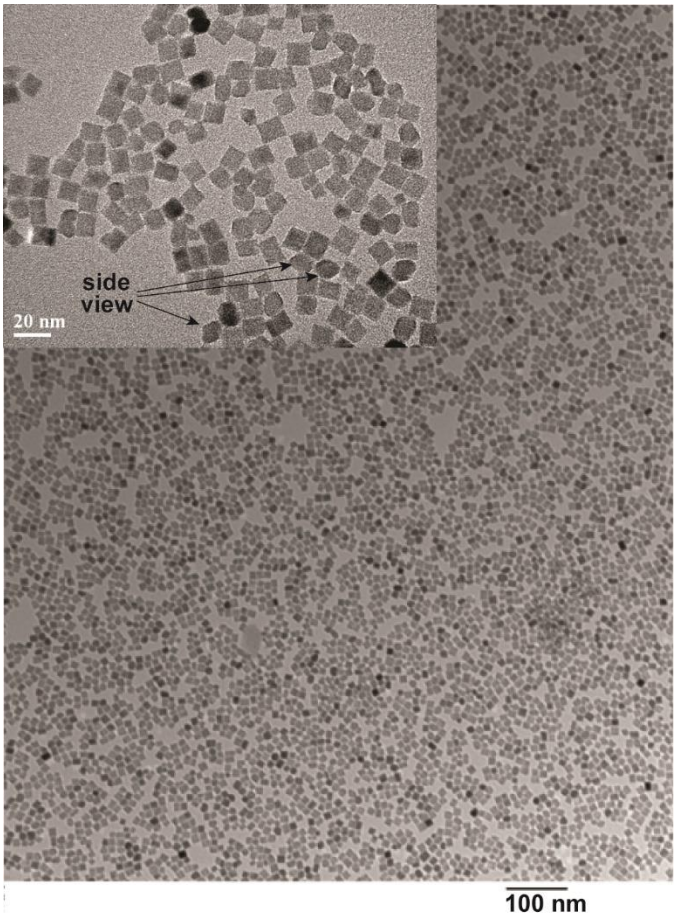

Figure F.3 Overview TEM image of M-OLAM NCs showing NC uniformity throughout the sample. Inset: zoom-in of the overview image showing different NC orientations. Typical truncated square bipyramidal NCs oriented perpendicular to the square base are indicated with an arrow. High-resolution TEM of a M-OLAM NC oriented perpendicular to the NC square base is shown in Figure 5.1b (middle). Additional discussion about NC faceting, including the difference between F-OLAM and M-OLAM NCs is given the text above.

Appendix G

Characterization and Magneto-Optical Properties of $WO_{2.72}$ NCs

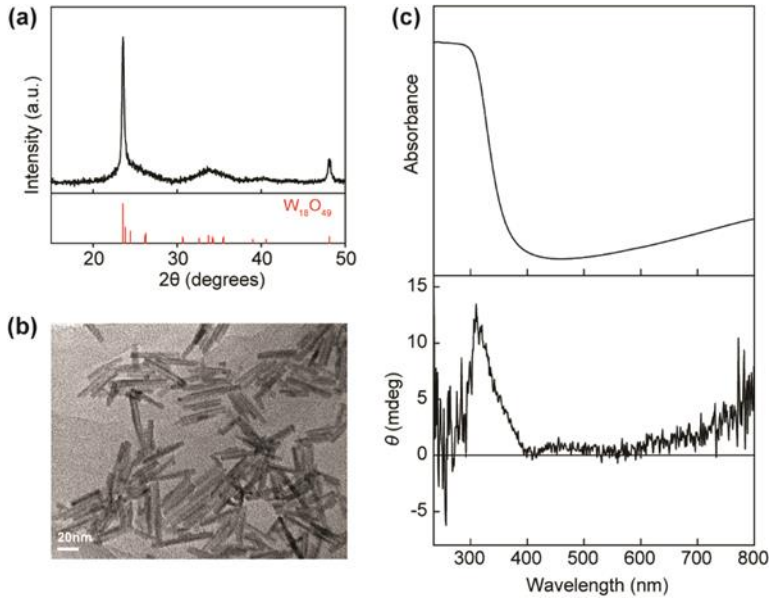

Figure G.1 Characterization and magneto-optical properties of $WO_{2.72}$ NCs. (a) XRD pattern of $WO_{2.72}$ NCs, prepared by modifying a procedure used for the synthesis of tungsten nanoparticles.[217] The XRD pattern of the nanocrystal sample agrees well with that reported for $WO_{2.72}$ phase (red sticks, JCPDS-084-1516). (b) TEM image of $WO_{2.72}$ sample in (a) demonstrating the formation of nanorods. (c) 300 K absorption (top panel) and MCD (bottom panel) spectra of the same $WO_{2.72}$ nanorods. In addition to the excitonic absorption with the onset at ca. 400 nm, a broad feature extending into NIR range corresponds to LSPR, consistent with the previously reported results for similar NCs. Importantly, a positive sign of the excitonic MCD band with the maximum at ca. 300 nm is observed, similar to TiO_2 NCs.

Bibliography

1. Maier, S. A., *Plasmonics: Fundamentals and Applications*. Springer: New York, 2007.

2. Giannini, V.; Fernandez-Dominguez, A. I.; Heck, S. C.; Maier, S. A., *Chem. Rev.* **2011,** *111*, 3888-3912.

3. Atwater, H. A.; Polman, A., *Nat. Mater.* **2010,** *9*, 205-213.

4. Stewart, M. E.; Anderton, C. R.; Thompson, L. B.; Maria, J.; Gray, S. K.; Rogers, J. A.; Nuzzo, R. G., *Chem. Rev.* **2008,** *108*, 494-521.

5. Huang, X.; Jain, P. K.; El-Sayed, I. H.; El-Sayed, M. A., *Lasers Med. Sci.* **2008,** *23*, 217-228.

6. Comin, A.; Manna, L., *Chem. Soc. Rev.* **2014,** *43*, 3957-3975.

7. Agrawal, A.; Cho, S. H.; Zandi, O.; Ghosh, S.; Johns, R. W.; Milliron, D. J., *Chem. Rev.* **2018,** *118*, 3121-3207.

8. Luther, J. M.; Jain, P. K.; Ewers, T.; Alivisatos, A. P., *Nat. Mater.* **2011,** *10*, 361-366.

9. Kanehara, M.; Koike, H.; Yoshinaga, T.; Teranishi, T., *J. Am. Chem. Soc.* **2009,** *131*, 17736-17737.

10. Mattox, T. M.; Bergerud, A.; Agrawal, A.; Milliron, D. J., *Chem. Mater.* **2014,** *26*, 1779-1784.

11. Manthiram, K.; Alivisatos, A. P., *J. Am. Chem. Soc.* **2012,** *134*, 3995-3998.

12. Fang, H.; Hegde, M.; Yin, P.; Radovanovic, P. V., *Chem. Mater.* **2017,** *29*, 4970-4979.

13. Balitskii, O. A.; Sytnyk, M.; Stangl, J.; Primetzhofer, D.; Groiss, H.; Heiss, W., *ACS Appl. Mater. Interfaces* **2014,** *6*, 17770-17775.

14. Tandon, B.; Yadav, A.; Khurana, D.; Reddy, P.; Santra, P. K.; Nag, A., *Chem. Mater.* **2017,** *29*, 9360-9368.

15. Wang, T.; Radovanovic, P. V., *J. Phys. Chem. C* **2010,** *115*, 406-413.

16. Della Gaspera, E.; Chesman, A. S.; van Embden, J.; Jasieniak, J. J., *ACS Nano* **2014,** *8*, 9154-9163.

17. Gordon, T. R.; Paik, T.; Klein, D. R.; Naik, G. V.; Caglayan, H.; Boltasseva, A.; Murray, C. B., *Nano Lett.* **2013,** *13*, 2857-2863.

18. zum Felde, U.; Haase, M.; Weller, H., *J. Phys. Chem. B* **2000,** *104*, 9388-9395.

19. De Trizio, L.; Buonsanti, R.; Schimpf, A. M.; Llordes, A.; Gamelin, D. R.; Simonutti, R.; Milliron, D. J., *Chem. Mater.* **2013,** *25*, 3383-3390.

20. Yin, H.; Kuwahara, Y.; Mori, K.; Cheng, H.; Wen, M.; Yamashita, H., *J. Mater. Chem. A* **2017,** *5*, 8946-8953.

21. Agoston, P.; Albe, K.; Nieminen, R. M.; Puska, M. J., *Phys. Rev. Lett.* **2009,** *103*, 245501.

22. Burbano, M.; Scanlon, D. O.; Watson, G. W., *J. Am. Chem. Soc.* **2011,** *133*, 15065-15072.

23. Peelaers, H.; Chabinyc, M. L.; Van de Walle, C. G., *Chem. Mater.* **2017,** *29*, 2563-2567.

24. Chen, A.; Zhu, K.; Zhong, H.; Shao, Q.; Ge, G., *Sol. Energy Mater. Sol. Cells* **2014,** *120*, 157-162.

25. Hu, H.; Ji, H. F.; Sun, Y., *Phys. Chem. Chem. Phys.* **2013,** *15*, 16557-16565.

26. Yin, P.; Hegde, M.; Tan, Y.; Chen, S.; Garnet, N.; Radovanovic, P. V., *ACS Nano* **2018,** *12*, 11211-11218.

27. Gordon, T. R.; Cargnello, M.; Paik, T.; Mangolini, F.; Weber, R. T.; Fornasiero, P.; Murray, C. B., *J. Am. Chem. Soc.* **2012,** *134*, 6751-6761.

28. Ke, Y.; Wen, X.; Zhao, D.; Che, R.; Xiong, Q.; Long, Y., *ACS Nano* **2017,** *11*, 7542-7551.

29. Ghosh, S.; Lu, H. C.; Cho, S. H.; Maruvada, T.; Price, M. C.; Milliron, D. J., *J. Am. Chem. Soc.* **2019**.

30. Runnerstrom, E. L.; Bergerud, A.; Agrawal, A.; Johns, R. W.; Dahlman, C. J.; Singh, A.; Selbach, S. M.; Milliron, D. J., *Nano Lett.* **2016,** *16*, 3390-3398.

31. Yin, P.; Tan, Y.; Fang, H.; Hegde, M.; Radovanovic, P. V., *Nat. Nanotechnol.* **2018,** *13*, 463-467.

32. Sachet, E.; Shelton, C. T.; Harris, J. S.; Gaddy, B. E.; Irving, D. L.; Curtarolo, S.; Donovan, B. F.; Hopkins, P. E.; Sharma, P. A.; Sharma, A. L.; Ihlefeld, J.; Franzen, S.; Maria, J. P., *Nat. Mater.* **2015,** *14*, 414-420.

33. Ghosh, S.; Saha, M.; Paul, S.; De, S. K., *Small* **2017,** *13*, 1602469.

34. Hwang, J., *Solid State Ion.* **2000,** *129*, 135-144.

35. Hussain, A.; Gruehn, R.; Rüscher, C. H., *J. Alloys Compd.* **1997,** *246*, 51-61.

36. Alvarez Barragan, A.; Ilawe, N. V.; Zhong, L.; Wong, B. M.; Mangolini, L., *J. Phys. Chem. C* **2017,** *121*, 2316-2322.

37. Palomaki, P. K.; Miller, E. M.; Neale, N. R., *J. Am. Chem. Soc.* **2013,** *135*, 14142-14150.

38. Liu, Z.; Beaulac, R., *Chem. Mater.* **2017,** *29*, 7507-7514.

39. Shen, G.; Guyot-Sionnest, P., *J. Phys. Chem. C* **2016,** *120*, 11744-11753.

40. Goubet, N.; Jagtap, A.; Livache, C.; Martinez, B.; Portales, H.; Xu, X. Z.; Lobo, R.; Dubertret, B.; Lhuillier, E., *J. Am. Chem. Soc.* **2018,** *140*, 5033-5036.

41. Rowe, D. J.; Jeong, J. S.; Mkhoyan, K. A.; Kortshagen, U. R., *Nano Lett.* **2013,** *13*, 1317-1322.

42. Lukashev, P.; Lambrecht, W. R. L.; Kotani, T.; van Schilfgaarde, M., *Phys. Rev. B* **2007,** *76*, 195202.

43. Coughlan, C.; Ibanez, M.; Dobrozhan, O.; Singh, A.; Cabot, A.; Ryan, K. M., *Chem. Rev.* **2017,** *117*, 5865-6109.

44. Jain, P. K.; Manthiram, K.; Engel, J. H.; White, S. L.; Faucheaux, J. A.; Alivisatos, A. P., *Angew. Chem. Int. Ed. Engl.* **2013,** *52*, 13671-13675.

45. Chakrabarti, D. J.; Laughlin, D. E., *Bull. Alloy Phase Diagr.* **1981,** *2*, 305-315.

46. Chakrabarti, D. J.; Laughlin, D. E., *Bull. Alloy Phase Diagr.* **1983,** *4*, 254-271.

47. Kriegel, I.; Rodriguez-Fernandez, J.; Wisnet, A.; Zhang, H.; Waurisch, C.; Eychmuller, A.; Dubavik, A.; Govorov, A. O.; Feldmann, J., *ACS Nano* **2013,** *7*, 4367-4377.

48. Xie, Y.; Riedinger, A.; Prato, M.; Casu, A.; Genovese, A.; Guardia, P.; Sottini, S.; Sangregorio, C.; Miszta, K.; Ghosh, S.; Pellegrino, T.; Manna, L., *J. Am. Chem. Soc.* **2013,** *135*, 17630-17637.

49. Dorfs, D.; Hartling, T.; Miszta, K.; Bigall, N. C.; Kim, M. R.; Genovese, A.; Falqui, A.; Povia, M.; Manna, L., *J. Am. Chem. Soc.* **2011,** *133*, 11175-11180.

50. Liu, X.; Wang, X.; Swihart, M. T., *Chem. Mater.* **2013,** *25*, 4402-4408.

51. Dilena, E.; Dorfs, D.; George, C.; Miszta, K.; Povia, M.; Genovese, A.; Casu, A.; Prato, M.; Manna, L., *J. Mater. Chem* **2012,** *22*, 13023–13031.

52. Wang, J. J.; Xue, D. J.; Guo, Y. G.; Hu, J. S.; Wan, L. J., *J. Am. Chem. Soc.* **2011,** *133*, 18558-18561.

53. Guo, Q.; Yao, Y.; Luo, Z. C.; Qin, Z.; Xie, G.; Liu, M.; Kang, J.; Zhang, S.; Bi, G.; Liu, X.; Qiu, J., *ACS Nano* **2016,** *10*, 9463-9469.

54. Niezgoda, J. S.; Yap, E.; Keene, J. D.; McBride, J. R.; Rosenthal, S. J., *Nano Lett.* **2014,** *14*, 3262-3269.

55. Wang, X.; Swihart, M. T., *Chem. Mater.* **2015,** *27*, 1786-1791.

56. Crockett, B. M.; Jansons, A. W.; Koskela, K. M.; Sharps, M. C.; Johnson, D. W.; Hutchison, J. E., *Chem. Mater.* **2019,** *31*, 3370-3380.

57. Lounis, S. D.; Runnerstrom, E. L.; Bergerud, A.; Nordlund, D.; Milliron, D. J., *J. Am. Chem. Soc.* **2014,** *136*, 7110-7116.

58. Zandi, O.; Agrawal, A.; Shearer, A. B.; Reimnitz, L. C.; Dahlman, C. J.; Staller, C. M.; Milliron, D. J., *Nat. Mater.* **2018,** *17*, 710-717.

59. Johns, R. W.; Bechtel, H. A.; Runnerstrom, E. L.; Agrawal, A.; Lounis, S. D.; Milliron, D. J., *Nat. Commun.* **2016,** *7*, 11583.

60. Kim, J.; Agrawal, A.; Krieg, F.; Bergerud, A.; Milliron, D. J., *Nano Lett.* **2016,** *16*, 3879-3884.

61. Hu, W.; Guo, S.; Gaul, J. P.; Boebinger, M. G.; McDowell, M. T.; Filler, M. A., *J. Phys. Chem. C* **2017,** *121*, 15970-15976.

62. Schimpf, A. M.; Lounis, S. D.; Runnerstrom, E. L.; Milliron, D. J.; Gamelin, D. R., *J. Am. Chem. Soc.* **2015,** *137*, 518-524.

63. Schimpf, A. M.; Thakkar, N.; Gunthardt, C. E.; Masiello, D. J.; Gamelin, D. R., *ACS Nano* **2014,** *8*, 1065-1072.

64. Shim, M.; Guyot-Sionnest, P., *J. Am. Chem. Soc.* **2001,** *123*, 11651-11654.

65. Schimpf, A. M.; Gunthardt, C. E.; Rinehart, J. D.; Mayer, J. M.; Gamelin, D. R., *J. Am. Chem. Soc.* **2013,** *135*, 16569-16577.

66. van der Stam, W.; Gudjonsdottir, S.; Evers, W. H.; Houtepen, A. J., *J. Am. Chem. Soc.* **2017,** *139*, 13208-13217.

67. Dahlman, C. J.; Agrawal, A.; Staller, C. M.; Adair, J.; Milliron, D. J., *Chem. Mater.* **2019,** *31*, 502-511.

68. Llordes, A.; Garcia, G.; Gazquez, J.; Milliron, D. J., *Nature* **2013,** *500*, 323-326.

69. DeForest, N.; Shehabi, A.; Selkowitz, S.; Milliron, D. J., *Appl. Energy* **2017,** *192*, 95-109.

70. Garcia, G.; Buonsanti, R.; Runnerstrom, E. L.; Mendelsberg, R. J.; Llordes, A.; Anders, A.; Richardson, T. J.; Milliron, D. J., *Nano Lett.* **2011,** *11*, 4415-4420.

71. Llorente, V. B.; Dzhagan, V. M.; Gaponik, N.; Iglesias, R. A.; Zahn, D. R. T.; Lesnyak, V., *J. Phys. Chem. C* **2017,** *121*, 18244-18253.

72. Hergert;, W.; Wriedt, T., *The Mie Theory: Basics and Applications*. Springer: Berlin 2012.

73. Fox, M., *Optical Properties of solids*. Oxford University Press: New York, 2001.

74. Gerlach, E., *J. Phys. C: Solid State Phys.* **1986,** *19*, 4585-4603.

75. Chattopadhyay, D.; Queisser, H. J., *Rev. Mod. Phys.* **1981,** *53*, 745-768.

76. Yin, P.; Hegde, M.; Garnet, N. S.; Tan, Y.; Radovanovic, P. V., *Nano Lett.* **2019,** *19*, 6695-6702.

77. Jain, P. K., *J. Phys. Chem. Lett.* **2014,** *5*, 3112-3119.

78. Armelles, G.; Cebollada, A.; García-Martín, A.; González, M. U., *Adv. Opt. Mater.* **2013,** *1*, 10-35.

79. Belotelov, V. I.; Doskolovich, L. L.; Zvezdin, A. K., *Phys. Rev. Lett.* **2007,** *98*, 077401.

80. Belotelov, V. I.; Akimov, I. A.; Pohl, M.; Kotov, V. A.; Kasture, S.; Vengurlekar, A. S.; Gopal, A. V.; Yakovlev, D. R.; Zvezdin, A. K.; Bayer, M., *Nat. Nanotechnol.* **2011,** *6*, 370-376.

81. Pineider, F.; Campo, G.; Bonanni, V.; Fernandez Cde, J.; Mattei, G.; Caneschi, A.; Gatteschi, D.; Sangregorio, C., *Nano Lett.* **2013,** *13*, 4785-4789.

82. Hartstein, K. H.; Schimpf, A. M.; Salvador, M.; Gamelin, D. R., *J. Phys. Chem. Lett.* **2017,** *8*, 1831-1836.

83. March, N. H., *Electron Correlation in Molecules and Condensed Phases*. Springer: New York, 1996.

84. Mooradian, A.; Wright, G. B., *Phys. Rev. Lett.* **1966,** *16*, 999-1001.

85. Mooradian, A.; McWhorter, A. L., *Phys. Rev. Lett.* **1967,** *19*, 849-852.

86. Yokota, I., *J. Phys. Soc. Japan* **1961,** *16*, 2075.

87. Varga, B. B., *Phys. Rev.* **1965,** *137*, A1896-A1902.

88. Kloeckner, K.; Himmerlich, M.; Koch, R. J.; Polyakov, V. M.; Eisenhardt, A.; Haensel, T.; Ahmed, S. I. U.; Krischok, S.; Schaefer, J. A., *Phys. Status Solidi C* **2010,** *7*, 173-176.

89. Faust, A.; Amit, Y.; Banin, U., *J. Phys. Chem. Lett.* **2017,** *8*, 2519-2525.

90. Husanu, A.-M., *Phys. Status Solidi B* **2009,** *246*, 87-91.

91. Rieder, K. H.; Ishigame, M.; Genzel, L., *Phys. Rev. B* **1972,** *6*, 3804-3810.

92. Radović, M.; Dohčević-Mitrović, Z.; Paunović, N.; Bošković, S.; Tomić, N.; Tadić, N.; Belča, I., *J. Phys. D: Appl. Phys.* **2015,** *48*, 065301.

93. Zhu, H.; Yi, J.; Li, M. Y.; Xiao, J.; Zhang, L.; Yang, C. W.; Kaindl, R. A.; Li, L. J.; Wang, Y.; Zhang, X., *Science* **2018,** *359*, 579-582.

94. Chen, H.; Zhang, W.; Niu, Q.; Zhang, L., *2D Mater.* **2018,** *6*, 012002.

95. Drexhage, K. H., IV Interaction of Light with Monomolecular Dye Layers. In *Progress in Optics*, Wolf, E., Ed. Elsevier: 1974; Vol. 12, pp 163-232.

96. Achermann, M., *J. Phys. Chem. Lett.* **2010,** *1*, 2837-2843.

97. Cao, E.; Lin, W.; Sun, M.; Liang, W.; Song, Y., *Nanophotonics* **2018,** *7*, 145-167.

98. Pelton, M.; Sheldon, M.; Khurgin, J., *Nanophotonics* **2019,** *8*, 513-516.

99. Schaadt, D. M.; Feng, B.; Yu, E. T., *Appl. Phys. Lett.* **2005,** *86*, 063106.

100. Wang, Y.; Yang, T.; Tuominen, M. T.; Achermann, M., *Phys. Rev. Lett.* **2009,** *102*, 163001.

101. Wu, D. M.; Garcia-Etxarri, A.; Salleo, A.; Dionne, J. A., *J. Phys. Chem. Lett.* **2014,** *5*, 4020-4031.

102. El Kabbash, M.; Rahimi Rashed, A.; Sreekanth, K. V.; De Luca, A.; Infusino, M.; Strangi, G., *J. Nanomater.* **2016,** *2016*, 4819040.

103. Marin, B. C.; Hsu, S.-W.; Chen, L.; Lo, A.; Zwissler, D. W.; Liu, Z.; Tao, A. R., *ACS Photonics* **2016,** *3*, 526-531.

104. Morfa, A. J.; Rowlen, K. L.; Reilly, T. H.; Romero, M. J.; van de Lagemaat, J., *Appl. Phys. Lett.* **2008,** *92*, 013504.

105. Akimov, A. V.; Mukherjee, A.; Yu, C. L.; Chang, D. E.; Zibrov, A. S.; Hemmer, P. R.; Park, H.; Lukin, M. D., *Nature* **2007,** *450*, 402-406.

106. Bergman, D. J.; Stockman, M. I., *Phys. Rev. Lett.* **2003,** *90*, 027402.

107. Haq, S.; Addamane, S.; Kafle, B.; Huang, D.; Balakrishnan, G.; Habteyes, T. G., *Sci. Rep.* **2017,** *7*, 864.

108. Gomez, D. E.; Vernon, K. C.; Mulvaney, P.; Davis, T. J., *Nano Lett.* **2010,** *10*, 274-278.

109. Liu, W.; Lee, B.; Naylor, C. H.; Ee, H. S.; Park, J.; Johnson, A. T.; Agarwal, R., *Nano Lett.* **2016,** *16*, 1262-1269.

110. Lee, B.; Liu, W.; Naylor, C. H.; Park, J.; Malek, S. C.; Berger, J. S.; Johnson, A. T. C.; Agarwal, R., *Nano Lett.* **2017,** *17*, 4541-4547.

111. Zhang, J.; Tang, Y.; Lee, K.; Ouyang, M., *Nature* **2010,** *466*, 91-95.

112. Zhou, Y.; Scuri, G.; Wild, D. S.; High, A. A.; Dibos, A.; Jauregui, L. A.; Shu, C.; De Greve, K.; Pistunova, K.; Joe, A. Y.; Taniguchi, T.; Watanabe, K.; Kim, P.; Lukin, M. D.; Park, H., *Nat. Nanotechnol.* **2017,** *12*, 856-860.

113. Awschalom, D. D.; Flatté, M. E., *Nat. Phys.* **2007,** *3*, 153-159.

114. Žutić, I.; Fabian, J.; Das Sarma, S., *Rev. Mod. Phys.* **2004,** *76*, 323-410.

115. Schaibley, J. R.; Yu, H.; Clark, G.; Rivera, P.; Ross, J. S.; Seyler, K. L.; Yao, W.; Xu, X., *Nat. Rev. Mater.* **2016,** *1*, 16055.

116. Fert, A., *Rev. Mod. Phys.* **2008,** *80*, 1517-1530.

117. Wolf, S. A.; Awschalom, D. D.; Buhrman, R. A.; Daughton, J. M.; von Molnar, S.; Roukes, M. L.; Chtchelkanova, A. Y.; Treger, D. M., *Science* **2001,** *294*, 1488-1495.

118. Ando, K., *Science* **2006,** *312*, 1883-1885.

119. Baibich, M. N.; Broto, J. M.; Fert, A.; Nguyen Van Dau, F.; Petroff, F.; Etienne, P.; Creuzet, G.; Friederich, A.; Chazelas, J., *Phys. Rev. Lett.* **1988,** *61*, 2472-2475.

120. Binasch, G.; Grunberg, P.; Saurenbach, F.; Zinn, W., *Phys. Rev. B* **1989,** *39*, 4828-4830.

121. Sato, K.; Bergqvist, L.; Kudrnovský, J.; Dederichs, P. H.; Eriksson, O.; Turek, I.; Sanyal, B.; Bouzerar, G.; Katayama-Yoshida, H.; Dinh, V. A.; Fukushima, T.; Kizaki, H.; Zeller, R., *Rev. Mod. Phys.* **2010,** *82*, 1633-1690.

122. Ohno, Y.; Young, D. K.; Beschoten, B.; Matsukura, F.; Ohno, H.; Awschalom, D. D., *Nature* **1999,** *402*, 790-792.

123. Ohno, H.; Chiba, D.; Matsukura, F.; Omiya, T.; Abe, E.; Dietl, T.; Ohno, Y.; Ohtani, K., *Nature* **2000,** *408*, 944-946.

124. Bryan, J. D.; Gamelin, D. R., *Prog. Inorg. Chem.* **2005,** *54*, 47-126.

125. Furdyna, J. K., *J. Appl. Phys.* **1988,** *64*, R29-R64.

126. Novak, V.; Olejnik, K.; Wunderlich, J.; Cukr, M.; Vyborny, K.; Rushforth, A. W.; Edmonds, K. W.; Campion, R. P.; Gallagher, B. L.; Sinova, J.; Jungwirth, T., *Phys. Rev. Lett.* **2008,** *101*, 077201.

127. Dietl, T.; Ohno, H.; Matsukura, F.; Cibert, J.; Ferrand, D., *Science* **2000,** *287*, 1019-1022.

128. Sonoda, S.; Shimizu, S.; Sasaki, T.; Yamamoto, Y.; Hori, H., *J. Cryst. Growth* **2002,** *237-239*, 1358-1362.

129. Matsumoto, Y.; Murakami, M.; Shono, T.; Hasegawa, T.; Fukumura, T.; Kawasaki, M.; Ahmet, P.; Chikyow, T.; Koshihara, S.; Koinuma, H., *Science* **2001,** *291*, 854-856.

130. Bryan, J. D.; Heald, S. M.; Chambers, S. A.; Gamelin, D. R., *J. Am. Chem. Soc.* **2004,** *126*, 11640-11647.

131. Archer, P. I.; Radovanovic, P. V.; Heald, S. M.; Gamelin, D. R., *J. Am. Chem. Soc.* **2005,** *127*, 14479-14487.

132. Radovanovic, P. V.; Gamelin, D. R., *Phys. Rev. Lett.* **2003,** *91*, 157202.

133. Farvid, S. S.; Sabergharesou, T.; Hutfluss, L. N.; Hegde, M.; Prouzet, E.; Radovanovic, P. V., *J. Am. Chem. Soc.* **2014,** *136*, 7669-7679.

134. Coey, J. M. D.; Wongsaprom, K.; Alaria, J.; Venkatesan, M., *J. Phys. D: Appl. Phys.* **2008,** *41*, 134012.

135. Coey, J. M.; Venkatesan, M.; Fitzgerald, C. B., *Nat. Mater.* **2005,** *4*, 173-179.

136. Vitale, S. A.; Nezich, D.; Varghese, J. O.; Kim, P.; Gedik, N.; Jarillo-Herrero, P.; Xiao, D.; Rothschild, M., *Small* **2018,** *14*, 1801483.

137. Ashcroft, N. W.; Mermin, N. D., *Solid State Physics*. Holt, Rinehart and Winston: 1976.

138. Shayegan, M.; De Poortere, E. P.; Gunawan, O.; Shkolnikov, Y. P.; Tutuc, E.; Vakili, K., *Phys. Status Solidi B* **2006,** *243*, 3629-3642.

139. Tsui, D. C.; Kaminsky, G., *Phys. Rev. Lett.* **1979,** *42*, 595-597.

140. Édel'man, V. S., *Adv. Phys.* **1976,** *25*, 555-613.

141. Xiao, D.; Liu, G. B.; Feng, W.; Xu, X.; Yao, W., *Phys. Rev. Lett.* **2012,** *108*, 196802.

142. Xiao, D.; Chang, M.-C.; Niu, Q., *Rev. Mod. Phys.* **2010,** *82*, 1959-2007.

143. Xu, X.; Yao, W.; Xiao, D.; Heinz, T. F., *Nat. Phys.* **2014,** *10*, 343-350.

144. Rycerz, A.; Tworzydło, J.; Beenakker, C. W. J., *Nat. Phys.* **2007,** *3*, 172-175.

145. Cao, T.; Wang, G.; Han, W.; Ye, H.; Zhu, C.; Shi, J.; Niu, Q.; Tan, P.; Wang, E.; Liu, B.; Feng, J., *Nat. Commun.* **2012,** *3*, 887.

146. Mak, K. F.; He, K.; Shan, J.; Heinz, T. F., *Nat. Nanotechnol.* **2012,** *7*, 494-498.

147. Zeng, H.; Dai, J.; Yao, W.; Xiao, D.; Cui, X., *Nat. Nanotechnol.* **2012,** *7*, 490-493.

148. Farvid, S. S.; Dave, N.; Radovanovic, P. V., *Chem. Mater.* **2010,** *22*, 9-11.

149. Farvid, S. S.; Dave, N.; Wang, T.; Radovanovic, P. V., *J. Phys. Chem. C* **2009,** *113*, 15928-15933.

150. Heald, S. M.; Brewe, D. L.; Stern, E. A.; Kim, K. H.; Brown, F. C.; Jiang, D. T.; Crozier, E. D.; Gordon, R. A., *J. Synchrotron Radiat.* **1999,** *6*, 347-349.

151. Mason, W., *A Practical Guide to Magnetic Circular Dichroism Spectroscopy*. Wiley: Hoboken, 2007.

152. Ju, L.; Sabergharesou, T.; Stamplecoskie, K. G.; Hegde, M.; Wang, T.; Combe, N. A.; Wu, H.; Radovanovic, P. V., *J. Am. Chem. Soc.* **2012,** *134*, 1136-1146.

153. Piepho, S. B.; Schatz, P. N., *Group theory in spectroscopy : with applications to magnetic circular dichroism*. Wiley: New York, 1983.

154. Giannozzi, P.; Baroni, S.; Bonini, N.; Calandra, M.; Car, R.; Cavazzoni, C.; Ceresoli, D.; Chiarotti, G. L.; Cococcioni, M.; Dabo, I.; Dal Corso, A.; de Gironcoli, S.; Fabris, S.; Fratesi, G.; Gebauer, R.; Gerstmann, U.; Gougoussis, C.; Kokalj, A.; Lazzeri, M.; Martin-Samos, L.; Marzari, N.; Mauri, F.; Mazzarello, R.; Paolini, S.; Pasquarello, A.; Paulatto, L.; Sbraccia, C.; Scandolo, S.; Sclauzero, G.; Seitsonen, A. P.; Smogunov, A.; Umari, P.; Wentzcovitch, R. M., *J. Phys. Condens. Matter* **2009,** *21*, 395502.

155. Mattioli, G.; Alippi, P.; Filippone, F.; Caminiti, R.; Amore Bonapasta, A., *J. Phys. Chem. C* **2010,** *114*, 21694-21704.

156. Mattioli, G.; Amore Bonapasta, A.; Bovi, D.; Giannozzi, P., *J. Phys. Chem. C* **2014,** *118*, 29928-29942.

157. Wang, C. Y.; Dai, Y.; Pezoldt, J.; Lu, B.; Kups, T.; Cimalla, V.; Ambacher, O., *Cryst. Growth Des.* **2008,** *8*, 1257-1260.

158. Chen, Z.; Huang, L.; Zhang, Q.; Xi, Y.; Li, R.; Li, W.; Xu, G.; Cheng, H., *J. Phys. Chem. C* **2015,** *119*, 4789-4795.

159. Lany, S.; Zunger, A., *Phys. Rev. Lett.* **2007,** *98*, 045501.

160. Walsh, A., *Appl. Phys. Lett.* **2011,** *98*, 261910.

161. Zhang, L.; He, R.; Gu, H.-C., *Appl. Surf. Sci.* **2006,** *253*, 2611-2617.

162. Fedorov, A. V.; Baranov, A. V.; Inoue, K., *Phys. Rev. B* **1997,** *56*, 7491-7502.

163. Beye, M.; Hennies, F.; Deppe, M.; Suljoti, E.; Nagasono, M.; Wurth, W.; Fohlisch, A., *Phys. Rev. Lett.* **2009,** *103*, 237401.

164. Gurlo, A.; Ivanovskaya, M.; Pfau, A.; Weimar, U.; Göpel, W., *Thin Solid Films* **1997,** *307*, 288-293.

165. Gaj, J. A., Chapter 7 Magnetooptical Properties of Large-Gap Diluted Magnetic Semiconductors. In *Semiconductors and Semimetals*, Furdyna, J. K.; Kossut, J., Eds. Elsevier: 1988; Vol. 25, pp 275-309.

166. Alivisatos, A. P.; Harris, A. L.; Levinos, N. J.; Steigerwald, M. L.; Brus, L. E., *J. Chem. Phys.* **1988,** *89*, 4001-4011.

167. Link, S.; El-Sayed, M. A., *J. Phys. Chem. B* **1999,** *103*, 4212-4217.

168. Farvid, S. S.; Hegde, M.; Radovanovic, P. V., *Chem. Mater.* **2013,** *25*, 233-244.

169. Farvid, S. S.; Ju, L.; Worden, M.; Radovanovic, P. V., *J. Phys. Chem. C* **2008,** *112*, 17755-17759.

170. Ulbricht, R.; Hendry, E.; Shan, J.; Heinz, T. F.; Bonn, M., *Rev. Mod. Phys.* **2011,** *83*, 543-586.

171. Bellingham, J. R.; Mackenzie, A. P.; Phillips, W. A., *Appl. Phys. Lett.* **1991,** *58*, 2506-2508.

172. Mryasov, O.; Freeman, A., *Phys. Rev. B* **2001,** *64*, 233111.

173. Reunchan, P.; Zhou, X.; Limpijumnong, S.; Janotti, A.; Van de Walle, C. G., *Curr. Appl. Phys.* **2011,** *11*, S296-S300.

174. Stesmans, A., *Phys. Status Solidi B* **1987,** *143*, 733-740.

175. Choi, J. G.; Thompson, L. T., *Appl. Surf. Sci.* **1996,** *93*, 143-149.

176. Fleisch, T. H.; Mains, G. J., *J. Chem. Phys.* **1982,** *76*, 780-786.

177. Bhachu, D. S.; Scanlon, D. O.; Sankar, G.; Veal, T. D.; Egdell, R. G.; Cibin, G.; Dent, A. J.; Knapp, C. E.; Carmalt, C. J.; Parkin, I. P., *Chem. Mater.* **2015,** *27*, 2788-2796.

178. Ghodsi, V.; Layek, A.; Hegde, M.; Yildirim, B.; Radovanovic, P. V., *Chem. Commun.* **2016,** *52*, 4353-4356.

179. Layek, A.; Yildirim, B.; Ghodsi, V.; Hutfluss, L. N.; Hegde, M.; Wang, T.; Radovanovic, P. V., *Chem. Mater.* **2015,** *27*, 6030-6037.

180. Mendonca, J. T.; Thide, B.; Then, H., *Phys. Rev. Lett.* **2009,** *102*, 185005.

181. Medvedeva, J. E., *Phys. Rev. Lett.* **2006,** *97*, 086401.

182. González, G. B.; Cohen, J. B.; Hwang, J.-H.; Mason, T. O.; Hodges, J. P.; Jorgensen, J. D., *J. Appl. Phys.* **2001,** *89*, 2550-2555.

183. Jayarathne, U.; Chandrasekaran, P.; Greene, A. F.; Mague, J. T.; DeBeer, S.; Lancaster, K. M.; Sproules, S.; Donahue, J. P., *Inorg. Chem.* **2014,** *53*, 8230-8241.

184. Balerna, A.; Bernieri, E.; Burattini, E.; Kuzmin, A.; Lusis, A.; Purans, J.; Cikmach, P., *Nucl. Instrum. Method Phys. Res. A* **1991,** *308*, 240-242.

185. Crockett, B. M.; Jansons, A. W.; Koskela, K. M.; Johnson, D. W.; Hutchison, J. E., *ACS Nano* **2017,** *11*, 7719-7728.

186. Liu, L.; Jiang, Y.; Zhao, H.; Chen, J.; Cheng, J.; Yang, K.; Li, Y., *ACS Catal.* **2016,** *6*, 1097-1108.

187. Yang, H. G.; Sun, C. H.; Qiao, S. Z.; Zou, J.; Liu, G.; Smith, S. C.; Cheng, H. M.; Lu, G. Q., *Nature* **2008,** *453*, 638-641.

188. Huy, H. A.; Aradi, B.; Frauenheim, T.; Deák, P., *Phys. Rev. B* **2011,** *83*, 155201.

189. Nowotny, M. K.; Bak, T.; Nowotny, J., *J. Phys. Chem. B* **2006,** *110*, 16270-16282.

190. Kawamura, K.; Suzuki, N.; Tsuchiya, T.; Shimazu, Y.; Minohara, M.; Kobayashi, M.; Horiba, K.; Kumigashira, H.; Higuchi, T., *Jpn. J. Appl. Phys.* **2016,** *55*, 06GJ08.

191. Chen, H.; Wei, Z.; Yan, K.; Bai, Y.; Yang, S., *J. Phys. Chem. Lett.* **2014,** *5*, 2890-2896.

192. Faucheaux, J. A.; Jain, P. K., *J. Phys. Chem. Lett.* **2013,** *4*, 3024-3030.

193. Schimpf, A. M.; Ochsenbein, S. T.; Buonsanti, R.; Milliron, D. J.; Gamelin, D. R., *Chem. Commun.* **2012,** *48*, 9352-9354.

194. Henderson, G. S.; de Groot, F. M. F.; Moulton, B. J. A., *Rev. Mineral. Geochem.* **2014,** *78*, 75-138.

195. Luca, V.; Djajanti, S.; Howe, R. F., *J. Phys. Chem. B* **1998,** *102*, 10650-10657.

196. Santomauro, F. G.; Lubcke, A.; Rittmann, J.; Baldini, E.; Ferrer, A.; Silatani, M.; Zimmermann, P.; Grubel, S.; Johnson, J. A.; Mariager, S. O.; Beaud, P.; Grolimund, D.; Borca, C.; Ingold, G.; Johnson, S. L.; Chergui, M., *Sci. Rep.* **2015,** *5*, 14834.

197. Fukumura, T.; Yamada, Y.; Tamura, K.; Nakajima, K.; Aoyama, T.; Tsukazaki, A.; Sumiya, M.; Fuke, S.; Segawa, Y.; Chikyow, T.; Hasegawa, T.; Koinuma, H.; Kawasaki, M., *Jpn. J. Appl. Phys.* **2003,** *42*, L105-L107.

198. Yamasaki, T.; Fukumura, T.; Yamada, Y.; Nakano, M.; Ueno, K.; Makino, T.; Kawasaki, M., *Appl. Phys. Lett.* **2009,** *94*, 102515.

199. Asahi, R.; Taga, Y.; Mannstadt, W.; Freeman, A. J., *Phys. Rev. B* **2000,** *61*, 7459-7465.

200. Wang, F.; Di Valentin, C.; Pacchioni, G., *J. Phys. Chem. C* **2011,** *115*, 8345-8353.

201. Clark, R. J. H., 32 - TITANIUM. In *The Chemistry of Titanium, Zirconium and Hafnium*, Clark, R. J. H.; Bradley, D. C.; Thornton, P., Eds. Pergamon: 1973; pp 355-417.

202. Kilty, P. A.; Nicholls, D., *J. Chem. Soc.* **1965**, 4915-4922.

203. Fowles, G. W. A.; Hoodless, R. A.; Walton, R. A., *J. Inorg. Nucl. Chem.* **1965,** *27*, 391-396.

204. Jackman, M. J.; Thomas, A. G.; Muryn, C., *J. Phys. Chem. C* **2015,** *119*, 13682-13690.

205. Weng, H.; Dong, J.; Fukumura, T.; Kawasaki, M.; Kawazoe, Y., *Phys. Rev. B* **2006,** *73*, 121201.

206. Berger, T.; Sterrer, M.; Diwald, O.; Knozinger, E.; Panayotov, D.; Thompson, T. L.; Yates, J. T., Jr., *J. Phys. Chem. B* **2005,** *109*, 6061-6068.

207. Khan, M. M.; Ansari, S. A.; Pradhan, D.; Ansari, M. O.; Han, D. H.; Lee, J.; Cho, M. H., *J. Mater. Chem. A* **2014,** *2*, 637-644.

208. Zhou, S.; Čižmár, E.; Potzger, K.; Krause, M.; Talut, G.; Helm, M.; Fassbender, J.; Zvyagin, S. A.; Wosnitza, J.; Schmidt, H., *Phys. Rev. B* **2009,** *79*, 113201

209. Brant, A. T.; Golden, E. M.; Giles, N. C.; Yang, S.; Sarker, M. A. R.; Watauchi, S.; Nagao, M.; Tanaka, I.; Tryk, D. A.; Manivannan, A.; Halliburton, L. E., *Phys. Rev. B* **2014,** *89*, 115206.

210. Chiesa, M.; Livraghi, S.; Giamello, E.; Albanese, E.; Pacchioni, G., *Angew. Chem. Int. Ed. Engl.* **2017,** *56*, 2604-2607.

211. Strunk, J.; Vining, W. C.; Bell, A. T., *J. Phys. Chem. C* **2010,** *114*, 16937-16945.

212. Dresselhaus, G.; Kip, A. F.; Kittel, C., *Phys. Rev.* **1955,** *98*, 368-384.

213. KeßLer, F. R.; Metzdorf, J., CHAPTER 11 - Landau Level Spectroscopy: Interband Effects and Faraday Rotation. In *Modern Problems in Condensed Matter Sciences*, Landwehr, G.; Rashba, E. I., Eds. Elsevier: 1991; Vol. 27, pp 579-675.

214. Stephens, R. E.; Plyler, E. K.; Rodney, W. S.; Spindler, R. J., *J. Opt. Soc. Am.* **1953,** *43*, 110-112.

215. Cao, S.; Zhang, S.; Zhang, T.; Fisher, A.; Lee, J. Y., *J. Mater. Chem. C* **2018,** *6*, 4007-4014.

216. Wen, C. Z.; Jiang, H. B.; Qiao, S. Z.; Yang, H. G.; Lu, G. Q., *J. Mater. Chem* **2011,** *21*, 7052–7061.

217. Sahoo, P. K.; Kalyan Kamal, S. S.; Premkumar, M.; Jagadeesh Kumar, T.; Sreedhar, B.; Singh, A. K.; Srivastava, S. K.; Chandra Sekhar, K., *Int. J. Refract. Met. Hard Mater.* **2009,** *27*, 784-791.